Silicon Photonic Components using
Sub-wavelength Gratings and other Periodic Structures

by

Han Yun

B. A. Sc., University of British Columbia, 2009

M. A. Sc., University of British Columbia, 2013

A THESIS SUBMITTED IN PARTIAL FULFILLMENT
OF THE REQUIREMENTS FOR THE DEGREE OF

Doctor of Philosophy

in

THE FACULTY OF GRADUATE AND POSTDOCTORAL
STUDIES
(Electrical and Computer Engineering)

The University of British Columbia
(Vancouver)

March 2020

The following individuals certify that they have read, and recommend to the Faculty of Graduate and Postdoctoral Studies for acceptance, the thesis entitled:

Silicon Photonic Components using Sub-wavelength Gratings and other Periodic Structures

submitted by **Han Yun** in partial fulfillment of the requirements for the degree of **Doctor of Philosophy** in **Electrical and Computer Engineering**.

Examining Committee:

Nicolas A. F. Jaeger, Electrical and Computer Engineering, The University of British Columbia
Supervisor

Lukas Chrostowski, Electrical and Computer Engineering, The University of British Columbia
Supervisory Committee Member

Shuo Tang, Electrical and Computer Engineering, The University of British Columbia
University Examiner

Guangrui Xia, Materials Engineering, The University of British Columbia
University Examiner

Additional Supervisory Committee Members:

Sudip Shekhar, Electrical and Computer Engineering, The University of British Columbia
Supervisory Committee Member

Abstract

Sub-wavelength gratings (SWGs) and periodic waveguides play important roles in integrated optics. These periodic structures have been employed in integrated optical power couplers and wavelength filters which are key components for optical communication and sensing systems. This dissertation is a theoretical and experimental study of high performance silicon photonic SWG-based adiabatic couplers, SWG contra-directional couplers (SWG CDCs), and polarization-rotating Bragg grating (PRBG) filters that use these periodic structures.

Mode-evolution-based couplers, also known as adiabatic couplers, are fundamental building blocks for optical communications applications such as broadband optical switches and electro-optic modulators. In this thesis, to begin with, adiabatic 3 dB couplers using conventional silicon-on-insulator (SOI) ridge and strip waveguides are studied and demonstrated for 100-μm-long mode-evolution regions and 100 nm operating bandwidths with splitting imbalances <0.5 dB. Next, SWG waveguides are explored and employed to design and demonstrate a compact, broadband SWG 3 dB adiabatic coupler with a 20-μm-long mode-evolution region, a 130 nm bandwidth, and a splitting imbalance <0.4 dB. Finally, SWG-assisted strip waveguides are studied and utilized for a compact, ultra-broadband, adiabatic 3 dB coupler that has a 15-μm-long mode-evolution region, a 185 nm bandwidth, a splitting imbalance <0.3 dB, low insertion losses (ILs) <0.11 dB, and high fabrication tolerances. The SWG-assisted adiabatic 3 dB couplers have smaller footprints with much wider operating bandwidths and much lower ILs than their alternatives, i.e., directional couplers and multi-mode interference couplers.

SWG CDCs are proposed and demonstrated to provide broadband wavelength filtering for applications such as add-drop filters and bandwidth-tunable filters.

These devices provide square-shaped, drop-port responses with 3 dB bandwidths $>$30 nm and sidelobe suppression ratios $>$50 dB.

PRBGs are proposed and demonstrated using periodic corner corrugations on single-mode SOI strip waveguides for polarization-insensitive wavelength filtering. A PRBG band-rejection filter is demonstrated with a 3 dB bandwidth of 2.63 nm, an extinction ratio (ER) $>$27 dB, and a low IL $<$1 dB for both the transverse electric and transverse magnetic modes. A PRBG band-pass filter is also demonstrated using phase-shifted PRBGs and achieves a 3 dB bandwidth of 0.26 nm and an ER of 19 dB for both modes.

Lay Summary

Optical power couplers and wavelength filters are fundamental building blocks in optical communication systems such as those used for high-speed internet, telephone and cable television distribution, and other data streaming applications. This thesis describes the development of high performance couplers and filters using a low-cost, silicon-based technology, the silicon-on-insulator platform, for next-generation optical communication systems.

This research resulted in novel components for high performance photonic integrated circuits, including compact, ultra-broadband couplers, broadband filters, and polarization-insensitive filters. In addition to communications, these devices can be used in other systems such as sensor systems.

Preface

Parts of the dissertation are based on the author's manuscripts, which have been published, resulting from collaborations with multiple researchers. A complete list of the author's 57 publications is given in Appendix A.

A version of Section 2.2 has been published:

1. Han Yun, Wei Shi, Yun Wang, Lukas Chrostowski, and Nicolas A. F. Jaeger, "2×2 Adiabatic 3-dB coupler on silicon-on-insulator rib waveguides," *Proceedings of SPIE*, 8915, 89150V-1–89150V-6 (2013).

   I conceived the idea with W. Shi. I designed the devices, measured the devices, performed data analysis, and wrote the manuscript. Y. Wang designed the fiber grating coupler and helped with the measurement. Prof. Chrostowski obtained access to the fabrication technology used in this project and provided feedback to the manuscript. Prof. Jaeger provided the supervision and guidance regarding the structure and content of the manuscript.

A version of Section 2.3 has been published:

2. Han Yun, Zeqin Lu, Yun Wang, Wei Shi, Lukas Chrostowski, and Nicolas A. F. Jaeger, "2×2 Broadband adiabatic 3-dB couplers on SOI strip waveguides for TE and TM modes," in *CLEO (Conference on Lasers and Electro-Optics): 2015, (Optical Society of America, 2015)*, p. STh1F.8. (05/2015).

   I conceived the idea, conducted the device design, measured the devices, performed data analysis, and wrote the manuscript. Z. Lu helped with discussions on the design. Y. Wang designed the fiber grating coupler. W. Shi provided feedback to the manuscript. Prof. Chrostowski obtained access to the fabrication technology used in this project and provided feedback to the manuscript. Prof. Jaeger provided the supervision and guidance regarding the structure and content of the manuscript.

A version of Chapter 3 has been published:

3. Han Yun, Yun Wang, Fan Zhang, Zeqin Lu, Stephen Lin, Lukas Chrostowski, and Nicolas A. F. Jaeger, "Broadband 2×2 adiabatic 3 dB coupler using silicon-on-insulator sub-wavelength grating waveguides," *Optics Letters*, vol. 41, pp. 3041-3044, 2016.

   I conceived the idea, conducted the device design, measured the devices, performed data analysis, and wrote the manuscript. Y. Wang designed the fiber grating coupler and helped with the design layout. F. Zhang and Z. Lu helped with discussions on the design. S. Lin helped with the measurement. Prof. Chrostowski obtained access to the fabrication technology used in this project and provided feedback to the manuscript. Prof. Jaeger provided the supervision and guidance regarding the structure and content of the manuscript.

A version of Chapter 4 has been published:

4. Han Yun, Lukas Chrostowski, and Nicolas A. F. Jaeger, "Ultra-broadband 2×2 adiabatic 3 dB coupler using subwavelenght-grating-assisted silicon-on-insulator strip waveguides," *Optics Letters*, vol. 43, pp. 1935-1938, 2018.

   I conceived the idea, conducted the devices' design, measured the devices, performed data analysis, and wrote the manuscript. Prof. Chrostowski obtained access to the fabrication technology used in this project and provided feedback to the manuscript. Prof. Jaeger provided the supervision and guidance regarding the structure and content of the manuscript.

A version of Chapter 5 has been published:

5. Han Yun, Mustafa Hammood, Stephen Lin, Lukas Chrostowski, and Nicolas A. F. Jaeger, "Broadband Flat-top SOI Add-drop Filters using Apodized

Sub-wavelength Grating Contra-directional Couplers," *Optics Letters*, vol. 44, pp. 4929-4932, 2019.

I conceived the idea, conducted the device design, measured the devices, performed data analysis, and wrote the manuscript. M. Hammood helped with discussions on the simulation, the design layout, and the measurement. S. Lin helped with the simulation and the measurement. Prof. Chrostowski obtained access to the fabrication technology used in this project, helped with discussions on the design, and provided feedback to the manuscript. Prof. Jaeger provided the supervision and guidance regarding the structure and content of the manuscript.

A version of Section 6.1 has been published:

6. Han Yun, Zhitian Chen, Yun Wang, Jonas Flueckiger, Michael Caverley, Lukas Chrostowski, and Nicolas A. F. Jaeger, "Polarization-rotating, Bragg-grating filters on silicon-on-insulator strip waveguides using asymmetric periodic corner corrugations," *Optics Letters*, vol. 40, pp. 5578-5581, 2015.

   Prof. Jaeger suggested the project. I conceived the idea, conducted the device design, measured the devices, performed data analysis, and wrote the manuscript. Z. Chen helped with discussions on the design. Y. Wang designed the fiber grating coupler. J. Flueckiger helped with the design layout. M. Caverley provided feedback to this manuscript. Prof. Chrostowski obtained access to the fabrication technology used in this project and provided feedback to the manuscript. Prof. Jaeger provided the supervision and guidance regarding the structure and content of the manuscript.

A version of Section 6.2 has been published:

7. Han Yun, Lukas Chrostowski, and Nicolas A. F. Jaeger, "Narrow-band, polarization-independent, transmission filter in a silicon-on-insulator strip waveguide," *Optics Letters*, vol. 44, pp. 847-850, 2019.

   I conceived the idea, conducted the device design, measured the devices, performed data analysis, and wrote the manuscript. Prof. Chrostowski provided feedback to the manuscript. Prof. Jaeger obtained access to the fabrication technology used in this project and provided the supervision and guidance regarding the structure and content of the manuscript.

Table of Contents

List of Tables

List of Figures

List of Abbreviations

AWG	arrayed waveguide grating
BOX	buried oxide
CMOS	complementary metal-oxide-semiconductor
CDC	contra-directional coupler
CW	continuous-wave
CWDM	coarse wavelength division multiplexing
DC	directional coupler
DUV	deep ultra-violet
EBL	electron beam lithography
ER	extinction ratio
FDTD	finite-difference time-domain
FSR	free-spectral-range
GC	grating coupler
IL	insertion loss
IO	input/output
MMI	multi-mode interference

MPW	multi-project wafer
MRR	micro-ring resonator
MZI	Mach-Zehnder interferometer
OADM	optical add-drop multiplexer
PAM	pulse-amplitude modulation
PIC	photonic integrated circuit
PRBG	polarization-rotating Bragg grating
PSR	polarization splitter-rotator
SEM	scanning electron microscope
SLSR	sidelobe supression ratio
SOI	silicon-on-insulator
SWG	sub-wavelength grating
TE	transverse electric
TM	transverse magnetic
WDM	wavelength-division multiplexing

Acknowledgments

I would like to thank my parents for their unconditional love, continuous support, encouragement, and faith throughout my undergraduate and graduate studies. I would like to thank my wife and my daughter for their ever-lasting love and faith on me.

I would like to express my gratitude to my supervisor, Prof. Nicolas A. F. Jaeger, for the inspiration, great support, guidance, and mentorship that he has provided throughout my research at the University of British Columbia (UBC), which has been a wonderful journey in my life. I would like to thank Prof. Lukas Chrostowski for the dedicated help, insightful suggestions, and fruitful discussions that he has provided throughout my PhD journey. I would also like to thank Prof. John D. Madden for his participation in my Department Exam and for his insightful suggestions and fruitful discussions. In addition, I would like to thank Prof. Hon Ki Tsang from the Chinese University of Hong Kong for reviewing my thesis as the External Examiner of my University Exam and for his thoughtful comments and constructive suggestions. I would also like to thank Prof. Mu Chiao at the Department of Mechanical Engineering of UBC for his participation as the Chair of my University Exam.

I would also like to thank all of my current and former colleagues, with whom I have been working, for their help and support, in particular Prof. Wei Shi, Dr. Xu Wang, Dr. Jonas Flueckiger, Dr. Miguel Ángel Guillén-Torres, Dr. Robert Boeck, Dr. Yun Wang, and Dr. Zeqin Lu, as well as Charlie Lin, Zhitian Chen, Fan Zhang, Michael Caverley, Anthony Park, Minglei Ma, Enxiao Luan, Hossam Shoman, Rui Cheng, Mustafa Hammood, Ajay Mistry, Stephen Lin, Jaspreet Jhojia, and Donald Witt. Also, I would like to thank Richard J. Bojko and N. Shane Patrick at the University of Washington and Cameron Horvath at the Applied Nanotools, Inc. for fabricating many of the devices that are presented within this dissertation as well as Dr. Yiheng Lin at the Department of Material Engineering of UBC for taking optical microscope images. In addition, I would like to acknowledge Dr. Dan Deptuck and Dr. Jessica Zhang from CMC Microsystems for their help.

Also, I acknowledge the Natural Sciences and Engineering Research Council of Canada (NSERC), the NSERC CREATE SiEPIC program, CMC Microsystems, and Keysight Technologies, Inc. for their financial support, and Lumerical, Inc., and Mentor Graphics for the design software. Part of this work was conducted at the University of Washington Nanofabrication Facility (a member of the NSF National Nanotechnology Infrastructure Network) and at Applied Nanotools, Inc.

Dedication

To my father, Qinglong Yun, and my mother, Gexin Jin, whose unconditional love, continuous support, encouragement, and faith have given me the strength to overcome obstacles and to succeed in so many aspects and areas of my life.

To my beloved wife, Xiaoran Ma, who loves, inspires, supports, and encourages me at every step of this journey.

To my daughter, Grace Fangfei Yun, who has served as my inspiration.

Chapter 1

Introduction

1.1 Silicon Photonics

Silicon photonics, using a high-index-contrast silicon-on-insulator (SOI) platform, is an emerging technology that can be used to integrate large-scale photonic and electronic circuits to obtain eletronic-photonic functionality. The low cost of high crystal quality silicon wafers, and their compatibility with mature silicon integrated circuit manufacturing techniques, have enabled the rapid growth of silicon photonics in recent years. Due to the strong optical confinement, which is offered by the high refractive index contrast between silicon and silicon dioxide, on the SOI platform, the feature sizes of silicon photonic integrated circuits (PICs) have been scaled down to the sub-micron level. Fabricated using processes developed for advanced complementary metal-oxide-semiconductor (CMOS) technology nodes, e.g., the 90-nm node, high levels of integration of highly compact PICs can be realized with low manufacturing costs [1–3].

During the past two decades, various photonics components with compact footprints and competitive performances have been proposed and demonstrated on the SOI platform within standard telecommunications optical wavelength bands, i.e., from 1260 nm to 1675 nm. These components include low-loss waveguides [4, 5], optical inputs/outputs (IOs) [6–12], power couplers/splitters [13–16], wavelength filters [17–22], multi/demultiplexers [23–26], electro-optic modulators [27–34], photodetectors [35, 36], etc. Using mature hybrid integration and packaging techniques, integrated systems using many of these components have been publicly announced and/or commercially released to the telecommunications and data communications markets. Those products that have been released are typically produced in large volumes by world leading semiconductor and telecommunications companies. Acacia Communications Inc. [37], Luxtera (now part of Cisco) [38], Finisar (now part of II-IV Inc.) [39], and Intel [40] are examples of such companies. Silicon photonics-based optical coherent transceiver modules, for example, have been released with a wide range of data rates up to 200 Gbps [38, 40, 41] for optical interconnects in data centers and high-performance computing. In these modules, power couplers/splitters, polarization beam splitter and rotators, wavelength (de)multiplexers, modulators, photodetectors, and lasers are integrated to achieve high performance PICs in a compact size with reduced costs [3, 42].

Recently, within the past five years, there have been significant technological breakthroughs towards the monolithic integration of photonic and electronic devices on SOI platforms [43]. In 2015, a microprocessor integrating over 850 photonic components and 70 million transistors on a single chip [44] was demonstrated using a commercial 45-nm CMOS fabrication process [45]. In 2016, continuous-wave (CW) InAs/GaAs quantum dot lasers, which were directly grown on silicon substrates, were demonstrated [46]. Also in 2016, a 56 Gb/s silicon photonic pulse-amplitude modulation (PAM) transmitter [47] was demonstrated by monolithically integrating silicon travelling-wave modulators and CMOS driver circuits on a single chip using the IBM's 90-nm CMOS fabrication process [2]. In 2018, 10 Gbps wavelength-division multiplexing (WDM) transceiver chips were demonstrated by integrating silicon photonic components, digital electronic circuits, and thermal tuner controllers on a chip using a 65-nm bulk CMOS fabrication technology [48]. Recently MACOM demonstrated a 4$\times$106 Gbps PAM-4 silicon photonics transmitter, with monolithic integrated CW InP lasers, on a single chip [49]. Advances in silicon photonics, and its compatibility with standard CMOS processes, allow high speed, high density data transmission with low power consumption at low cost, which provide promising solutions for next-generation optical communications applications.

1.1.1 The Silicon-on-Insulator Platform

Figure. 1.1 shows a schematic of a cross-section of an SOI wafer that is commonly used for silicon photonics fabrication. An SOI wafer typically consists of a silicon substrate (~700 μm thick), a buried oxide (BOX) layer (2 to 3 μm thick), and a thin, crystalline, silicon layer [50]. Optical waveguides and devices are defined in the thin, crystalline, silicon layer and are usually covered by another oxide (cladding) layer for protection. The thickness of the thin silicon layer is typically 220 nm, which has become a standard offering by silicon photonics foundries [51]. It should be noted that some commercially available products, such as silicon active optical cables from Luxtera [38], are based on a thicker silicon layer (300 nm for example), but this is not widely available to the research community or to small companies [3]. The devices presented in this dissertation are based on SOI wafers with a 220 nm silicon layer. The thickness of the silicon layer that we used is the same as that provided by silicon photonics multi-project wafer (MPW) foundries, such as imec, CEA-LETI, A*Star/IME/AMF, and IHP [52–55].

In this thesis, the devices defined in the 220 nm silicon layer were patterned using either 193 nm deep ultra-violet (DUV) lithography (provided by imec and IME/AMF) or electron beam lithography (EBL), provided by the Washington Nanofabrication Facility [56] and the Applied Nanotools, Inc. [57]. These two approaches are common choices for silicon photonics fabrication on SOI platforms. The DUV lithography process has high throughput for mass production whereas the EBL pro-

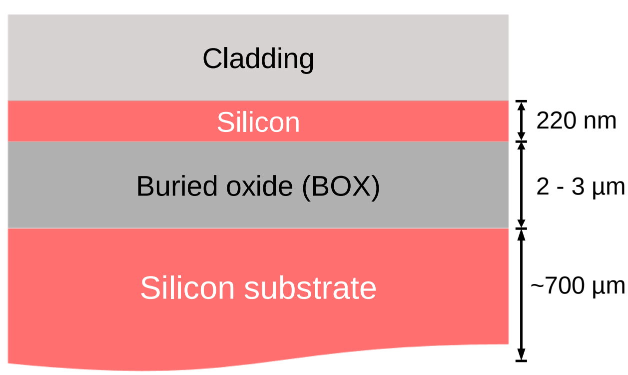

Figure 1.1: Schematic of the cross-section of a typical silicon-on-insulator (SOI) wafer.

cess is suitable for rapid-prototyping research and development purposes but at the cost of low throughput [58]. Detailed fabrication procedures of using these two approaches can be found in Refs. [59–61].

1.1.2 Challenges and State of the Art

In silicon PICs, passive photonic devices are fundamental building blocks for subsystems or system integration. Although significant progress has been achieved, many challenges remain to be solved to improve the performance at the component-level and, therefore, to achieve satisfactory system performance. The high refractive index contrast between the silicon layer and the cladding layer allows SOI waveguides with small cross-sectional geometries (typically 500-nm-wide by 220-nm-high) to have guided optical modes with strong optical confinement for single-mode operation. However, this high index contrast also raises the problems of dispersion and birefringence, which limit the device performance such as operating bandwidth and polarization independence.

Power Coupler/Splitter

Optical power couplers/splitters are key components for combining and splitting light between waveguides with desired coupling ratios and are widely used for interferometer-based optical switches and electro-optic modulators. Optical power couplers/splitters, having broad operating bandwidths, low splitting imbalances, low insertion losses (ILs), small footprints, and high fabrication tolerances, have always been needed for high performance optical switches [62–64] and modulators [31, 65]. Figure 1.2 shows the schematic diagrams of four types of optical power coupler/splitter that are commonly used on SOI platforms. They are Y-junctions, directional couplers (DCs), multi-mode interference (MMI) couplers, and adiabatic couplers. Y-junctions have the most compact footprints with low ILs but are 1×2 couplers which are not suitable for applications such as $N \times N$ switch matrices. DCs, consisting of two parallel symmetric waveguides, have simple structures but are highly sensitive to wavelength changes and fabrication variations. MMI couplers are self-image based devices with broader operating bandwidths than DCs and low splitting imbalances; however, they have higher ILs

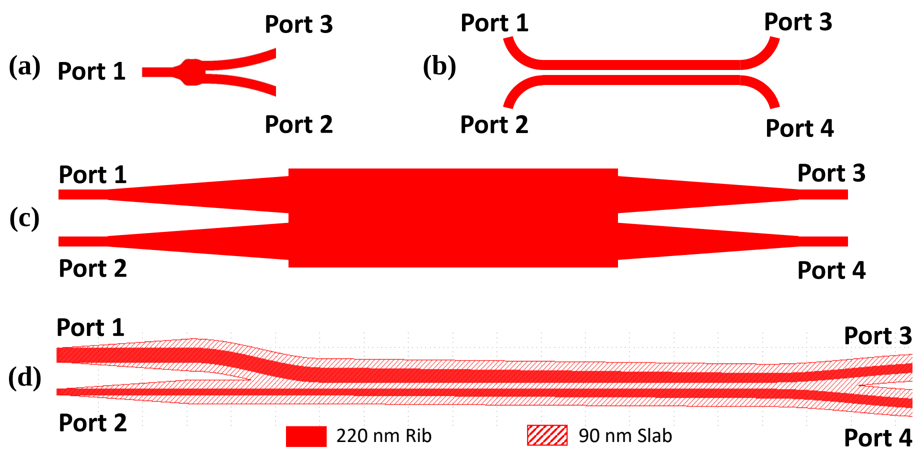

Figure 1.2: Schematics of optical power couplers/splitters that are commonly used in silicon photonic integrated circuits: (a) Y-junction, (b) directional coupler, (c) MMI coupler, and (d) adiabatic coupler.

than other types of coupler/splitter and are sensitive to fabrication variations [66]. Adiabatic couplers are mode-evolution based couplers that support broadband operation [67]. In an adiabatic coupler, two parallel, tapered waveguides are used to evolve either the fundamental mode or the next higher-order mode of two asymmetric waveguides at one end of the coupler to the same order mode of two symmetric waveguides at the other end of the coupler, respectively, and vice versa. Due to its operating principle, the adiabatic coupler has broad operating bandwidth, low IL, low splitting imbalance, and high tolerance to fabrication imperfections. However, due to the strong mode confinements in regular SOI waveguides (either strip or ridge waveguides), adiabatic couplers need long mode-evolution (or coupling) regions and, therefore, often have large footprints. It is a great challenge to reduce the footprints of adiabatic couplers while maintaining their advantages of broad operating bandwidths, low ILs, low splitting imbalances, and high tolerance to fabrication imperfections. Several methods have been proposed to reduce the footprints of adiabatic couplers, such as simultaneously tapering the gap distance between the two waveguides [68], using a narrow waveguide gap distance of 100 nm [69], or using non-linear waveguide tapering profiles [70–72], but at a cost of increased IL, increased splitting imbalance, and increased design and fabrication complexity.

Ref.	Year	Polarization	BW (nm)	Splitting Ratio (dB)	IL (dB)	L_E (μm)	Waveguide
[73]	2006	TE&TM	300	3±0.7	∼0.5	250	Rib
[74]	2010	TE	90	3±1.1	NA	200	Rib
[68]	2013	TE	100	3±0.2	0.31	300	Rib
[15]	***2013***	***TE***	***100***	***3±0.5***	***<1***	***100***	***Rib***
[62]	2013	TE	70	3±0.3	<1	100	Strip
[75]	***2015***	***TE/TM***	***100***	***3±0.8 (TE)*** ***3±0.2 (TM)***	***<0.5***	***100 (TE)*** ***122 (TM)***	***Strip***
[76]	***2016***	***TE***	***130***	***3±0.4***	***<0.5***	***20***	***SWG***
[77]	2017	TE&TM	100	3±0.7	NA	125	Strip
[78]	***2018***	***TE***	***185**** ***500*****	***3±0.3***	***<0.11***	***15***	***SWG-assisted Strip***
[69]	2018	TE&TM	100 (TE) 80 (TM)	3±0.6 (TE) 3±0.1 (TM)	∼1	75	Strip
[79]	2018	TE&TM	100	3±0.27	<0.74	25	SWG-assisted Slot
[71]	2018	TE	100	3±0.3	<0.3	60	Rib
[72]	2019	TE	100	3±0.5	<0.3	26.3	Rib

*: Measured bandwidth (limited by our test setup).
**: Simulated bandwidth.

Table 1.1: Comparison of mode-evolution-based, 2×2 power splitters on SOI platforms. The adiabatic couplers developed in this dissertation are highlighted in ***bold italics***. BW: Bandwidth; L_E: mode evolution region length.

Table. 1.1 lists the adiabatic 3 dB couplers developed in this dissertation as well as state-of-the-art, mode-evolution-based, SOI power splitters demonstrated by other research groups in chronological order. In this dissertation, broadband adiabatic 3 dB couplers using regular SOI rib [15] (2013) and strip waveguides [75] (2015) are demonstrated in Chapter 2 both with 100 nm operating bandwidths and 100-μm-long mode-evolution regions (a reduction in length by a factor of 2 at the time that my first work in this area was published [15]) for the TE mode. Compact, broadband adiabatic 3 dB couplers using sub-wavelength grating (SWG) waveguides [76] (2016) are demonstrated in Chapter 3 with 130 nm operating bandwidths and 20-μm-long mode-evolution regions, which were at least 80 percent shorter and had at least 30 percent wider bandwidths than any prior reports on adiabatic couplers. Compact, ultra-broadband adiabatic 3 dB couplers using SWG-assisted waveguides [78] (2018) are demonstrated in Chapter 4 with 500 nm (simulated) and 185 nm (measured) operating bandwidths[†], 15-μm-long mode-evolution regions, ILs <0.11 dB, and splitting imbalances $< \pm 0.3$ dB, which represented state-of-art performance at that time. As shown in Table. 1.1, our approach of using SWG-based waveguides substantially reduces the footprint of adiabatic couplers and extends their operating bandwidths while maintaining low insertion losses, low splitting imbalances, and high tolerances to fabrication errors. More important, our SWG-assisted adiabatic coupler improves the state-of-the-art performance in terms of feature size, operating bandwidth, insertion loss, and splitting imbalance. Until now, there has been no improvements with regards to bandwidth or length on our results for our SWG-assisted adiabatic couplers [78] published in 2018 [69, 71, 72, 79]. In comparison with other types of SWG-based power splitters [80, 81], our SWG-assisted adiabatic couplers have much lower insertion losses and splitting imbalances, and are more robust to fabrication imperfections.

Wavelength Filter

Optical wavelength filters are essential devices for wavelength-selective filtering and have been widely used for applications including optical add-drop multiplexers (OADMs), modulators, bio-sensors, etc. SOI wavelength filters with flat-top, square-shaped responses and broad operating bandwidths are promising candidates for applications such as bandwidth-tunable filtering, dispersion engineering, and WDM band splitting. Among the various types of SOI filter, contra-directional couplers (CDCs) are competitive due to their compact sizes, flat-top responses, low ILs, and high extinction ratios (ERs). As shown in Fig. 1.3, a CDC usually consists of two asymmetric waveguides with integrated, first-order, Bragg gratings on each waveguide. Typically, for either transverse electric (TE) or transverse magnetic (TM) modes, the Bragg gratings couple light contra-directionally between the fundamental mode and the next higher-order mode of the two asymmetric waveguide system at selected wavelengths. Therefore, when light is injected into one

[†]The measured bandwidth was limited by our test setup.

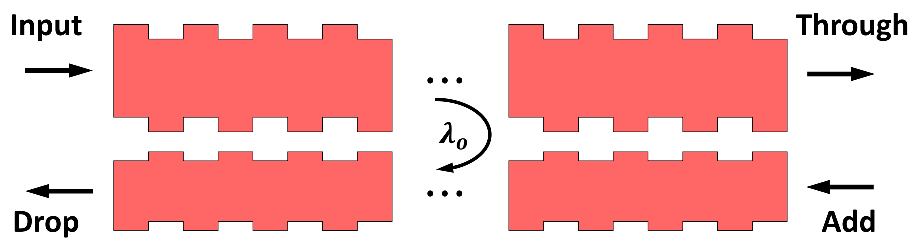

Figure 1.3: Schematic of a CDC with uniform gratings.

waveguide, the selected wavelengths will be dropped and reflected to the other waveguide of the CDC. Unlike micro-ring resonators (MRRs), first-order, Bragg grating based CDCs have unlimited free-spectral-ranges (FSRs). As compared with other waveguide Bragg grating filters [20, 82], CDCs do not need additional circulators or power couplers/splitters (which have their own, additional, ILs) to separate the dropped signal from the input signal with extra ILs. However, due to the strong mode confinement in conventional SOI waveguides (either strip or ridge waveguides), it is difficult to achieve a very large coupling strength between the two system modes and, thus, SOI CDCs typically have bandwidths of less than 10 nm. Recently CDCs utilizing one conventional strip waveguide and one SWG waveguide have been proposed and demonstrated on SOI platforms [83–85]. However, these devices have low ERs and/or strong sidelobes.

In this dissertation, in Chapter 5, broadband CDCs using two apodized SWG waveguides are demonstrated with broad 3 dB bandwidths of 32.6 nm, high sidelobe supression ratios (SLSRs) $>$19 dB and high ERs $>$40 dB. Moreover, our series-cascaded SWG contra-DCs provide square-shaped filtering responses with 3 dB bandwidths $>$30 nm and SLSRs $>$50 dB. These devices provide the state-of-the-art performance in terms of bandwidth and SLSR and are competitive candidates for applications such as WDM band-splitters and bandwidth-tunable filters.

Polarization Diversity

Polarization diversity is another challenge in silicon PICs. Due to the cross-sectional geometry of SOI waveguides (typically 500 nm wide by 220 nm high) and the high refractive index contrast between the silicon layer and the cladding layer, SOI devices suffer from modal birefringence and are highly polarization-sensitive. This makes them incompatible with fiber-optic systems that use non-polarization-maintaining, single-mode fibers, since light is typically coupled from optical fibers to silicon PICs in arbitrary polarization states [86]. SOI wavelength filters, such as MRRs, arrayed waveguide gratings (AWGs), waveguide Bragg gratings, and CDCs, are typically designed for either TE mode or TM mode operation. To work for both polarization types, several methods have been proposed such as using cladding stress on SOI ridge waveguides [87] or implementing polarization control circuits at the inputs of the filters [88–90]. However, these methods increase the design complexity as well as the fabrication costs. Using polarization-rotating Bragg gratings (PRBGs) [91–93] provides an alternative solution to meet the needs for polarization-independent wavelength filtering. As shown in Fig. 1.4, a single PRBG-based filter will pass, or reflect, both the TE and TM modes at the same wavelength without the need to use additional polarization beam splitters and/or polarization rotators such as required in most polarization diversity circuits [88, 89]. Recently PRBG-based filters [94] using non-vertical waveguide sidewalls have been proposed and demonstrated on the SOI platform. However, these devices were demonstrated using 300-nm-thick waveguides and required special control of the sidewall angles during the fabrication process. In contrast, over the past decade, silicon photonic foundries have been putting a lot of effort into fabricating SOI waveguides with nearly vertical sidewalls for silicon PICs.

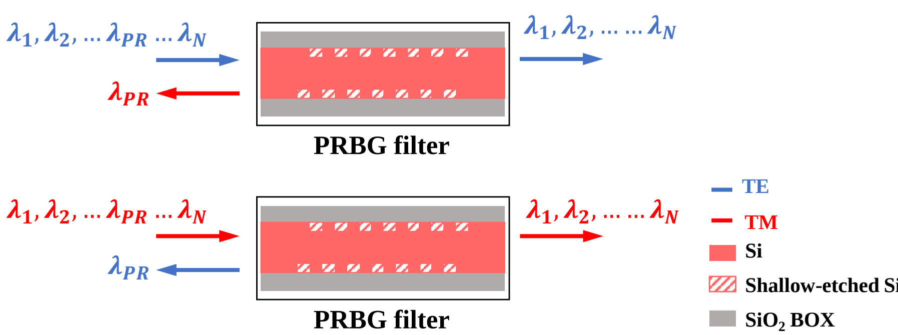

Figure 1.4: Illustration of polarization-independent wavelength filtering and wavelength-selective polarization-rotating achieved by using an SOI, PRBG-based, band-rejection filter.

In Chapter 6 of this dissertation, compact, PRBG-based, band-rejection and transmission filters, which work with vertical sidewalls, are demonstrated on regular, 220-nm-thick, SOI strip waveguides. Unlike the device demonstrated in [94], my approach uses partially-etched, waveguide corner corrugations and is achieved by using a standard duo-etching process, that is widely offered by silicon photonics foundries. In comparison with the previous work [94], my PRBG band-rejection filter is more compact, having a total grating length of 294.4 μmm (as compared to 1 mm [94]) and achieves higher ERs $>$27 dB for both the TE mode and the TM mode [95]. Based on our approach of using waveguide corner corrugations, the work in [96] introduced a quarter-wave phase-shift to the PRBG waveguide in order to obtain a PRBG transmission filter that had unbalanced transmission peaks with 0.2 nm bandwidths and 5 dB insertion losses for both the TE mode and the TM mode. In this dissertation, in Section 6.2, I present a thermally-tunable PRBG transmission filter that achieves balanced transmission peaks with 0.26 nm bandwidths, insertion losses $<$0.5 dB, and wavelength tuning efficiencies of 0.028 nm/mW for both the TE mode and the TM mode [97]. Our PRBG filters set the state-of-the-art performance in terms of feature size, operating bandwidth, and insertion loss for polarization-independent wavelength filtering.

1.2 Silicon Photonic Periodic Waveguide Structures

The propagation and diffraction of light in periodic waveguide structures show numerous phenomena that are widely used in integrated optics. Periodic waveguide structures are obtained by periodically modulating the effective refractive index along the propagation direction of the optical mode in the waveguide system. It should be noted that the waveguide system refers to a system consisting of either one or multiple physical waveguides and, therefore, the optical modes refer to the eigenmodes of the entire system (instead of a single waveguide). The periodic modulation can be achieved by either varying the refractive index (e.g., alternating material) or changing the physical dimensions of the waveguides. In silicon photonics, while there are a few approaches such as ion implantation [98, 99] and external cladding modulation [100, 101], the periodic grating patterns are usually formed by changing the physical dimensions of the waveguide using physical cor-

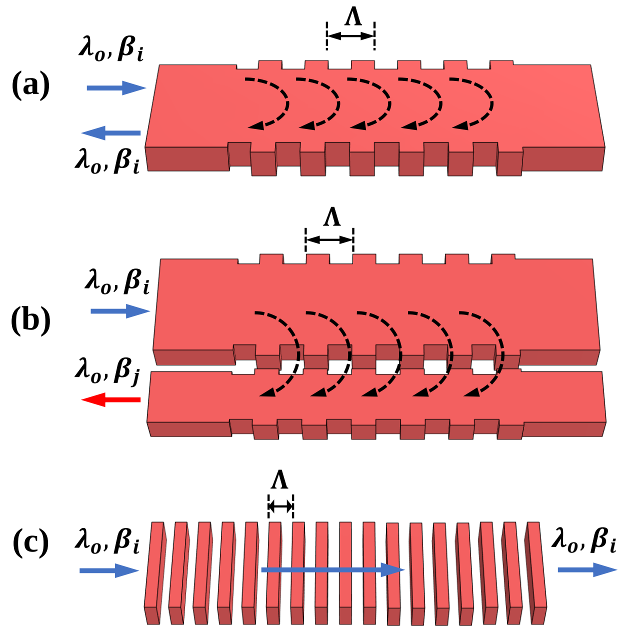

Figure 1.5: Schematic drawings of several periodic waveguide structures and the diffraction (or propagation) of light: (a) a waveguide Bragg grating reflector, (b) a grating-based, contra-directional coupler, and (c) a sub-wavelength grating waveguide.

rugations [18–20, 22, 82, 102–106] that lead to the modulation of the effective refractive index of the optical modes in the waveguides.

The effective refractive index modulation perturbs the propagating optical mode with the periodicity (i.e., the grating period), Λ. Therefore, as illustrated in Fig. 1.5, light can be scattered (or propagated) at the operating wavelength, λ_o, in one of the following cases: (a) reflected back, (b) coupled from the current guided mode into another guided mode, and (c) continue propagating with diffraction effects fully suppressed. Waveguide Bragg grating reflectors [20, 82, 107], contra-directional couplers (CDCs) [19, 22, 103], and sub-wavelength gratings (SWGs) [108, 109] are typical examples of cases (a), (b), and (c), respectively.

1.2.1 Coupled-Mode Analysis

The operation of periodic grating structures can be understood by using coupled mode theory [110, 111]. The corrugations have the effect of periodically varying the dielectric constant profile of the waveguide system along the length of the grating and can cause the i-th mode of the waveguide system, having a propagation constant β_i, to be coupled into the j-th mode, having a propagation constant β_j. This coupling only occurs when the phase-match condition is met, which is given by

$$\beta_i - \beta_j = m \cdot \frac{2\pi}{\Lambda}, \tag{1.1}$$

for some integer m. In this dissertation, only the case in which $m = \pm 1$ is considered since first-order gratings are used in all of my devices. It should be noted that $\beta_i \cdot \beta_j$ can be either positive or negative. When $\beta_i \cdot \beta_j > 0$, the coupled j-th mode has a component in the same propagation/diffraction direction as the input i-th mode, whereas, when $\beta_i \cdot \beta_j < 0$, the coupled j-th mode has a component in the opposite propagation direction to the input i-th mode [see Figs. 1.5(a) and (b)]. As shown in Fig. 1.5(a), periodic gratings act as Bragg reflectors and couple light from forward propagating modes into the same order, backward propagating modes, when $\beta_j = -\beta_i$. As shown in Fig. 1.5(b), when $i \neq j$ and $\beta_i \beta_j < 0$, the gratings contra-directionally couple light from the forward propagating, i-th mode into the backward propagating, j-th mode of the two waveguide system. However, when

$$\Lambda < \frac{\lambda_o}{2 \cdot max\{n_{eff,i},\ n_{eff,j}\}}, \tag{1.2}$$

where $n_{eff,i}$ and $n_{eff,j}$ are the wavelength-dependent effective indices of the i-th and j-th eigenmodes, respectively, no phase-match condition will be met and there will be no diffraction. In such a case, as shown in Fig. 1.5(c), the gratings are referred to as SWGs waveguides and light will propagate through the SWG waveguides without being affected by the discontinuities along the direction of propagation [108, 109].

The spectral responses of the coupling between the two modes in periodic grating structures can be determined using coupled-mode theory. When light propagates along the z direction of the waveguide system, the electric field can be written as [111]:

$$E(x,y,z) = A(z)E_a(x,y)e^{-j\beta_a z} + B(z)E_b(x,y)e^{-j\beta_b z} \tag{1.3}$$

where $E_a(x,y)$ and $E_b(x,y)$ are the normalized transverse electric field distributions of the eigenmodes that have the propagation constants β_a and β_b, respectively, and $A(z)$ and $B(z)$ are the field amplitudes as functions of the longitudinal position, z. In the presence of the gratings, the coupled-mode equations are given by [111]:

$$\begin{aligned} \tfrac{d}{dz}A(z) &= -j\tfrac{\beta_a}{|\beta_a|}\kappa_{ab}B(z)e^{j\Delta\beta z} \\ \tfrac{d}{dz}B(z) &= -j\tfrac{\beta_b}{|\beta_b|}\kappa_{ba}A(z)e^{-j\Delta\beta z} \end{aligned} \tag{1.4}$$

where $\kappa_{ab} = \kappa_{ba}^*$ and κ_{ab} and κ_{ba} are the distributed coupling coefficients of the gratings and represent the coupling strength between the two modes. $\Delta\beta$ is the phase mismatch and is given by $\Delta\beta = \beta_a - \beta_b - \frac{2\pi}{\Lambda}$. The coupling coefficients are given by [21, 111]:

$$\kappa_{ab} = \kappa_{ba}^* = \frac{\omega}{4}\iint \mathbf{E}_a^*(x,y)\cdot\varepsilon(x,y)\mathbf{E}_b(x,y)dxdy \tag{1.5}$$

where ω is the optical angular frequency and ε is the first-order Fourier component of the dielectric perturbation. Eq. 1.5 is appropriate for the case in which the effect of the dielectric perturbation is small. For high index contrast waveguides, with strong perturbations, κ can be calculated using finite-difference time-domain (FDTD) simulation techniques with Bloch boundary conditions [104].

For either reflective or contra-directional coupling between the two modes, the coupled modes are propagating in opposite directions and, therefore, $\beta_a/|\beta_a|$ and $\beta_b/|\beta_b|$ become 1 and -1, respectively. In this case, Eq. 1.4 becomes:

$$\begin{aligned} \tfrac{d}{dz}A(z) &= -j\kappa B(z)e^{j\Delta\beta z} \\ \tfrac{d}{dz}B(z) &= j\kappa^* A(z)e^{-j\Delta\beta z} \end{aligned} \tag{1.6}$$

The general solutions of Eq. 1.6 can be written as:

$$\begin{aligned} A(z) &= \left\{ \left[\cosh(sz) - j\tfrac{\Delta\beta}{2s}\sinh(sz) \right] A(0) - j\tfrac{\kappa}{s}\sinh(sz)B(0) \right\} e^{j\frac{\Delta\beta}{2}z} \\ B(z) &= \left\{ j\tfrac{\kappa^*}{s}\sinh(sz)A(0) + \left[\cosh(sz) + j\tfrac{\Delta\beta}{2s}\sinh(sz) \right] B(0) \right\} e^{-j\frac{\Delta\beta}{2}z} \end{aligned} \tag{1.7}$$

where $s = \sqrt{|\kappa|^2 - (\Delta\beta/2)^2}$ and $A(0)$ and $B(0)$ are the field amplitudes at $z = 0$. The complex amplitudes of the electric fields for the forward and backward propagating modes can be defined by including their propagation phases and are given by

$$\begin{aligned} a(z) &= A(z)e^{-j\beta_a z} \\ b(z) &= B(z)e^{-j\beta_b z} \end{aligned} \tag{1.8}$$

Then Eq. 1.7 can be written in a transfer matrix form as

$$\begin{bmatrix} a(z)e^{j\frac{\beta_a+\beta_b}{2}z}e^{+j\frac{\pi}{\Lambda}z} \\ b(z)e^{j\frac{\beta_a+\beta_b}{2}z}e^{-j\frac{\pi}{\Lambda}z} \end{bmatrix} = \begin{bmatrix} \cosh(sz) - j\frac{\Delta\beta}{2s}\sinh(sz) & -j\frac{\kappa}{s}\sinh(sz) \\ j\frac{\kappa^*}{s}\sinh(sz) & \cosh(sz) + j\frac{\Delta\beta}{2s}\sinh(sz) \end{bmatrix} \begin{bmatrix} a(0) \\ b(0) \end{bmatrix} \tag{1.9}$$

Since the matrix is unimodular, by inverting the above matrix equation, Eq. 1.9 can be rearranged to give

$$\begin{bmatrix} a(0) \\ b(0) \end{bmatrix} = \begin{bmatrix} \cosh(sz) + j\frac{\Delta\beta}{2s}\sinh(sz) & j\frac{\kappa}{s}\sinh(sz) \\ -j\frac{\kappa^*}{s}\sinh(sz) & \cosh(sz) - j\frac{\Delta\beta}{2s}\sinh(sz) \end{bmatrix} \begin{bmatrix} a(z)e^{j\frac{\beta_a+\beta_b}{2}z}e^{+j\frac{\pi}{\Lambda}z} \\ b(z)e^{j\frac{\beta_a+\beta_b}{2}z}e^{-j\frac{\pi}{\Lambda}z} \end{bmatrix} \tag{1.10}$$

In Eq. 1.10, assuming that the total length of the grating is an integer multiple of Λ, the $e^{\pm j\frac{\pi}{\Lambda}z}$ terms will be either +1 or -1 depending on whether the total length of the grating is an even or odd integer multiple of Λ, respectively. For a uniform grating with a total length, $L = N \cdot \Lambda$, the total power coupling efficiency, η, is given by

$$\eta = \left.\frac{|b(0)|^2}{|a(0)|^2}\right|_{b(L)=0} = \frac{|\kappa|^2\sinh^2(sL)}{s^2\cosh^2(sL) + (\Delta\beta/2)^2\sinh^2(sL)} \tag{1.11}$$

At the central wavelength where $\Delta\beta = 0$, the peak power coupling efficiency is

$$\eta_{peak} = \tanh^2(\kappa L) \tag{1.12}$$

The bandwidth between the first two nulls (zeros) around the central wavelength in the coupling spectral response is determined by [111, 112]:

$$\Delta\lambda = \frac{\lambda_o^2}{\pi(n_{g,a} + n_{g,b})/2}\sqrt{\kappa^2 + \left(\frac{\pi}{L}\right)^2} \tag{1.13}$$

where $n_{g,a}$ and $n_{g,b}$ are the group indices for the two modes, respectively. For long gratings, Eq. 1.13 can be simplified to be:

$$\Delta\lambda = \frac{\lambda_o^2 \kappa}{\pi(n_{g,a} + n_{g,b})/2} \tag{1.14}$$

It should be noted, coupled-mode theory assumes that the effect of the dielectric (refractive index) perturbation is small. Therefore, coupled-mode theory was originally used for weakly guiding fiber Bragg gratings and has been used to model weakly coupled Bragg gratings on SOI platforms [18, 104]. Nevertheless, it has also been shown to provide good agreement between simulations and measurements when used to model strongly coupled SOI Bragg gratings [22, 85, 113, 114].

1.2.2 Sub-wavelength Gratings

In SWGs, the SWG period, Λ_{SWG}, is selected to be much smaller than π/β, where β is the propagation constant of the optical mode under consideration. Therefore, instead of resulting in Bragg diffraction, the light propagating in an SWG waveguide can be treated as it would be in a regular waveguide made of homogeneous material with an equivalent refractive index [115]. When light travels through the SWG structure in the z direction (see Fig. 1.6), it propagates in Floquet-Bloch modes along the periodic structure, which is very similar to the motion of electrons in crystalline solids [111]. The derivations and the mathematical proof of the Bloch theorem for waves propagating in periodic dielectric media can be found in Sections 12.1 and 12.2 of Ref. [111].

The equivalent refractive index of SOI SWGs can be calculated using [116, 117]:

$$\begin{aligned} n_{\parallel}^2 &= ff \cdot n_{core}^2 + (1-ff) \cdot n_{clad}^2 \\ \frac{1}{n_{\perp}^2} &= ff \cdot \frac{1}{n_{core}^2} + (1-ff) \cdot \frac{1}{n_{clad}^2} \end{aligned} \tag{1.15}$$

where $n_{\parallel}$ and $n_{\perp}$ are the the equivalent refractive indices for the polarization along the y direction and the z direction (see Fig. 1.6), respectively. n_{core} and n_{cladd} are the refractive indices for the waveguide core and cladding material, which are Si and SiO_2 in this work, respectively, and ff is the grating duty cycle (the ratio of the silicon strip width to the grating period). Eq. 1.15 provides a good starting point for SWG structure design. However, when using Eq. 1.15, the assumption has been made that the SWG structure is infinite in the y and z directions. For a precise design, in this dissertation, a 3D FDTD band structure simulation tool [104], provided by Lumerical, Inc., was used to numerically calculate the properties of the Floquet-Bloch modes propagating along the SWG structure. 3D FDTD band structure calculations simulate the actual structure and take the material dispersion, the structure dispersion, and the Bragg effect into consideration. Instead of simulating the full SWG structure, 3D FDTD band structure calculations simulate only a single grating period of the SWG structure with Bloch boundary conditions applied in the mode propagation direction in FDTD Solutions (from Lumerical, Inc.). In this work, all of the SWG structures are analyzed using this numerical simulation method.

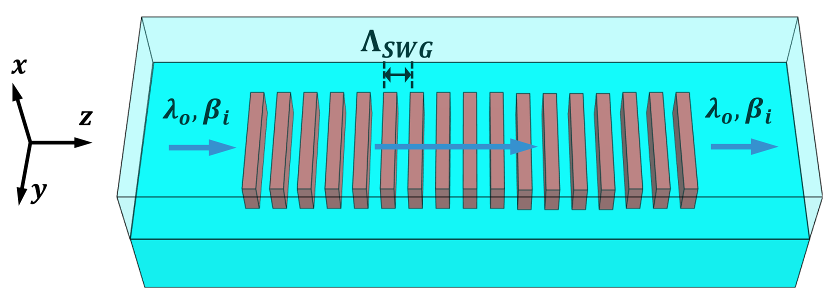

Figure 1.6: Schematic drawing of a sub-wavelength grating waveguide with light propagating along the z direction.

SWG structures provide the flexibility to tailor the effective refractive indices and the dispersion properties of the optical modes, which have been used in PICs on the SOI platform. Many SWG-based components have been proposed or demonstrated, such as grating couplers (GCs) [10, 12, 118], MRRs [119–121], waveguide Bragg grating filters [122, 123], MMI couplers [81, 124], DCs [80, 125], and polarization splitter-rotators (PSRs) [90, 126, 127], for optical communications and sensing applications. In this work, SWG waveguides are used in adiabatic couplers [76, 78] and CDCs [114] for broadband operation.

1.2.3 Polarization-rotating Bragg Gratings

Periodic waveguide structures can be used to achieve coupling and exchange of energy between the polarization modes. Such polarization mode coupling occurs when both of the following conditions are met [111]:

- A periodic perturbation with a period Λ is required to meet the phase-match condition in Eq. 1.1.
- The perturbation breaks the optical symmetry of the modes so that the coupling between the two polarization modes is nonzero.

Polarization-rotating Bragg gratings (PRBGs) provide the required perturbation and can be used to couple light between a TE-polarized mode and a TM-polarized mode at selected wavelengths. These gratings break the optical symmetry of the waveguides in the transverse plane and periodically perturb the light in the waveguide. This results in the light being reflected with its polarization rotated at selected wavelengths. Therefore, PRBGs can be used for applications in which polarization-independent wavelength filtering is desired.

To obtain PRBGs, as shown in Fig. 1.7(a), one approach is to use asymmetric periodically loaded waveguides, which have been previously demonstrated optically in lnP [91] and at microwave frequencies in polycarbonate [93]. In these devices, asymmetric periodic Bragg grating structures were integrated on top of the waveguides. Another approach used has been to integrate Bragg gratings on waveguides that have tilted sidewalls. Such devices have been demonstrated using ridge waveguides in InGaAsP-lnP [92] [see Fig. 1.7(b)] and using strip waveguides

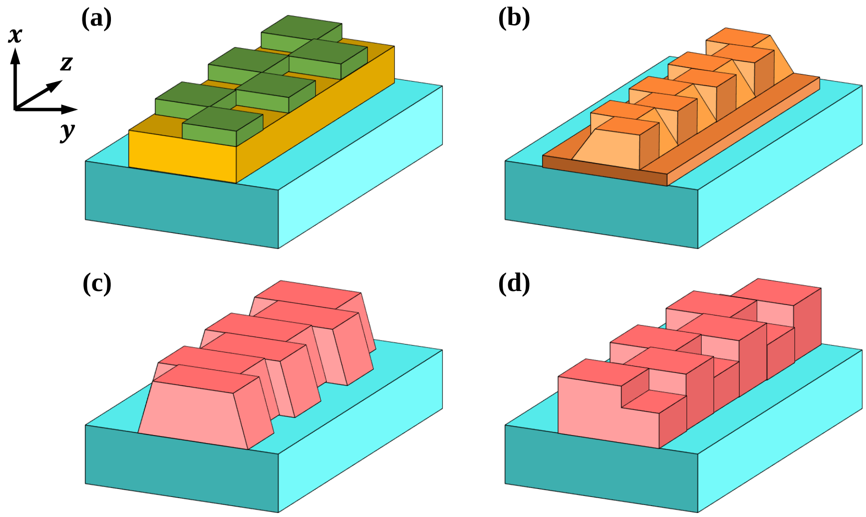

Figure 1.7: Schematic drawings of polarization-rotating Bragg gratings achieved by using (a) periodically loaded waveguides, (b) sidewall corrugations on a ridge waveguide with tilted sidewalls, (c) sidewall corrugations on an SOI strip waveguide with tilted sidewalls, and (d) corner corrugations on a regular SOI strip waveguide.

in SOI [94] [see Fig. 1.7(c)]. In those devices, the waveguide sidewalls were fabricated to have specific angles (55° in [92] and 89° in [94]) relative to the substrate, such that the optical symmetry to the horizontal axis in the transverse plane of the waveguide was broken, resulting in a polarization-rotating reflection at selected wavelengths. Here, I have proposed and demonstrated a third approach which uses partially-etched asymmetric Bragg gratings integrated on regular strip waveguides. Such devices have been demonstrated on the SOI platform [95–97, 128, 129].

1.3 About This Dissertation

1.3.1 Objective

The objective of this dissertation is to investigate the properties of sub-wavelength gratings and other periodic waveguide structures on the SOI platform and apply the propagation and diffraction properties that they can provide to study and develop novel photonic devices with improved operating characteristics and properties as compared to currently implemented technologies and approaches. The long-term objective of my work is to apply the benefits obtainable using these periodic structures to develop large-scale PICs with enhanced performance and enriched functionalities for numerous optical communication and sensing applications, such as high speed, high data-density, optical interconnects and enhanced bio-sensing systems.

1.3.2 Dissertation Organization

This dissertation is organized as follows:

In Chapter 2, broadband adiabatic 3 dB couplers are demonstrated using regular SOI rib and strip waveguides. The eigenmode evolution process is demonstrated for broadband even power splitting over 100 nm. The design, simulation, and characterization of adiabatic 3 dB couplers using SOI rib waveguides are demonstrated in Section 2.2 for TE mode operation and adiabatic 3 dB couplers using SOI strip waveguides are demonstrated in Section 2.3 for the TE mode and the TM mode operation.

In Chapter 3, broadband adiabatic 3 dB couplers are demonstrated using SWG waveguides for compact footprints and operating bandwidths of 130 nm. The properties of the fundamental and next higher-order TE modes of two-SWG-waveguide system are investigated using 3D FDTD band structures. The design, simulation, and characterization of SWG adiabatic 3 dB couplers are demonstrated.

In Chapter 4, ultra-broadband adiabatic 3 dB couplers are demonstrated using strip-assisted, SWG waveguides for compact footprints and ultra-broad operating bandwidths of $>$185 nm. The properties of the fundamental and next higher-order TE modes of the two-SWG-assisted-waveguide system are investigated. The design, simulation, and characterization of SWG-assisted adiabatic 3 dB couplers are demonstrated.

In Chapter 5, broadband SWG contra-directional couplers (CDCs) are demonstrated using two asymmetric SWG waveguides for bandwidths $>$30 nm and sidelobe suppressions $>$50 dB. The contra-directional coupling between the fundamental and the next higher-order TE modes of two-SWG-waveguide system are investigated. The design, simulation, and characterization of SWG CDCs are demonstrated.

In Chapter 6, polarization-insensitive wavelength filters are demonstrated using polarization-rotating Bragg gratings (PRBGs) to work at the same wavelengths for both TE and TM modes. The properties of wavelength-selective, polarization-rotation are studied and investigated. Both band-rejection filters and band-pass filters are demonstrated in Sections 6.1 and 6.2, respectively.

The dissertation is concluded in Chapter 7 with a brief summary and a discussion of possible future research directions.

Chapter 2

Broadband Adiabatic 3 dB Couplers in Silicon-on-Insulator Waveguides

In this chapter, broadband optical power splitters are demonstrated using adiabatic 3 dB couplers on conventional SOI waveguides. The adiabatic mode evolution processes of highly confined, guided optical modes in the two waveguide system are introduced in Section 2.1. Adiabatic 3 dB couplers using conventional SOI rib are shown in Section 2.2 for broadband TE mode operation. Adiabatic 3 dB couplers using SOI strip waveguides are shown in Section 2.3 for broadband TE mode and TM mode operation.

2.1 Eigenmode Evolution: an adiabatic process

Originally, the word "adiabatic" and the phrase "adiabatic process" referred to an isentropic process that occurs without the transfer of heat or mass of substances between a thermodynamic system and its surroundings. In an adiabatic process, energy is transferred to the surroundings only as work [130, 131]. It provides a rigorous conceptual basis for the theory used to expound the first law of thermodynamics and, as such, it is a key concept in thermodynamics to describe phenomena such as gas expansion and gas compression [132]. The definition and concept of an adiabatic process was later redefined in quantum mechanics [133, 134]. In quantum mechanics, when a system starts from a stationary eigenstate of the initial Hamiltonian, if the change of the Hamiltonian is made infinitely slow, it will pass through the corresponding stationary eigenstates of the Hamiltonian during the process and will end in the corresponding eigenstate of the final Hamiltonian [135].

Similarly, in integrated optics, we use the word "adiabatic" to describe a lossless mode evolution process of the guided mode in an optical waveguide system. In an optical waveguide system, when light starts to propagate in an eigenmode, if the change of the system (either by changing the waveguide's physical dimensions or by changing its refractive indices) is made gradual, light will remain in the same order eigenmode throughout the system. During the propagation, no energy will be transferred to other eigenmodes of the system, and, therefore, the mode evolution process is considered to be an adiabatic process.

Mode evolution based adiabatic processes have been employed in many silicon photonic devices including waveguide tapers [136], power splitters [73, 137], polarization splitters [138, 139] and rotators [140], and mode converters [141, 142]. In this dissertation, the adiabatic processes evolving the fundamental and next higher-order eigenmode of a pair of asymmetric SOI waveguides into those of a pair of symmetric SOI waveguides, respectively, are used to implement adiabatic 3 dB couplers for broadband optical power splitting. Adiabatic 3 dB couplers are 2×2 couplers that are used for coupling/splitting light evenly. These couplers are essentially wavelength independent and less sensitive to fabrication variations, particularly as compared to other couplers such as symmetric DCs or MMI couplers. In a conventional symmetric DC consisting of two identical waveguides, when

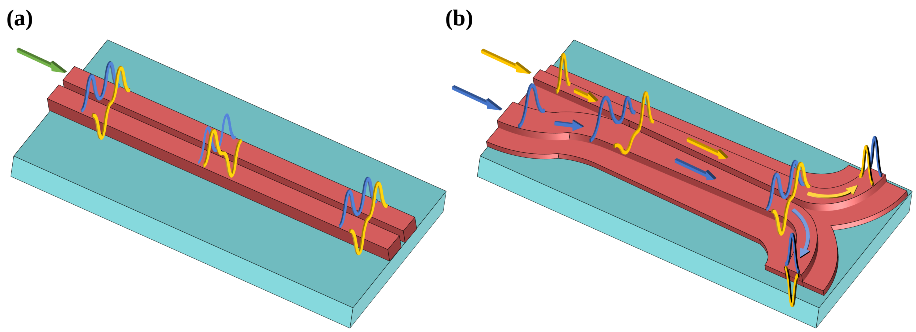

Figure 2.1: Perspective view of (a) a conventional, directional coupler with its fundamental (blue line) and next higher order mode (yellow line) excited at the input and (b) an adiabatic 3 dB coupler with only either the fundamental (blue line) or the next higher order (yellow line) mode excited.

light is injected into one of the waveguide, both the fundamental (even) and the next higher order (odd) eigenmodes of the two symmetric waveguide system are excited initially and interfere with each other as they propagate along the DC which results in the power transferring back and forth between the two waveguides [see Fig. 2.1(a)]. In such a DC, due to the waveguide symmetry, the described operation is independent of the end into which the light is injected [either the left-hand side or the right-hand side of Fig. 2.1(a)]. In an adiabatic 3 dB coupler, as shown in Fig. 2.1(b), only one eigenmode of the two waveguide system, either the fundamental or the next higher order mode, is excited when light is injected into either the wide or the narrow waveguide of the two asymmetric waveguides, at the left-hand side of Fig. 2.1(b), respectively. The excited mode, either the fundamental or next higher order mode, will evolve into the same order eigenmode of the two symmetric waveguide system, at the right-hand side of Fig. 2.1(b), for broadband power splitting. The adiabatic 3 dB coupler also works in reverse when light is injected into one of the two symmetric waveguides. However, when light is injected into one of the two symmetric waveguides, both the fundamental and next higher-order modes are excited equally and evolve into the same order system modes of the two asymmetric waveguides, at the other end of the coupler, respectively. More details on the mode evolution processes in adiabatic couplers can be found in Section 2.2.

2.2 Adiabatic 3 dB Coupler on SOI Rib Waveguides*

During the past two decades, adiabatic 3 dB couplers have been developed and fabricated using various types of waveguide materials, such as $LiNbO_3$ [143], SiO_2 [144], Polymers [145], and SOI [73]. Among these materials, SOI waveguides provide a high refractive index contrast that enables extreme device miniaturization and, thus, allows for the large-scale integration of photonic circuits. In 2006, Solehmainen et al. [73] demonstrated the first SOI adiabatic 3 dB coupler on 3.5-μm-wide silicon rib waveguides with a coupling length of 250 μm and obtained an Mach-Zehnder interferometer (MZI) extinction ratio (ER) of 15-20 dB. In 2008, Spector et al. [146] designed and integrated an SOI adiabatic 3 dB coupler, with a coupling length of 130 μm, into an MZI based electro-optic modulator and obtained a modulation depth of 22% ($\sim$6.6 dB) at a wavelength of 1550 nm. In 2010, Cao et al. [74] optimized the 3 dB coupler on SOI strip waveguides with a coupling length of 200 μm and measured an ER of $>$10 dB over the wavelength range from 1555 nm to 1640 nm.

Here, I present design and experimental results for a broadband SOI rib waveguide based adiabatic 3 dB coupler. As compared to SOI strip waveguides, SOI rib waveguides are less sensitive to sidewall roughness, which are more tolerant to fabrication variations [147]. In comparison with previous work [73, 74, 146], the rib waveguide geometry is compact, having a coupling length of 100 μm, and achieves broadband even splitting with an average normalized power splitting ratio of 52.90% /47.10% over a wavelength range of 100 nm (from 1500 nm to 1600 nm).

2.2.1 Design and Analysis

The adiabatic 3 dB coupler, as shown in Fig. 2.2, consists of four parts. In Region I, two parallel strip waveguides with 500 nm waveguide widths and a 3 μm gap distance are used as the two inputs and are tapered to 400 nm and 600 nm wide strip waveguides, respectively. They are then converted to corresponding rib waveguides with 1-μm-wide slabs on each side of the waveguides by using adiabatic linear

*A version of Section. 2.2 has been published: Han Yun, Wei Shi, Yun Wang, Lukas Chrostowski, and Nicolas A. F. Jaeger, "2×2 Adiabatic 3-dB coupler on silicon-on-insulator rib waveguides," *Proceedings of SPIE*, 8915, 89150V-1–89150V-6 (2013).

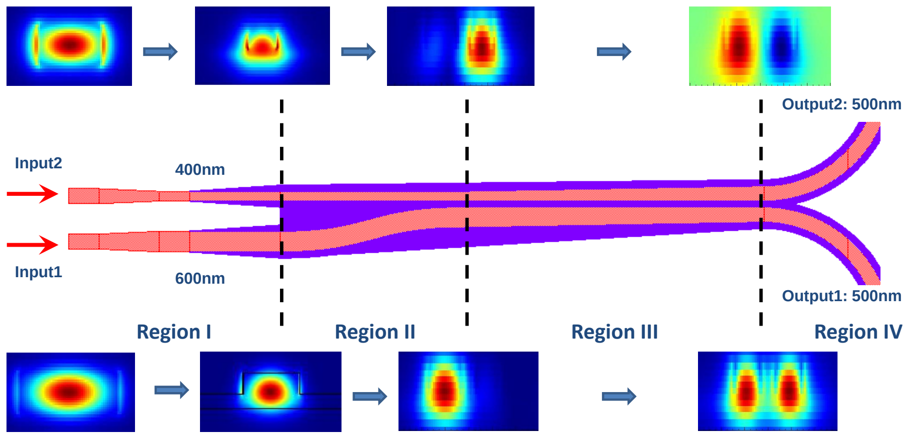

Figure 2.2: Schematic of an adiabatic 3 dB coupler on rib waveguides with simulation results.

tapers. In Region II, the two rib waveguides are brought together using an S-shape waveguide bend in one of the waveguides to reduce the gap distance from 3 μm to 200 nm. The S-shape waveguide bend in Region II is designed using Bezier curves to minimize the mode mismatch and thus reduce the waveguide bending loss [148]. In Region III, linear tapers are used to gradually convert the dissimilar input waveguides into two identical waveguides with a constant coupler gap of 200 nm. The widths of the two waveguides at the end of Region III are both 500 nm. In Region IV, the light in the two output waveguides is separated using two waveguide bends, to avoid further coupling.

I use the 3D FDTD method to simulate the layout shown in Fig. 2.2. When the light is injected into one of the input waveguides, the large asymmetry between the 400 nm and 600 nm wide rib waveguides in Regions I and II avoids coupling between the two waveguides (see Fig. 2.2). As shown in Fig. 2.2, the input light in the 600-nm-wide waveguide, which has the larger effective refractive index, excites the fundamental mode of the coupler in Region III while the input light in the 400-nm-wide waveguide excites the first order mode of the two waveguides due to its smaller effective refractive index. The length of the linear tapers in Region III are designed to be sufficiently long to have a gradual taper so that the excited modes at the interface between Regions II and III can be adiabatically transmitted

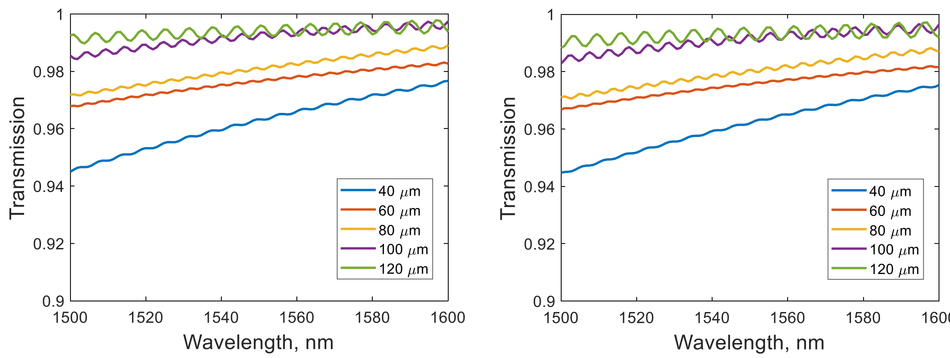

(a) (b)

Figure 2.3: Simulated eigenmode transmission spectral responses in Region III with various lengths for (a) the fundamental (even) and (b) the next higher-order (odd) TE modes of the two waveguide system.

into the even or odd mode of the symmetric 500-nm-wide waveguides at the end of Region III. In Region III, using the mode expansion monitors in FDTD Solutions (from Lumerical Inc.), I performed an overlap integral of the output field profile with the even/odd mode of the two waveguide system as solved by an eigenmode solver and, thus, obtained the eigenmode transmission efficiency for the power coupled from the excited even/odd mode at the input to the same order eigenmode at the output. As shown in Fig. 2.3, the eigenmode transmission was $> 98\%$ for both the even and odd TE modes over the wavelength range from 1500 nm to 1600 nm when using $\geq 100\ \mu$m for Region III. The excited even or odd mode automatically has half of the power in each waveguide which is then guided to one of the output waveguides by the two bending waveguides in Region IV. The simulated transmission responses of the adiabatic coupler, given in Fig. 2.4, show that the device has much smaller wavelength dependence and more robust 3 dB coupling over a wide spectral range, as compared to conventional DCs.

2.2.2 Fabrication and Measurement

The couplers were fabricated using electron beam lithography (EBL), with plasma etching, on an SOI platform. Fabrication was conducted at the University of Washington Microfabrication/Nanotechnology User Facility. The input strip waveguides

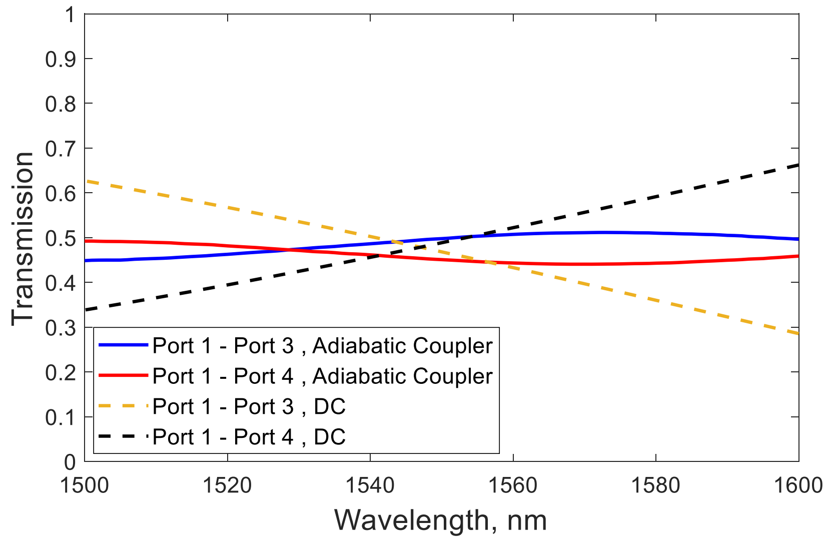

Figure 2.4: Simulated transmission responses of the rib-waveguide-based, adiabatic 3 dB coupler and a conventional, directional coupler.

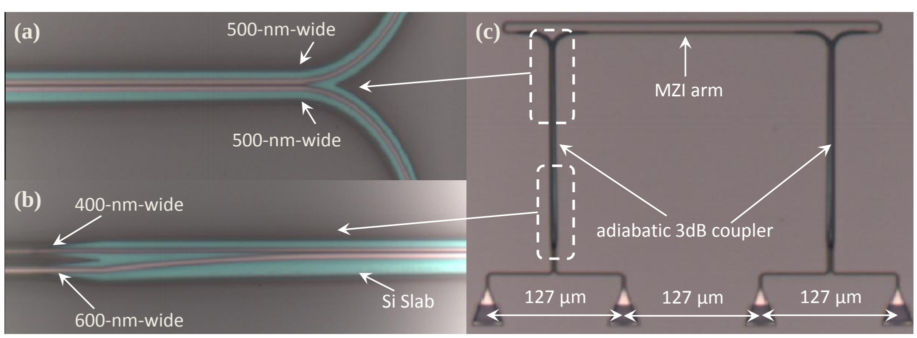

Figure 2.5: Optical images of a fabricated, unbalanced MZI with two adiabatic 3 dB couplers.

were 500-nm-wide by 220-nm-high silicon nanowires. The rib waveguides had 220-nm-high ribs with 90-nm-high slabs. Figures 2.5(a) and (b) show optical images of a fabricated 3 dB coupler. The linear tapers that converted the strip waveguides to rib waveguides were 15 μm long. The S-bend in Region II was 30 μm long and the linear tapers in Region III were 100 μm long. The radii of the waveguide bends in Region IV were 20 μm.

To demonstrate the performance of my adiabatic 3 dB couplers, I integrated two

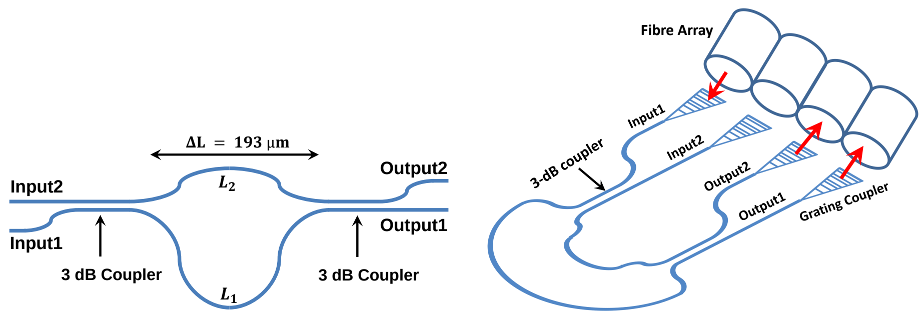

(a) (b)

Figure 2.6: Schematics of (a) a 2×2 unbalanced MZI with two adiabatic 3 dB couplers and (b) the MZI circuit used to make the measurements.

couplers into an unbalanced MZI with a length difference of 193 μm, where the output coupler was a 180-degree-rotated image of the input coupler [see Fig. 2.6(a)]. I designed the layout of the MZI, as shown in Fig. 2.6(b), for measurements using an optical fiber array. A fiber array containing four single-mode, TE-polarization-maintaining fibers, with 127 μm pitch, was used to simultaneously inject the input signal and to collect the two output signals. I integrated four TE-mode GCs [8] onto the input and output ports to couple the light into and out of the 2×2 MZI circuit. The GCs were parallel to each other and were placed on the chip with 127 μm spacing [see Fig. 2.5(c)], which enables us to align the fiber array to the two output ports at the same time and measure the two output responses simultaneously. The incident angle of the fiber array was adjusted to maximize the coupling efficiency at λ_0 = 1550 nm.

Measurements were taken at the two output ports of the 2×2 MZI when light was injected into one of the input ports. The MZI spectrum, after calibrating out the insertion loss (IL) introduced by the GCs, shows that ERs from both output ports were greater than 18 dB over a 100 nm wavelength range (see Fig. 2.7). The Input1-to-Output2 MZI responses, which were obtained between the 600-nm-wide rib waveguide of the input coupler and the 600-nm-wide rib waveguide of the output coupler, are given by the red line in Fig. 2.7 and show that a minimum ER of 27.2 dB was achieved over the 100 nm wavelength range, whereas a minimum ER of 33.4 dB was obtained over the wavelength range from 1520 nm to 1600 nm

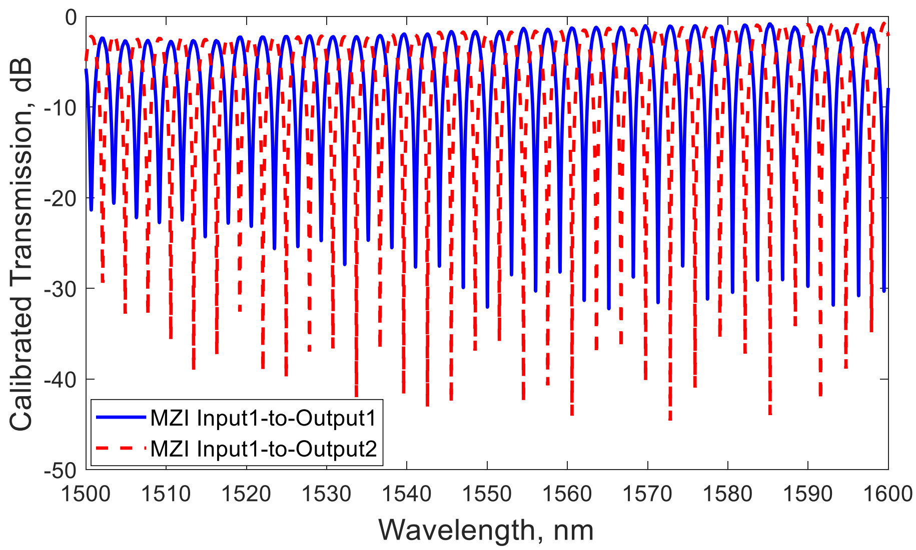

Figure 2.7: Measured MZI spectral responses after calibrating out the insertion loss from the grating couplers.

which covers the entire C-band and a portion of the L-band. A maximum ER of 42.5 dB was achieved at λ_o = 1572.8 nm. The measured spectrum also shows that the excess loss of the MZI is less than 2 dB, which indicates that the excess loss from each 3 dB coupler is less than 1 dB over the 100 nm wavelength range.

The normalized power cross coupling ratio is $K = k^2/(k^2+t^2)$, and the normalized power through coupling ratio is $T = 1-K = t^2/(k^2+t^2)$, where k and t are the real field cross and through coupling coefficients, respectively. K can be calculated from the ERs [149] which were extracted from the maxima from Output2 (i.e., the cross port) and corresponding minima from Output1 (i.e., the bar port) in the MZI spectra, assuming the propagation losses in the two MZI arms are negligible. The output electric field components of the MZI shown in Fig. 2.6(a) are given by:

$$\begin{bmatrix} E_{o1} \\ E_{o2} \end{bmatrix} = \begin{bmatrix} t \cdot e^{-j\phi_o} & k \cdot e^{-j\phi_e} \\ -k \cdot e^{-j\phi_o} & t \cdot e^{-j\phi_e} \end{bmatrix}^{-1} \begin{bmatrix} e^{-j\phi_1} & 0 \\ 0 & e^{-j\phi_2} \end{bmatrix} \begin{bmatrix} t \cdot e^{-j\phi_e} & -k \cdot e^{-j\phi_o} \\ k \cdot e^{-j\phi_e} & t \cdot e^{-j\phi_o} \end{bmatrix} \begin{bmatrix} E_{i1} \\ E_{i2} \end{bmatrix} \tag{2.1}$$

where E_{i1}, E_{i2}, E_{o1}, and E_{o2} represent the electric field component at Input1, Input2, Output1, and Output2, respectively. ϕ_e is the total propagation phase change along

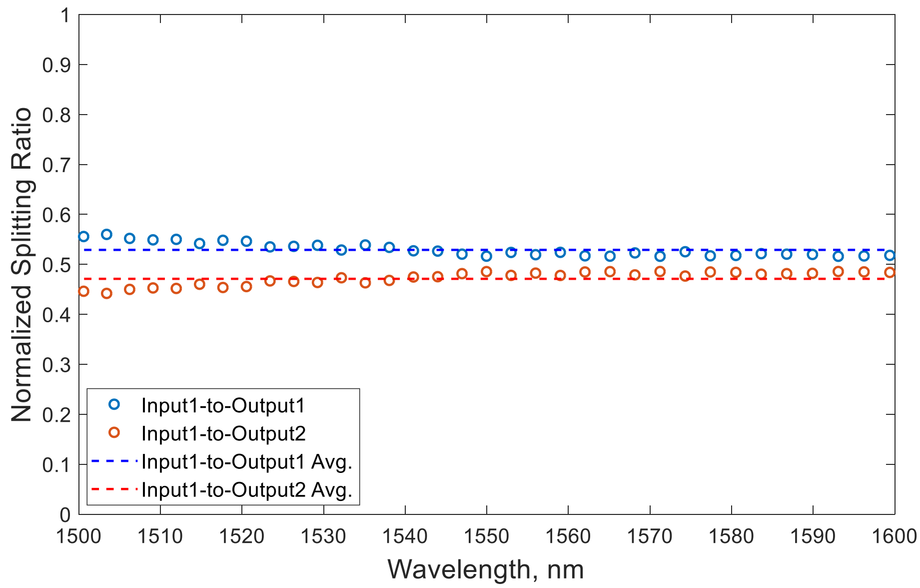

Figure 2.8: Calculated normalized power splitting ratio of the adiabatic 3 dB coupler and showing the average normalized power splitting ratio.

the adiabatic 3 dB coupler when the fundamental (even) mode is excited and ϕ_o is the total propagation phase change along the adiabatic 3 dB coupler when the next higher order (odd) mode is excited. ϕ_1 and ϕ_2 are the phase changes of the light propagating along the two unbalanced arms of the MZI with lengths L_1 and L_2, respectively. When light is injected into Input1, by solving Eq. 2.1, I can obtain the ERs of the normalized power intensity for Output1 and Output2:

$$\begin{aligned} ER_1 &= 10\log_{10}\left[\tfrac{(2kt)^2}{(t^2-k^2)^2}\right] \\ ER_2 &= 10\log_{10}\left[\tfrac{1}{0}\right] = \infty \end{aligned} \tag{2.2}$$

where ER_1 corresponds to the ER extracted from the maxima from Output2 and minima from Output1, and ER_2 corresponds to the ER extracted from the maxima from Output1 and minima from Output2. From Eq. 2.2, we can see that ER_2 is independent of the power splitting ratio and, therefore, K can only be calculated from ER_1 and is given by:

$$K = \frac{k^2}{k^2+t^2} = \frac{1}{2} \pm \sqrt{\frac{1}{10^{\frac{ER_1}{10}}+1}} \tag{2.3}$$

The normalized splitting ratios of the device are shown in Fig. 2.8. The average normalized splitting ratio, for the 100 nm wavelength range, was 52.90%/47.10%.

2.2.3 Discussion

For rapid prototyping, the rib-waveguide-based adiabatic 3 dB coupler was first demonstrated using electron beam lithography (EBL) tools. This device was later fabricated using both the 248 nm and the 193 nm DUV lithography processes that are provided by IME at Singapore. Fabricated using DUV lithography, this device has been widely used for building integrated photonic circuits including micro-ring-based optical gyroscopes [150], MZI modulators [151], Michelson interferometric modulators [65, 152], and optical switches [63, 64]. This device has also been included as a fixed cell in both the SiEPIC-EBeam-PDK for EBL tools and the SiEPIC-AMF-Library (custom library for the AMF DUV optical lithography process) [58].

2.3 Adiabatic 3 dB Coupler on SOI Strip Waveguides†

In Section 2.2, the rib-waveguide-based, adiabatic 3 dB coupler have shown broadband power splitting performance for the TE mode operation. However, it requires duo-etching processes to fabricate the slab layer and the rib layer, which increases the fabrication cost. In comparison with SOI rib waveguides, SOI strip waveguides require only a single-etch process for fabrication. In this work, I proposed and demonstrated two adiabatic 3 dB couplers using fully etched SOI strip waveguides for TE mode and TM mode operation, respectively. In comparison with previous work published on SOI strip waveguides [74], my TE-mode adiabatic 3 dB coupler has a more compact geometry, having a mode evolution length of 100 μm,

†A version of Section. 2.3 has been published: Han Yun, Zeqin Lu, Yun Wang, Wei Shi, Lukas Chrostowski, and Nicolas A. F. Jaeger, "2×2 Broadband adiabatic 3 dB couplers on SOI strip waveguides for TE and TM modes," in *CLEO (Conference on Lasers and Electro-Optics): 2015, (Optical Society of America, 2015)*, p. STh1F.8. (05/2015).

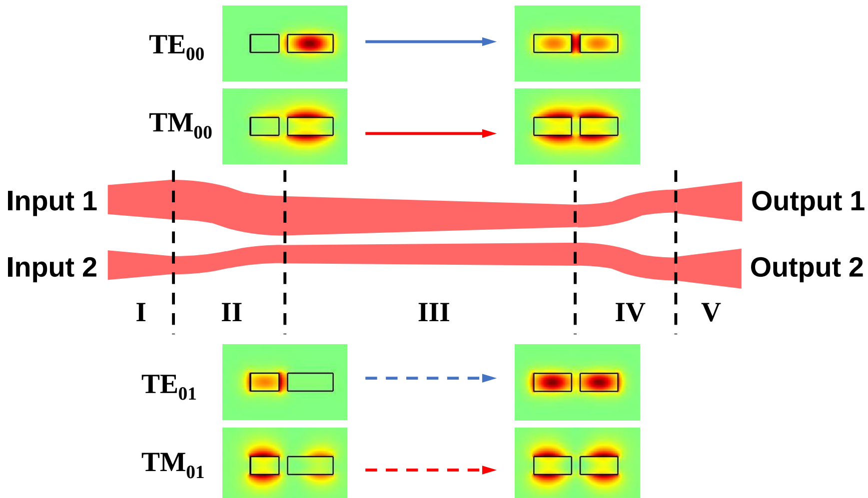

Figure 2.9: Schematic of an adiabatic 3 dB coupler on strip waveguides with simulated electric field intensity distributions of the fundamental (TE_{00}) and next higher-order (TE_{01}) quasi-TE modes and the fundamental (TM_{00}) and next higher-order (TM_{01}) quasi-TM modes of the two waveguide system.

and achieves more even splitting with an average normalized power splitting ratio of 46.55%/53.45% over a 100 nm wavelength range. My TM-mode adiabatic 3 dB coupler has a mode evolution length of 122 μm and achieves broadband even splitting with an average normalized power splitting ratio of 48.65%/51.35% over a 100 nm wavelength range.

2.3.1 Design and Simulation

I designed my adiabatic 3 dB couplers based on 220-nm-high SOI strip waveguides. The devices, as shown in Fig.2.9, consist of five regions. In Region I, two parallel 500-nm-wide strip waveguides, with a 3 μm gap distance, are used as the two inputs and are tapered to 550 nm and 350 nm wide strip waveguides, respectively. In Region II, the two waveguides are brought together using two adiabatic S-shape waveguide bends to reduce the gap distance from 3 μm to a narrow gap distance, G. The S-shape waveguide bends in Region II are designed using Bezier curves to minimize the mode mismatch and thus reduce the waveguide bending

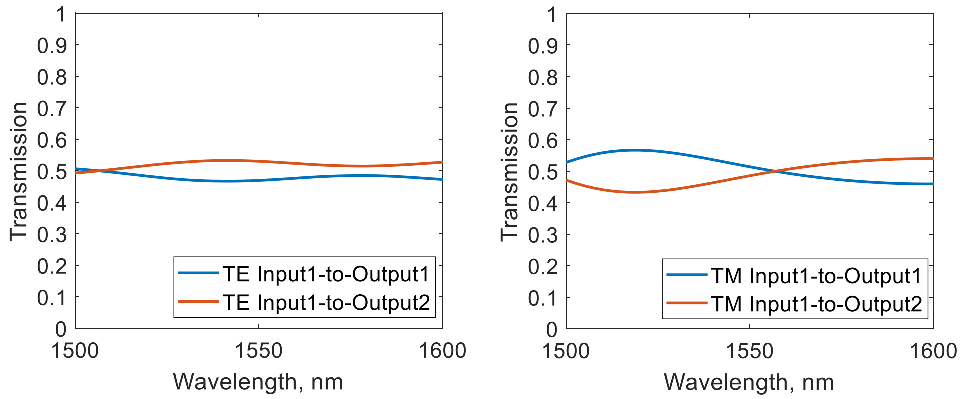

(a) (b)

Figure 2.10: Simulated transmission responses of (a) TE-mode and (b) TM-mode, strip-waveguide-based, adiabatic 3 dB couplers.

loss. In Region III, linear tapers are used to gradually convert the dissimilar input waveguides into two identical waveguides while keeping a constant G. The two waveguides at the end of Region III are both 450 nm wide. To avoid further coupling in Region IV, the light in the two output waveguides is separated to 3 μm using another two S-shape waveguide bends. In Region V, the two output waveguides are linearly tapered to be 500 nm wide.

To obtain sufficient eigenmode transmission efficiency for mode evolution, I chose $G = 100$ nm and the mode evolution length to be 100 μm and 122 μm for the TE and TM modes, respectively. Using the same method described in Sec. 2.2, I simulated the devices using the 3D FDTD solver in FDTD Solutions from Lumerical Inc., and obtained the transmission responses from 1500 nm to 1600 nm. The simulation results of the designed adiabatic couplers in Fig. 2.10(a) and (b) show small wavelength dependence and robust 3 dB splitting over a wide spectral range for both the TE and TM modes.

2.3.2 Experimental Results

My adiabatic 3 dB couplers were fabricated using electron-beam lithography, with plasma etching, on the SOI platform. To demonstrate the performance of my couplers, I integrated two couplers into an unbalanced MZI with a length difference of

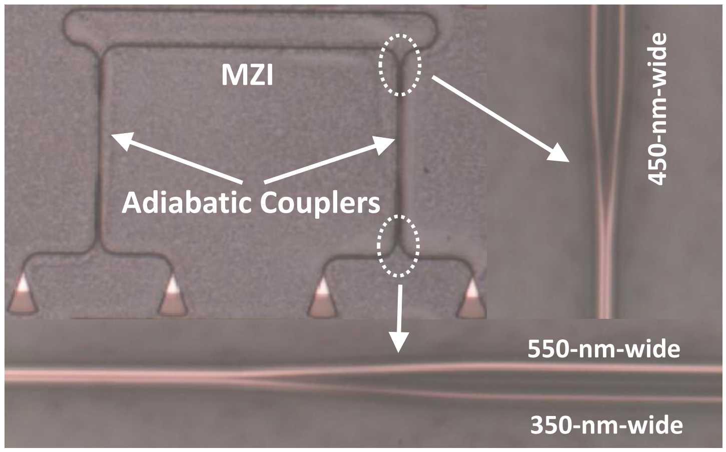

Figure 2.11: Optical images of a fabricated, unbalanced MZI with two adiabatic 3 dB couplers.

254 μm (see Fig. 2.11). Fully etched TE-mode and TM-mode GCs [8] were used to couple the light into and out of the MZI circuits. The MZI spectrum over a 100 nm wavelength range, after calibrating out the insertion loss introduced by the GCs, shows that the ERs from both output ports were $>$15 dB for the TE modes and were $>$20 dB for the TM modes [see Fig.2.12(a) and (b)], where maximum ERs of 49 dB and 55 dB were achieved for the TE and TM modes, respectively. Using Eq. 2.3, I calculated the power splitting ratios of the strip-waveguide-based, adiabatic 3 dB couplers and, as shown in Fig.2.13(a) and (b), obtained average splitting ratios of 46.55%/53.45% and 48.65%/51.35% over the 100 nm wavelength range from 1500 nm to 1600 nm for TE-mode and TM-mode couplers, respectively.

2.3.3 Discussion

In this work, two strip-waveguide-based adiabatic couplers were designed for TE mode operation and, for the first time, for TM mode operation, respectively. Based on this work and in direct collaboration with our group, polarization-independent adiabatic 3 dB couplers were designed and demonstrated using SOI strip waveguides [69], by optimizing the mode evolution region.

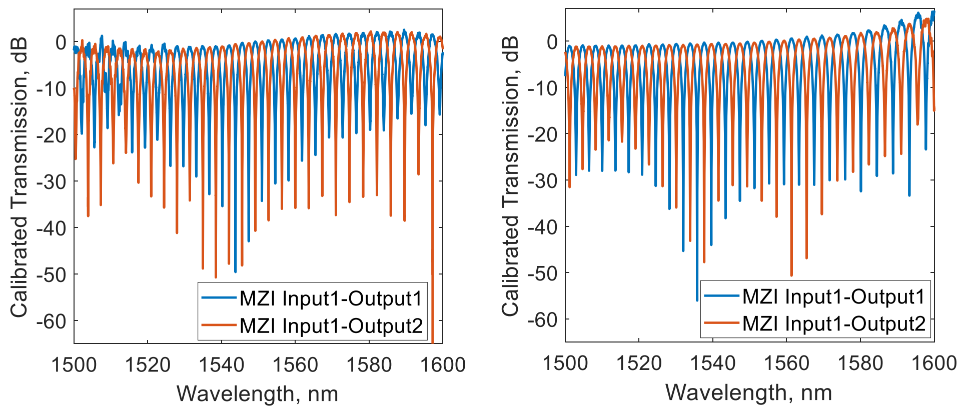

(a) (b)

Figure 2.12: Measured MZI spectral responses after calibrating out the insertion loss from the grating couplers for (a) the TE mode and (b) the TM mode, strip-waveguide-based, adiabatic 3 dB couplers.

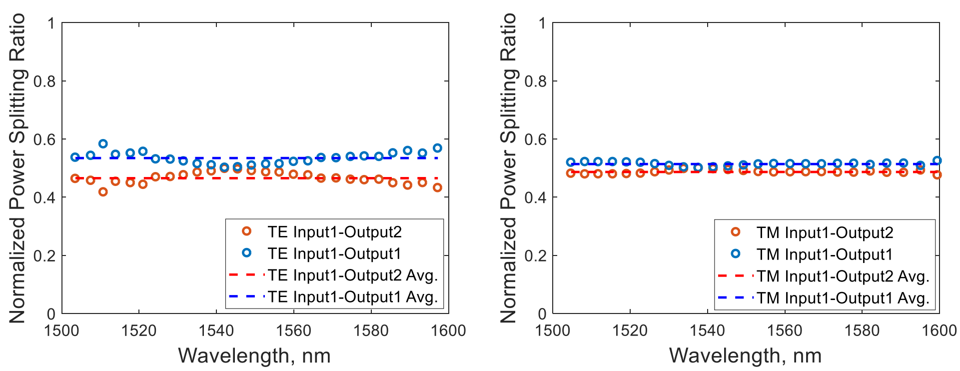

(a) (b)

Figure 2.13: Calculated normalized power splitting ratio of the adiabatic 3 dB coupler and showing the average normalized power splitting ratio for (a) TE mode and (b) TM mode.

Chapter 3

Broadband Sub-wavelength Grating Adiabatic 3 dB Couplers*

In this chapter, the design of a compact, broadband, 2×2 adiabatic 3 dB coupler is demonstrated utilizing SWG waveguides for TE mode power splitting. In this device, two SWG waveguides that support the fundamental and next higher-order TE modes and have tapered waveguide widths are used to achieve adiabatic mode evolution in the two-waveguide system for broadband 3 dB power splitting. The SWG waveguide geometry is very compact, having a total coupler length of only 50 μm, and achieves 3 dB power splitting over a wavelength range of 130 nm with an imbalance of no greater than ±0.4 dB and does so with low excess losses of less than 0.5 dB. Furthermore, the SWG waveguide design only requires a single-etch process for fabrication.

*A version of Chapter 3 has been published: Han Yun, Yun Wang, Fan Zhang, Zeqin Lu, Stephen Lin, Lukas Chrostowski, and Nicolas A. F. Jaeger, "Broadband 2×2 adiabatic 3-dB coupler using silicon-on-insulator sub-wavelength grating waveguides," *Optics Letters*, vol. 41, pp.3041-3044, 2016.

3.1 Motivation

The adiabatic couplers presented in Chapter 2 have shown broadband performance on the SOI platform. However, due to the high-index-contrast between the cladding (SiO_2) layer and the waveguide (Si) layer, SOI adiabatic 3 dB couplers usually suffer from large device footprints. For conventional silicon waveguides (strip or ridge waveguides) on an SOI platform, the excited system modes are highly confined in the two waveguides. To obtain adequate coupling and efficient adiabatic mode evolution of the excited system modes, the mode evolution region of an adiabatic 3 dB coupler typically needs to be several hundred micrometers long. In recent work, many designs have been proposed and demonstrated to reduce the footprints of adiabatic 3 dB couplers, such as simultaneously tapering the gap width between the two waveguides [68] or using a narrow, 100 nm, gap distance [69, 75]. Nevertheless, in these designs, the mode evolution regions are still around 100 μm.

SOI SWG structures can be used to further reduce the footprints of adiabatic 3 dB couplers. As discussed in Section. 1.2.2, SWG structures offer the flexibility to tailor the refractive index and the dispersion properties of SOI photonic devices [109] and, thus, provide a means to reduce the device footprint. SWG waveguides support lossless optical mode propagation when period lengths are smaller than π/β, where β is the propagation constant of the light in the structure. Therefore, they can be engineered to let the light "see" less high-index waveguide material and more low-index cladding material. This can be used to make the optical modes less dispersive and/or less sensitive to fabrication imperfections. Many SWG based components have been proposed or demonstrated on SOI platforms, such as micro-ring resonators (MRRs) [120], Bragg-grating filters [122], multimode interference (MMI) couplers [124], and directional couplers [125]. 2x2 SWG adiabatic 3 dB couplers, however, have not yet been demonstrated. In this work, for the first time, I proposed and demonstrated the design of a compact, broadband, 2×2 adiabatic 3 dB coupler utilizing SWG waveguides for TE mode power splitting [76]. As compared to regular SOI waveguides, SOI SWG waveguides enable more compact designs, with wider bandwidths, and have greater tolerance to fabrication variations.

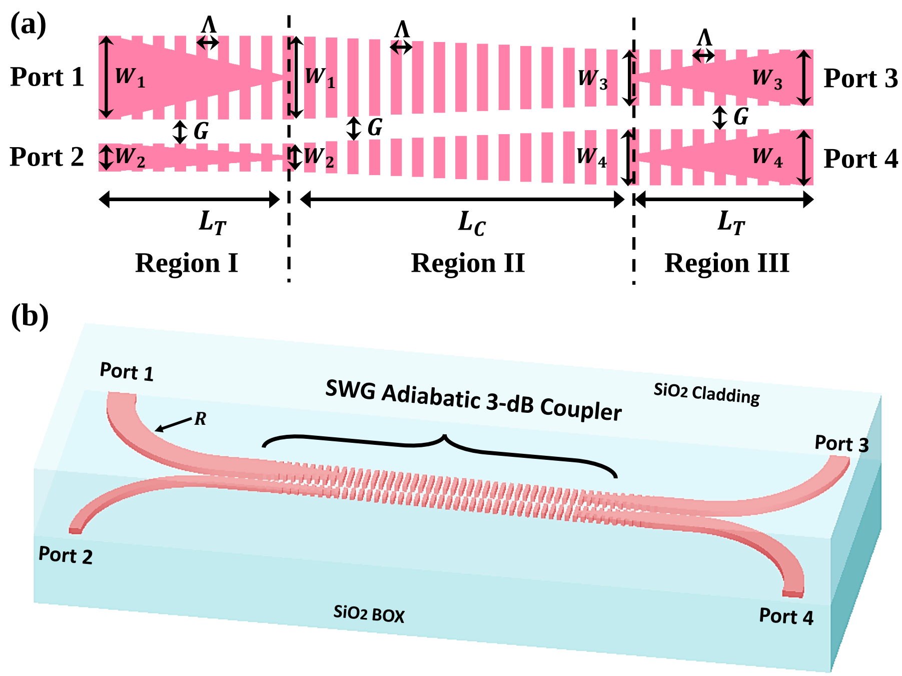

Figure 3.1: Schematics of an SWG adiabatic 3 dB coupler with the design parameters labeled: (a) 2D top view and (b) 3D perspective view.

3.2 Design and Simulation

For my SWG adiabatic 3 dB coupler, the design uses a 220 nm thick silicon layer, a 2 μm thick silicon dioxide upper cladding layer, and a 3 μm thick buried oxide layer (see Fig. 3.1). The coupler region consists of three parts, as shown in Fig. 3.1 (a). Region I consists of two uncoupled strip-to-SWG waveguide converters that convert the two strip waveguides that have widths W_1 and W_2, respectively, on the left hand side of the region to two SWG waveguides that also have widths W_1 and W_2, respectively, on the right hand side of the region, and vice versa. Each strip-to-SWG waveguide converter consists of an SWG waveguide with width W_1 (or W_2) and a waveguide horn with its width linearly tapered from W_1 (or W_2) to the minimum feature size (which is 60 nm in our case) provided by the fabrication process. Thus, the effective indices of the lowest order even and the lowest order odd modes of the two strip waveguide system at the left hand side of Region I are tapered to those of the two SWG waveguide system at the right hand side of the region, respectively. The length of Region I is L_T. Region II consists of two linearly tapered SWG waveguides that allow the even (or odd) mode of the two waveguide system injected to the left hand side of the region to evolve into the even (or odd) mode on the right hand side of the region, and vice versa. The length of Region II is L_C, and the widths of the two SWG waveguides are tapered from W_1 and W_2 on the left hand side of the region to W_3 and W_4 on the right side of the region, respectively. In Region III, I use two coupled SWG-to-strip waveguide converters to convert the two SWG waveguides that have widths W_3 and W_4, respectively, on the left hand side of the region to two strip waveguides that also have widths W_3 and W_4, respectively, on the right hand side of the region, and vice versa. Each SWG-to-strip waveguide converter consists of an SWG waveguide with width W_3 (or W_4) and a waveguide horn with its width linearly tapered from 60 nm to W_3 (or W_4). Thus, the effective indices of the lowest order even and the lowest order odd modes of the two SWG waveguide system at the left hand side of Region III are tapered to those of the two strip waveguide system at the right hand side of the region, respectively. Region III also has the length, L_T, and allows the excited even (or odd) mode (from Region II) to propagate unaltered. I use four 90 degree waveguide bends with radii $R = 15\ \mu$m for the input and output ports of my device [see Fig. 3.1(b)] where the widths of Ports 1 and 2 are W_1 and W_2, respectively, and the widths of Ports 3 and 4 are W_3 and W_4, respectively.

In order to excite only one system mode (either the lowest order even or the lowest order odd TE mode) of the two waveguide system, I use $W_1 = 560$ nm and $W_2 = 380$ nm in my device. For TE mode 3 dB power splitting I use $W_3 = W_4 =$ 470 nm. All of the SWG structures have the same period, Λ, with a duty cycle, ff, of 50%, to minimize the power losses at the interfaces between Regions I and II and between Regions II and III, and all of the waveguides in the coupler have the same gap distance, G, of 150 nm. I use $L_T = 15\ \mu$m for the waveguide converters in Regions I and III and obtained simulated insertion losses of less than 0.01 dB over the wavelength range from 1490 nm to 1620 nm. I use $L_C = 20\ \mu$m to obtain sufficient adiabatic mode evolution for the excited system modes in Region II. For larger values of Λ, Bragg diffraction may limit the operating bandwidth of the adiabatic 3 dB coupler. Hence, for broadband operation, Λ is selected such that

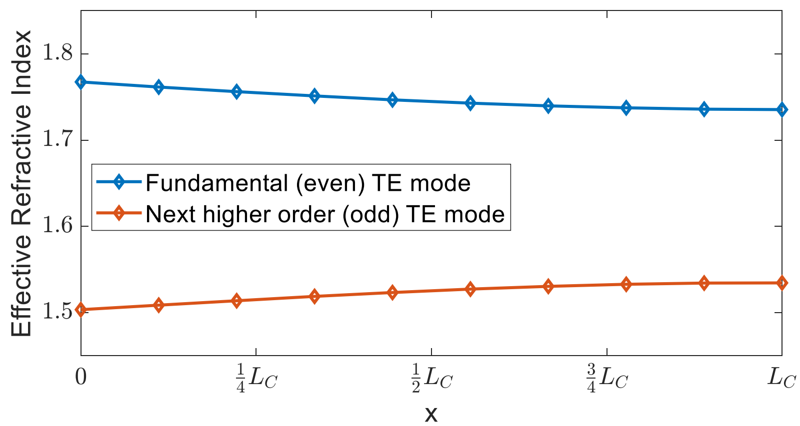

Figure 3.2: Calculated effective indices of the Floquet-Bloch modes, for the even and odd TE modes, as functions of the propagation position, x, in Region II of the SWG adiabatic 3 dB coupler at $\lambda_{min} = 1490$ nm.

$\Lambda \ll \lambda_{min}/(2 \cdot n_{SWG,\,eff})$ [124] where λ_{min} is the minimum operating wavelength and $n_{SWG,\,eff}$ is the effective index of the fundamental Floquet-Bloch mode in the two SWG waveguides at λ_{min}. I used 3D FDTD based band structure calculations with Bloch boundary conditions applied in the mode propagation direction in FDTD Solutions, from Lumerical, Inc., to simulate the periodic structure in my device and obtained the effective indices of the excited Bloch modes. In my case, $\lambda_{min} = 1490$ nm, and $n_{SWG,\,eff}$ changes from 1.7674 to 1.7353 for the even TE mode and from 1.5034 to 1.5347 for the odd TE mode (see Fig. 3.2), when the light propagates from the left hand side ($x = 0$) to the right hand side ($x = L_C$) of Region II of the SWG adiabatic 3 dB coupler. Hence, here I use $\Lambda = 200$ nm $\ll$ 1490 nm/(2×1.7674) = 421.5 nm.

I simulated my device, using the 3D FDTD solver, with a 5 nm mesh. As shown in Fig. 3.3, the excited TE mode injected into Port 1 was adiabatically coupled into the even TE mode of the two output waveguides, Ports 3 and 4, for a 50-μm-long ($2\times L_T + L_C = 50$ μm) coupler at $\lambda = 1550$ nm. Also, as expected, when the excited TE mode was injected into Port 2, it was adiabatically coupled into the odd TE mode of the two output waveguides at Ports 3 and 4. As a comparison, I also simulated the conventional adiabatic 3 dB coupler design from [75] with the same waveguide geometry, gap distance, and coupler length. Using the mode

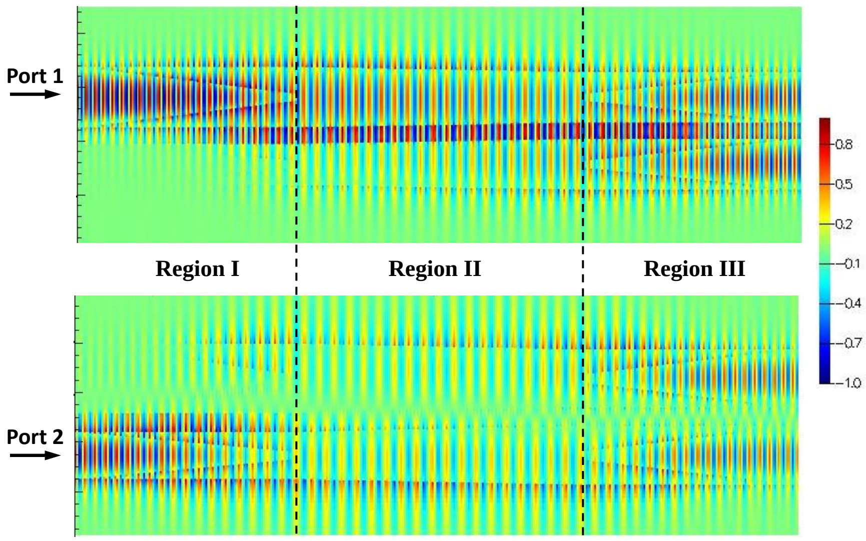

Figure 3.3: Top view of the simulated electric field distributions of the fundamental and the next higher-order TE modes for an SWG adiabatic 3 dB coupler when light is injected at Ports 1 and 2, respectively, at $\lambda = 1550$ nm.

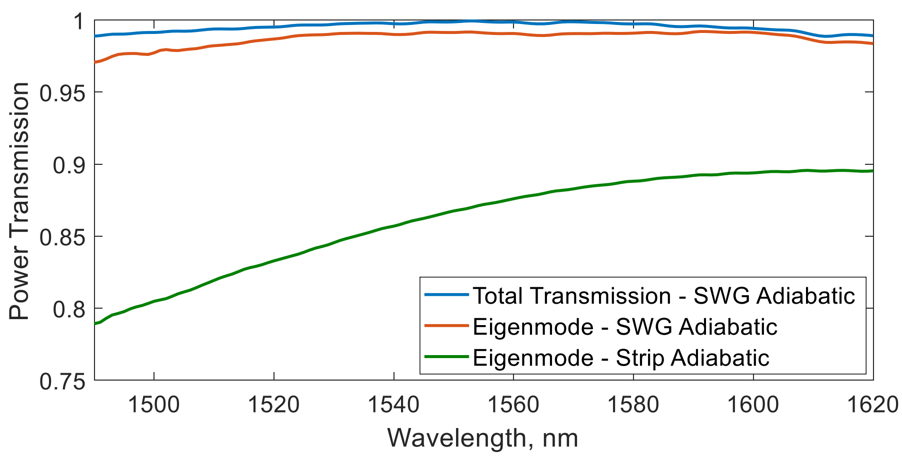

Figure 3.4: Simulated total transmission and eigenmode transmission spectra for an SWG adiabatic 3 dB coupler and the eigenmode transmission spectrum for a conventional adiabatic 3 dB coupler using strip waveguides.

expansion monitors in FDTD Solutions, I performed an overlap integral of the output field profile with the eigenmode of the two waveguide system as solved by an eigenmode solver and, thus, obtained the eigenmode transmission efficiency for the power coupled from the excited eigenmode at the input to the same order eigenmode at the output. As shown in Fig. 3.4, the eigenmode transmission for my SWG adiabatic 3 dB coupler was >97% for the even TE mode over the wavelength range from 1490 nm to 1620 nm, whereas the eigenmode transmission efficiency obtained for the conventional adiabatic 3 dB coupler was <90%.

I explored the fabrication tolerances of my design by simulating the eigenmode transmission response for the lowest order even and lowest order odd TE modes as functions of λ for various values of ΔH, ΔW, and Δl, where ΔH is the waveguide thickness variation, ΔW is the waveguide width variation, and Δl is the SWG groove length variation. Here $\Delta l = \Delta ff \cdot \Lambda$, where Δff is the variation of ff. While varying the waveguide widths, I included the corresponding gap variation by maintaining a constant center-to-center distance for the two waveguides. In my simulations, I used $\Delta H = \pm 20$ nm and $\Delta W = \Delta l = \pm 20$ nm to account for the types of fabrication process variations that may occur in commercially available silicon photonics SOI fabrication processes [153]. As shown in Fig. 3.5, the eigenmode transmission efficiency, over the 130 nm wavelength range, is not highly sensitive to these variations, which indicates that my coupler design is tolerant to possible fabrication variations.

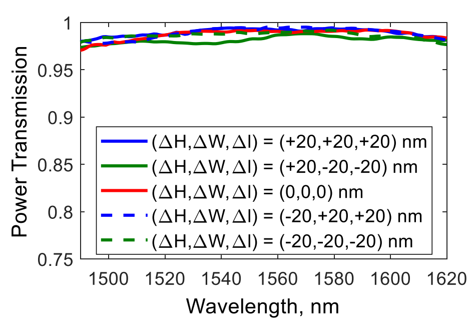

(a)

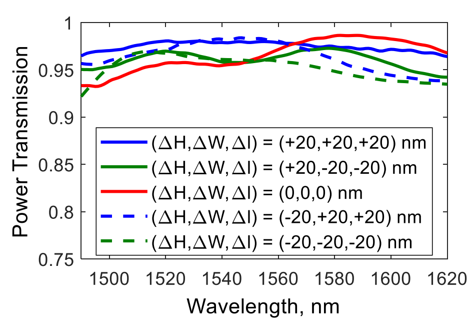

(b)

Figure 3.5: Simulated eigenmode transmission spectral responses for an SWG adiabatic 3 dB coupler with $\Delta H = \pm 20$ nm and $\Delta W = \Delta l = \pm 20$ nm for the (a) even and (b) odd TE modes.

3.3 Fabrication and Measurements

My SWG adiabatic 3 dB couplers were fabricated using electron-beam lithography, with plasma etching, on an SOI platform by Washington Nanofabrication Facility at the University of Washington. Figure 3.6(a) shows scanning electron microscope (SEM) images of sections of a fabricated SWG adiabatic 3 dB coupler with $\Lambda = 200$ nm and $G = 150$ nm. To demonstrate the performance of my couplers, as shown in Fig. 3.6(b), I integrated two identical couplers into an unbalanced MZI [15, 75] with a length difference of 164 μm. Broadband SWG TE-mode GCs [12] were used to couple light into and out of the MZI circuit. I characterized my device using a test setup [50] that maximized the optical power coupled into and out of the grating couplers during the measurements. In the test setup, a fiber array containing four single-mode, TE-polarization-maintaining fibers, were used to simultaneously inject the input light and to collect the light at the two outputs. An Agilent 81600B tunable laser was used as the light source and the two optical power sensors in an Agilent 81635A were used to detect the output powers.

The MZI spectra over a 130 nm wavelength range, after calibrating out the insertion losses introduced by the grating couplers, show that the ERs from both

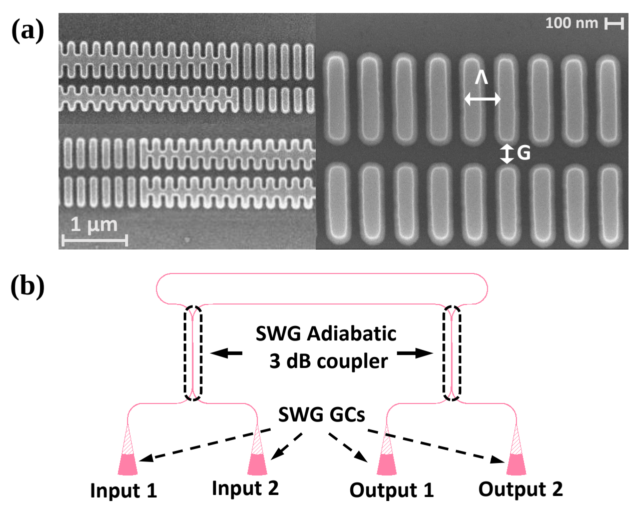

Figure 3.6: (a) SEM images of sections of a fabricated SWG adiabatic 3 dB coupler. (b) Fabrication mask layout of the unbalanced MZI structure with two identical SWG adiabatic 3 dB couplers.

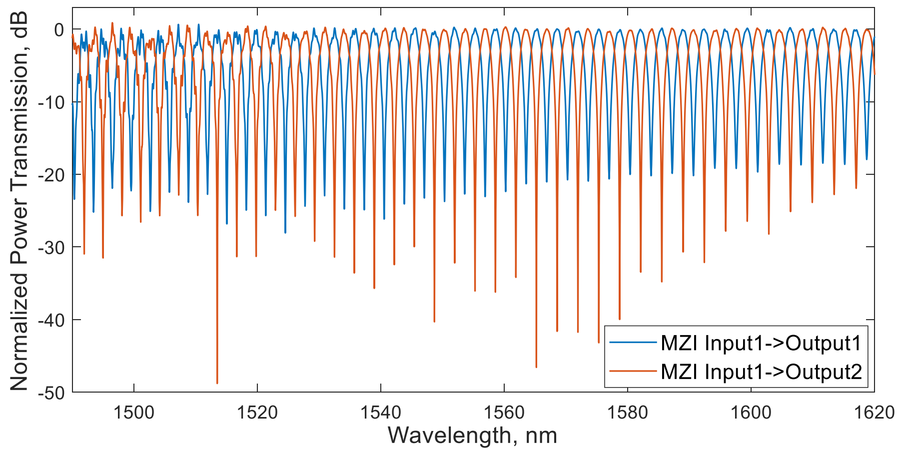

Figure 3.7: Measured MZI spectral responses of my SWG adiabatic 3 dB coupler after calibrating out the insertion losses of the grating couplers.

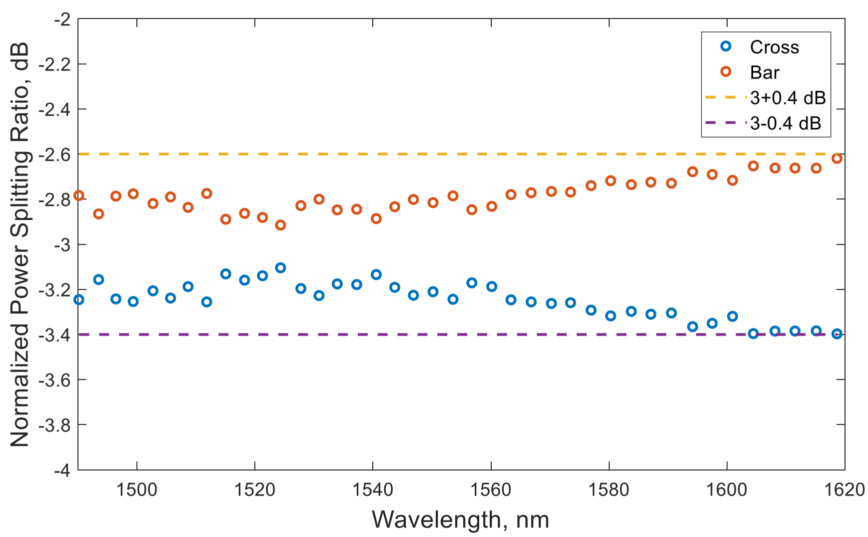

Figure 3.8: Calculated normalized power splitting ratios of my SWG adiabatic 3 dB coupler with $\leq \pm$ 0.4 dB imbalance.

output ports were >18 dB for the even mode (see Fig. 3.7), where a maximum ER of 49 dB was obtained. As shown in Fig. 3.8, I extracted the normalized power splitting ratios from the ERs of the measured MZI responses using the method described in Section 2.2 and obtained 3 dB power splitting ratios with $\leq \pm 0.4$ dB

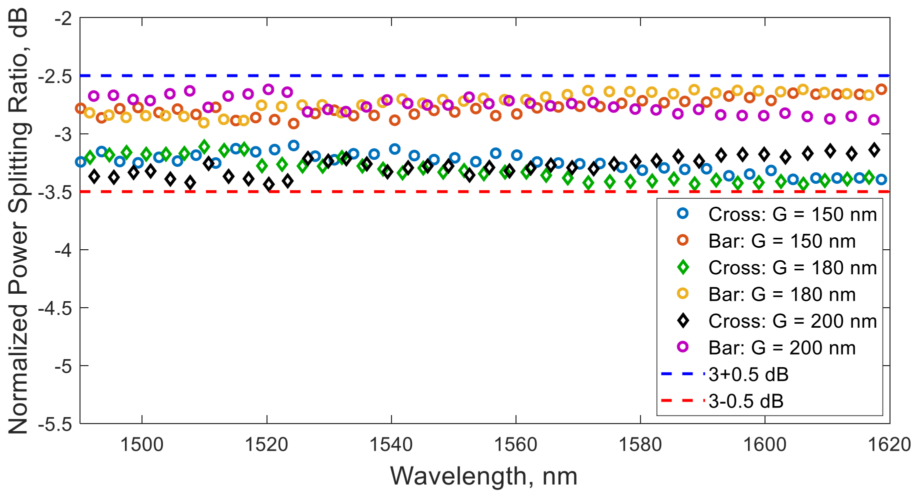

Figure 3.9: Calculated, normalized, power splitting ratios for SWG adiabatic 3 dB couplers with gap distances of 150 nm, 180 nm, and 200 nm and with $< \pm$ 0.5 dB imbalance.

imbalance over the wavelength range from 1490 nm to 1620 nm. The measured spectra also show that the excess loss of the MZI is less than 1 dB, which indicates that the excess loss from each 3 dB coupler is less than 0.5 dB over the 130 nm range.

SWG adiabatic 3 dB couplers with gap distances of 180 nm and 200 nm were also fabricated. As shown in Fig. 3.9, all of the devices (including the one with $G =$ 150 nm) provided broadband 3 dB power splitting ratios with $< \pm 0.5$ dB imbalance over the 130 nm wavelength range. This indicates that my SWG adiabatic 3 dB coupler provides design flexibility.

Chapter 4

Ultra-broadband SWG-assisted Adiabatic 3 dB Couplers*

In this chapter, I propose and demonstrate a compact, ultra-broadband, 2×2 adiabatic 3 dB coupler using SOI strip waveguides assisted by SWGs. In this device, two tapered SWG-assisted SOI strip waveguides achieve an adiabatic mode evolution of the two lowest-order TE modes, in a two waveguide system, for broadband 3 dB power splitting. Theory predicts that the proposed coupler will operate from 1200 nm to 1700 nm. I have been able to measure the performance of a device with a 15 μm long mode evolution region that achieves even, broadband power splitting over the 185 nm wavelength range of our tunable laser with an imbalance of less than ±0.3 dB and with low excess losses of <0.11 dB.

*A version of Chapter 4 has been published: Han Yun, Lukas Chrostowski, and Nicolas A. F. Jaeger, "Ultra-broadband 2×2 adiabatic 3 dB coupler using subwavelength-grating-assisted silicon-on-insulator strip waveguides," *Optics Letters*, 43, pp.1935-1938, 2018.

4.1 SWG-assisted Strip Waveguides for Ultra-broad Operation Bandwidth

The adiabatic 3 dB couplers demonstrated in Chapter 3 used two SWG waveguides and achieved an operating bandwidth of 130 nm (from 1490 nm to 1620 nm). However, this design limited the device operating bandwidth to wavelengths below 1630 nm. Above 1630 nm, due to the low equivalent refractive indices of the narrower waveguide of the two SWG waveguides, the lowest-order odd eigenmode was not guided by the adiabatic 3 dB coupler. To further extend the operation bandwidth, SWG-assisted strip waveguides are proposed and designed. SWG-assisted strip waveguides consisting of a narrow central strip waveguide and wide symmetric sub-wavelength fins are engineered to have much lower refractive indices than conventional strip or ridge waveguides, but higher refractive indices than conventional SWG waveguides, and, thus, enable compact designs with wider operating bandwidths. As compared to previous work [76], the proposed device is very compact, having a mode evolution region of only 15 μm and a total length of 35 μm, and is designed to operate from 1200 nm to 1700 nm, covering all optical telecommunication bands. Additionally, my device can be fabricated using a single-etch process.

4.2 Design and Analysis

The proposed SWG-assisted adiabatic 3 dB coupler, as shown in Fig. 4.1, is designed using a 220 nm thick silicon layer with a 2 μm thick silicon-dioxide cladding layer and a 3 μm thick buried oxide layer. As shown in Fig. 4.1(a), the coupler consists of three regions. In Region I, having length L_T, two uncoupled waveguide converters are used to convert two strip waveguides that have widths W_1 and W_2, respectively, on the left-hand side of the region to two SWG-assisted strip waveguides that also have widths W_1 and W_2, respectively, on the right-hand side of the region, and vice versa. Each waveguide converter consists of an SWG-assisted strip waveguide with constant total width but with its central strip width linearly tapered from either W_1 or W_2 to W_{core} [see Figs. 4.1(a)] where W_{core} is also the strip width for both waveguides in Region II. Thus, the effective indices of the lowest-order even and lowest-order odd modes of the two strip waveguides at the left-hand

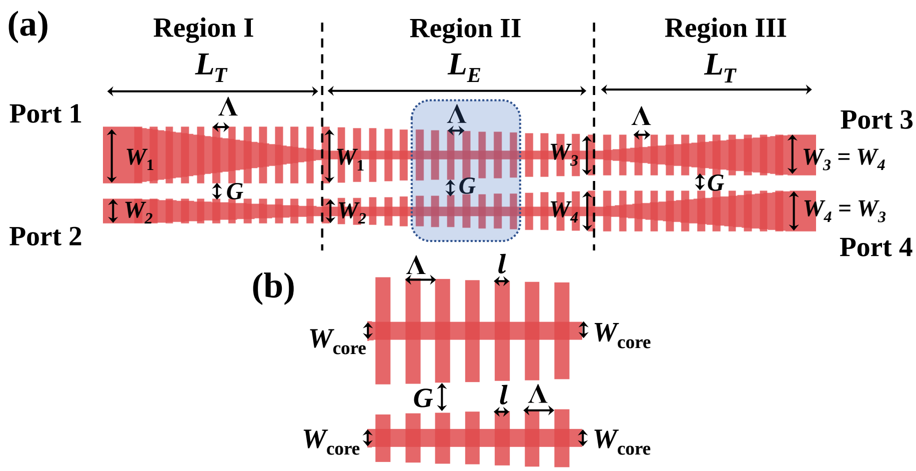

Figure 4.1: (a) Schematic (top view) of an adiabatic 3 dB coupler using SWG-assisted strip waveguides with the design parameters labeled and (b) a zoom-in of the shaded area in Region II.

side of Region I are tapered to those of the two SWG-assisted strip waveguides at the right-hand side of Region I, respectively. Region II is the mode evolution region and has a length of L_E. In Region II, the two SWG-assisted strip waveguides have the same strip widths which are constant and equal to W_{core}, but have total widths that are linearly tapered from W_1 and W_2 on the left-hand side of the region to W_3 and W_4 on the right-hand side of the region, respectively [see Fig. 4.1(b)]. In Region III, also having length L_T, two coupled waveguide converters are used to convert the two SWG-assisted strip waveguides that have widths W_3 and W_4, respectively, on the left-hand side of the region to two strip waveguides that also have widths W_3 and W_4, respectively, on the right-hand side of the region, and vice versa. In Region III, each waveguide converter consists of an SWG-assisted waveguide with constant total width but with its central strip width linearly tapered from W_{core} to either W_3 or W_4. Thus, the effective indices of the lowest-order even and lowest-order odd modes of the two SWG-assisted strip waveguide system at the left-hand side of Region III are tapered to those of the two strip waveguide system at the right-hand side of the region, respectively, and, therefore, allow the excited even and odd modes (from Region II) to propagate unaltered. In all three regions, the adiabatic coupler has the same gap distance, G, grating period, Λ, and

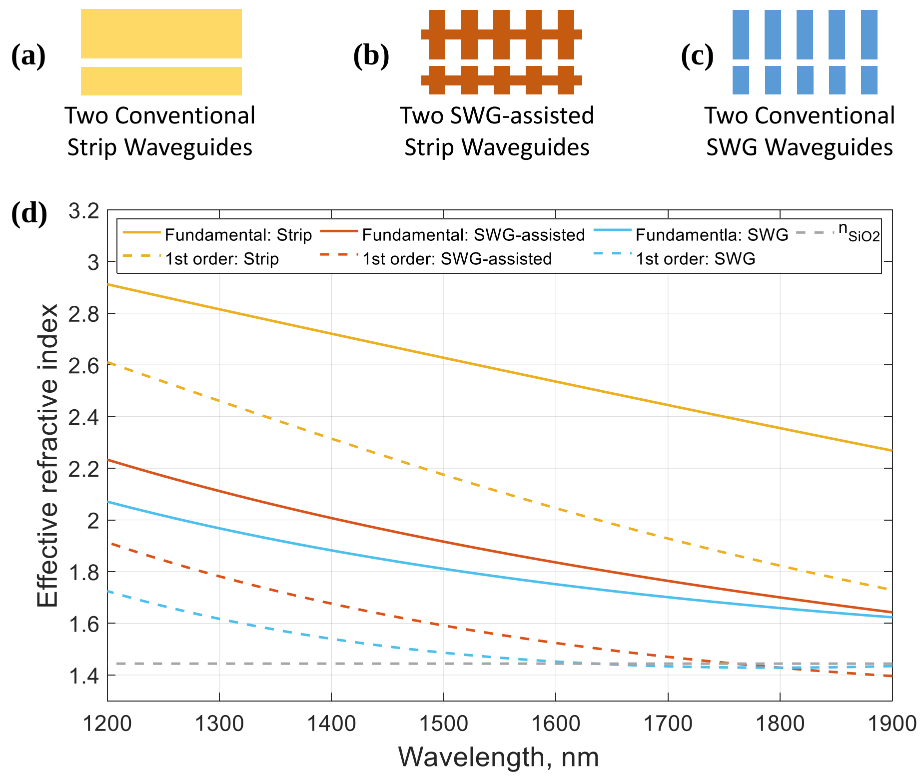

Figure 4.2: Schematic diagrams for (a) two conventional strip waveguides, (b) two SWG-assisted strip waveguides, and (c) two conventional SWG waveguides. (d) Calculated effective indices of the lowest-order even and lowest-order odd TE eigenmodes as functions of wavelength for the waveguides depicted in (a), (b), and (c).

sub-wavelength fin length, l [see Figs. 4.1(a) and 4.1(b)].

For single system excitation at Ports 1 and 2, I introduce a large asymmetry to the waveguide widths of the two waveguides where $W_1 = 610$ nm and $W_2 = 350$ nm. For 3 dB power splitting, I use $W_3 = W_4 = 480$ nm at Ports 3 and 4. In my design, $\Lambda = 200$ nm, $l = 100$ nm, $G = 100$ nm, and $W_{core} = 120$ nm. I calculated the effective index, n_{eff}, for both the lowest-order even and lowest-order odd eigenmodes of the two asymmetric SWG-assisted strip waveguides (with $W_1 = 610$ nm and $W_2 = 350$ nm) using 3d FDTD band structure calculations [76, 80] with Bloch boundary conditions applied in the mode propagation direction over the wavelength range 1200 nm to 1700 nm (for this, I used FDTD Solutions, from Lumerical Inc.). In my simulations, I used the refractive index data reported by Palik [154], which are provided in the material database in FDTD Solutions, for both Si and SiO_2. As shown in Fig. 4.2, $n_{eff} = 2.2332$ for the lowest-order even TE mode at $\lambda = 1200$ nm and, thus, I chose Λ to be less than the Bragg wavelength of 268.7 nm at 1200 nm. As a comparison, I also simulated the conventional SWG waveguide pair used in Ref. [76] and the conventional strip waveguide pair with the same waveguide geometries and gap distances that I used in my SWG-assisted strip waveguide pair [see Figs. 4.2(a) and 4.2(c)]. As expected, for both the even and odd TE eigenmodes of the two waveguide system, my SWG-assisted strip waveguides have much lower effective indices than the conventional strip waveguides but higher effective indices than the conventional SWG waveguides. In this case, as shown in Fig. 4.2(d), SWG-assisted strip waveguides extend the cut-off wavelength from 1630 nm to 1760 nm where n_{eff} for the odd TE eigenmode is equal to the refractive index of the SiO_2.

In my design, I used $L_T = 10$ μm and found that the eigenmode transmissions for the lowest-order even and odd TE modes saturated at $L_E = 15$ μm. Hence, I chose L_E to be 15 μm and, as shown in Fig. 4.3, the TE mode injected into Port 1 was coupled to the even TE mode of the two output waveguides at Ports 3 and 4, whereas, the TE mode injected into Port 2 was coupled to the odd TE mode, again at Ports 3 and 4, at $\lambda = 1550$ nm. As shown in Fig. 4.4, I obtained a worst case insertion loss and eigenmode transmission of 0.012 dB and -0.096 dB, respectively, for the even TE mode and of 0.006 dB and -0.201 dB, respectively, for the odd TE mode over the 500 nm wavelength range. Here, the eigenmode transmission is the ratio of the power coupled from the eigenmode excited at the input to the same order eigenmode at the output in dB and is obtained by performing an overlap integral of the output field profile with the eigenmode of the two waveguide system as solved by the eigenmode solver in FDTD Solutions [76]. The simulated low insertion losses and high eigenmode transmissions indicate that nearly adiabatic mode evolutions are achieved for both the even and odd TE eigenmodes in my device.

Then, to evaluate the power splitting ratio of my adiabatic coupler, I connected two asymmetric S-shape waveguides to Ports 1 and 2 to bring the two strip waveg-

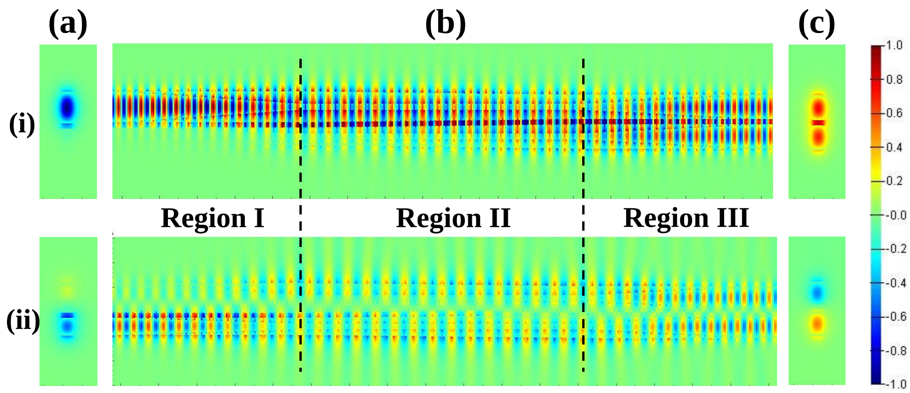

Figure 4.3: (a) Left end view, (b) top view, and (c) right end view of the simulated electric field distributions of the even (i) and odd (ii) TE eigenmodes for an SWG-assisted adiabatic 3 dB coupler when light is injected at Ports 1 and 2, respectively.

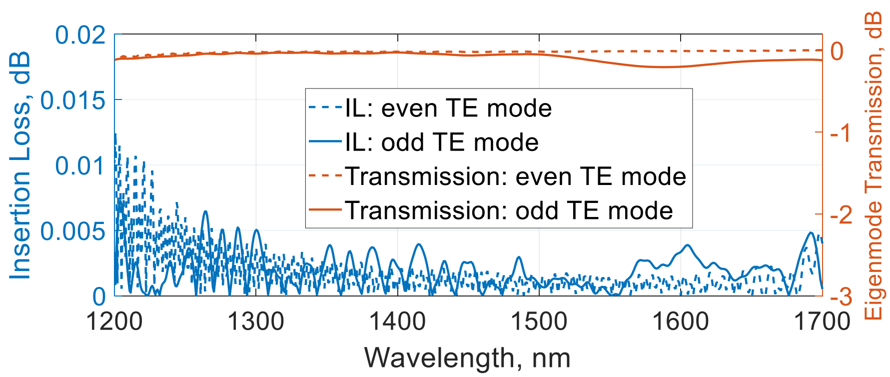

Figure 4.4: Simulated insertion losses (IL) and eigenmode transmissions vs. wavelength for the even and odd TE eigenmodes of the two waveguide system.

uides from a separation of 3 μm to 100 nm, with minimal losses. I used two S-shape waveguides with mirror symmetry, that connect to Ports 3 and 4, to separate the two strip waveguides from 100 nm to 3 μm, to avoid further coupling. The widths of the S-shape waveguides that connect to Ports 1, 2, 3, and 4 are W_1, W_2, W_3, and W_4, respectively. I simulated the entire device, including the adiabatic coupler and the S-shape waveguides, and, as shown in Fig. 4.5, obtained broadband 3 dB power splitting over the wavelength range 1200 nm to 1700 nm. In

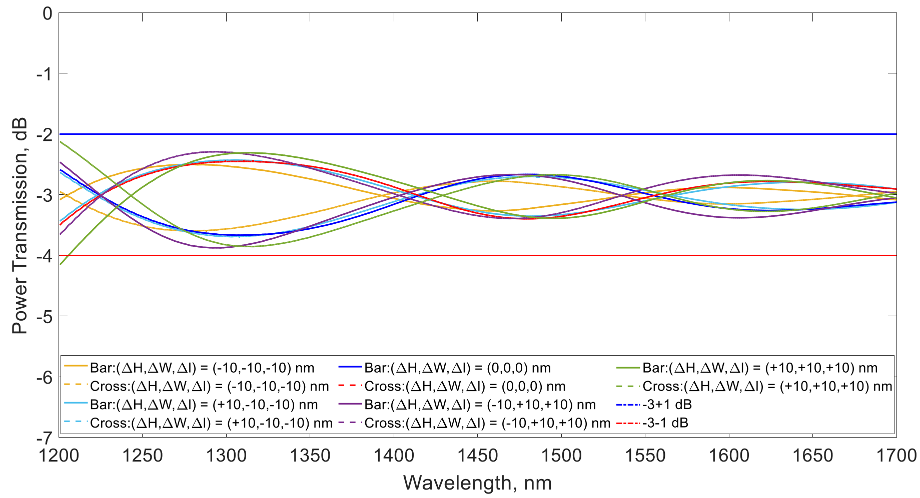

Figure 4.5: Simulated optical power splitting ratios of an SWG-assisted adiabatic 3 dB coupler considering fabrication process corners.

my broadband simulations, multifrequency source calculations (provided in FDTD Solutions) that include multiple frequencies, 21 frequencies in my case, were used to minimize mode mismatch errors.

I also explored the fabrication tolerances of my design by simulating my device for process corners, by considering variations in waveguide thickness (ΔH) and feature sizes (ΔW and Δl, where ΔW is the variation applied to both the total waveguide width and the strip width and Δl is the variation applied to the subwavelength fin length). I maintained a constant center-to-center distance for the two waveguides and a constant Λ. In my simulations, I used $\Delta H = \pm 10$ nm and $\Delta W = \Delta l = \pm 10$ nm to account for possible fabrication process variations that could occur in commercially available SOI fabrication processes [155]. As shown in Fig. 4.5, the simulated optical power splitting ratios are not highly sensitive to these variations.

4.3 Fabrication and Measurements

My SWG-assisted adiabatic 3 dB couplers were fabricated using EBL with plasma etching on an SOI platform. Fabrication was conducted at Applied Nanotools Inc. Figures 4.6(a) and 4.6(b) show scanning electron microscope (SEM) images of a

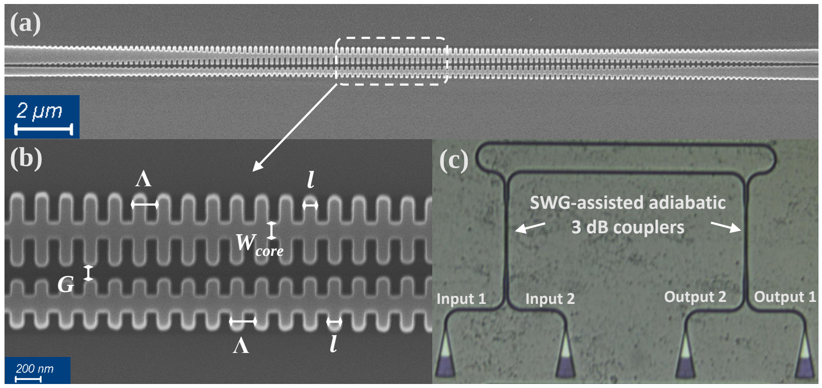

Figure 4.6: (a) SEM image of a fabricated SWG-assisted adiabatic 3 dB coupler. (b) SEM image of the center of Region II. (c) Microscope image of a fabricated, unbalanced MZI with two mirror image SWG-assisted adiabatic 3 dB couplers.

fabricated SWG-assisted adiabatic 3 dB coupler with $\Lambda = 200$ nm, $l = 100$ nm, $W_{core} = 120$ nm, and $G = 100$ nm. To demonstrate the performance of my device, as shown in Fig. 4.6(c), I integrated two of my SWG-assisted adiabatic 3 dB couplers into an unbalanced MZI [15, 76], where the output coupler was a mirror image of the input coupler, and the two 3 dB couplers were connected by two waveguides with a length difference of 160 μm. Broadband SWG TE-mode GCs [12] were used to couple light into and out of the MZI circuit. The fabricated device was measured on a custom-built test setup [50] that included a TE-polarization-maintaining fiber array (for light injection and collection), an Agilent 81600B tunable laser (as the light source), and an Agilent 81635A with the two optical power sensors (as the output detectors). I performed a wavelength sweep from 1455 nm to 1640 nm (which is the maximum wavelength range of our tunable laser) in 1 pm steps.

The MZI spectra over the 185 nm wavelength range, after calibrating out the insertion losses introduced by the GCs, show that the ERs from both output ports were >21 dB for the even TE mode [see Fig. 4.7(a)]. As shown in Fig. 4.7(b), I extracted the normalized power splitting ratios from the ERs of the measured, straight-through, MZI responses using the method described in Section 2.2 and obtained 3 dB power splitting ratios with $< \pm 0.3$ dB imbalance over the entire wavelength range. SWG-assisted adiabatic 3 dB couplers with $\Delta W = \Delta l = \pm 10$ nm were

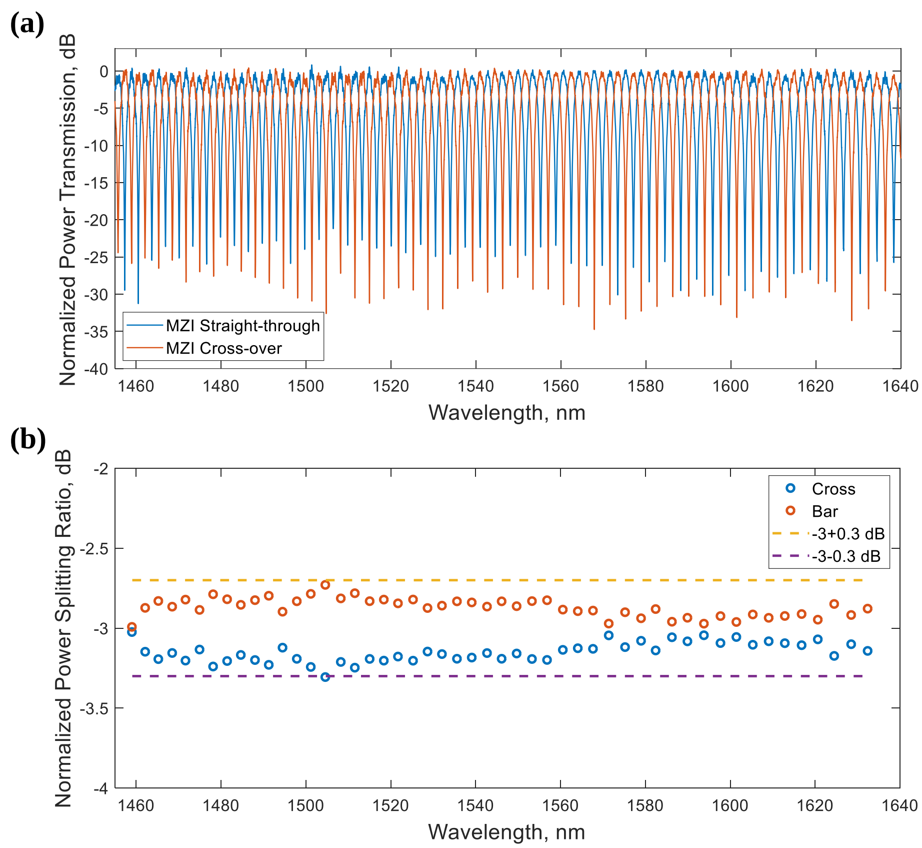

Figure 4.7: (a) Measured MZI spectral responses of the SWG-assisted adiabatic 3 dB coupler with $\Delta W = \Delta l = 0$ nm after calibration. (b) Calculated normalized power splitting ratios of the SWG-assisted adiabatic 3 dB coupler with $\leq \pm 0.3$ dB imbalance.

also fabricated while maintaining a constant center-to-center distance between the two waveguides and a constant Λ. As shown in Fig. 4.8, all of the devices (including the one with $\Delta W = \Delta l = 0$ nm) provided broadband 3 dB power splitting ratios with imbalances of $\leq \pm 0.7$ dB over the 185 nm wavelength range. This shows that, as expected, my SWG-assisted adiabatic 3 dB coupler is robust as regards fabrication variations.

To evaluate the excess loss for my coupler, I used a power calibration method [14, 50]. As shown in Fig. 4.9(a), I, again, integrated two mirror image SWG-assisted adiabatic 3 dB couplers into a balanced MZI where Port 2 of each adiabatic coupler

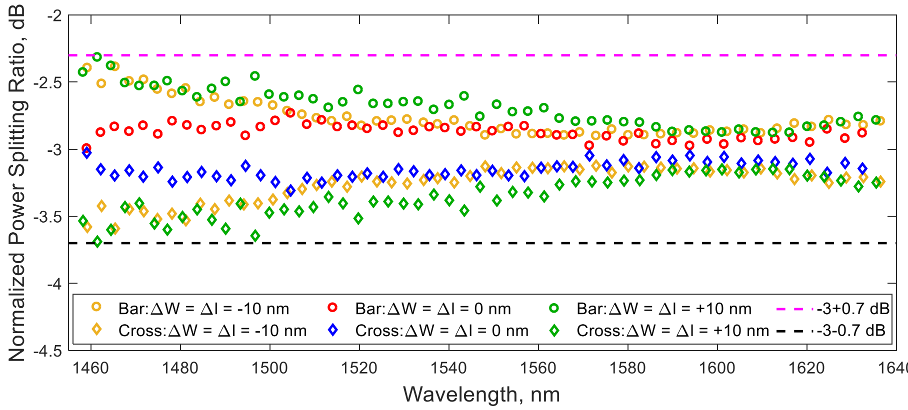

Figure 4.8: Normalized power splitting ratios extracted from experiments for three SWG-assisted adiabatic 3 dB couplers with $\Delta W = \Delta l = -10$ nm, 0 nm, and +10 nm.

was terminated using a waveguide terminator. In this case, ideally, when light is injected into Port 1 of the input adiabatic coupler, all of the optical power couples to Port 1 of the output adiabatic coupler. I cascaded multiple MZIs into chains and measured the transmission responses. I obtained the transmission spectra (including the losses introduced by the GCs) for chains of 12, 20, 40, and 80 couplers [see Fig. 4.9(b)]. Assuming that similar components have similar losses for the measured devices, as shown in Fig. 4.9(c), I used linear regressions to fit the measured MZI transmissions for various wavelengths. As shown in Fig. 4.9(d), I obtained average excess losses of < 0.11 dB for my SWG-assisted adiabatic 3 dB coupler, over the measured 185 nm wavelength range, after calibrating out the propagation losses from the interconnect waveguides between my adiabatic couplers and between the cascaded MZIs.

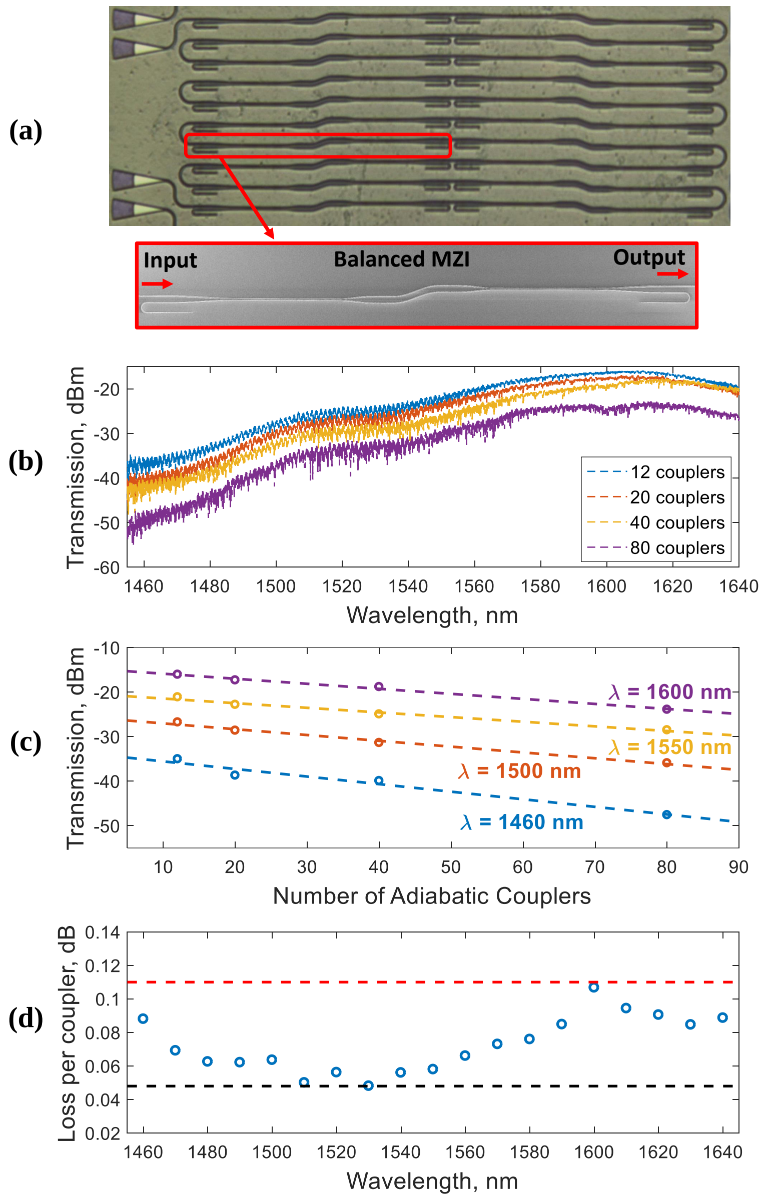

Figure 4.9: (a) Microscope image of a chain of cascaded MZIs and an inset SEM image showing a balanced MZI with two mirror image SWG-assisted 3 dB couplers. (b) Measured spectral responses of cascaded MZI chains having various numbers of couplers. (c) Linear regressions used to extract average excess losses for various wavelengths. (d) Extracted average excess losses for my SWG-assisted 3 dB coupler.

Chapter 5

Sub-wavelength Grating Contra-directional Couplers*

In this chapter, broadband, flat-top, optical add-drop filters are proposed and demonstrated using apodized, SWG CDCs on an SOI platform. In my device, two asymmetric SWG waveguides, having corrugation-apodized Bragg gratings, are used to couple light contra-directionally between the fundamental and next higher-order transverse electric modes of a two-waveguide system. I demonstrate an apodized, SWG CDC that has a flat-top, drop-port response with a 3 dB bandwidth of 32.6 nm, a sidelobe suppression ratio of 19 dB, and a low excess loss of 0.26 dB. I also demonstrate series-cascaded, apodized, SWG CDCs that have square-shaped, drop-port responses with 3 dB bandwidths $>$30 nm, sidelobe suppressions $>$50 dB, and low excess losses $<$0.85 dB.

*A version of Chapter 5 has been published: Han Yun, Mustafa Hammood, Stephen Lin, Lukas Chrostowski, and Nicolas A. F. Jaeger, "Broadband Flat-top SOI Add-drop Filters Using Apodized Sub-wavelength Grating Contradirectional Couplers," *Optics Letters*, 44, pp.4929-4932, 2019

5.1 Motivation

SOI CDCs are wavelength-selective, add-drop filters with flat-top responses, wide bandwidths, low insertion losses, and high extinction ratios (ERs) [19, 22, 26, 83–85, 103, 113, 114, 156, 157]. These devices are promising candidates for applications that require filters with flat-top responses and broad operating bandwidths such as coarse wavelength division multiplexing (CWDM), bandwidth-tunable filtering [157, 158] and dispersion engineering [82]. In a CDC, two asymmetric SOI waveguides with integrated Bragg gratings are typically used to couple light contra-directionally between the fundamental and next higher-order modes of the two-waveguide system, at selected wavelengths. Hence, when light is injected into one of the waveguides of the CDC, the selected wavelengths are dropped and reflected to the other waveguide. However, due to the high-index-contrast between the cladding (SiO_2) and waveguide (Si) layers, guided optical modes are strongly confined in conventional strip and ridge waveguides. Therefore, it is difficult to achieve very large coupling strengths between the two system modes. Thus, conventional SOI CDCs typically have bandwidths no greater than 10 nm. However, for wavelength-division-multiplexing (WDM) band splitting, filters of bandwidths $>$30 nm are needed to separate (or combine) C-band signals from (or with) other wavelength band signals which requires one to expand the bandwidths of the CDCs. To achieve this, SWGs provide a means to expand the bandwidth of a CDC. As demonstrated in Chapter 3, in comparison with conventional waveguides, SWG waveguides can be engineered so that their optical modes are less confined to the waveguides. This can be used to achieve stronger mode overlaps between the two system modes in the CDC and, thus, expand the CDC's bandwidth. SOI CDCs using one SWG waveguide and one conventional strip waveguide have been demonstrated with 3 dB bandwidths of 18.2 nm. However, these devices exhibited strong sidelobes, having sidelobe suppression ratios (SLSRs) of only $\sim$3 dB, in their pass-bands (i.e., in their drop-port responses) [83]. Some effort has been made to reduce SLSRs to below 19 dB by apodizing the gap distances between the SWG and strip waveguides [84, 156]. However, these devices had limited bandwidths and ERs of 12 nm and 14 dB, respectively [84]. A recently demonstrated SWG CDC, also using one SWG waveguide and one strip waveguide, achieved a

3 dB bandwidth of 33.4 nm [85]. However, this device had very strong sidelobes with an SLSR of ∼2 dB and required a minimum feature size of 40 nm, which is very challenging for mass production using optical lithography processes.

5.2 Design and Analysis

The SWG CDC design, as shown in Fig. 5.1(a), uses a 220 nm thick silicon layer, a 2.2 μm thick silicon dioxide upper cladding layer, and a 2 μm thick buried oxide layer. The device consists of three regions. Region I is the mode transition region and has length L_T. As shown in Fig. 5.1(b), Region I consists of two uncoupled strip-to-SWG waveguide converters that match the two strip waveguides that have widths W_1 and W_2, respectively, on the left-hand side (LHS) of the region to two SWG waveguides that also have widths W_1 and W_2, respectively, on the right-hand side (RHS) of the region. Each strip-to-SWG waveguide converter consists of a strip-assisted SWG waveguide with its total width linearly tapered from W_1 (or

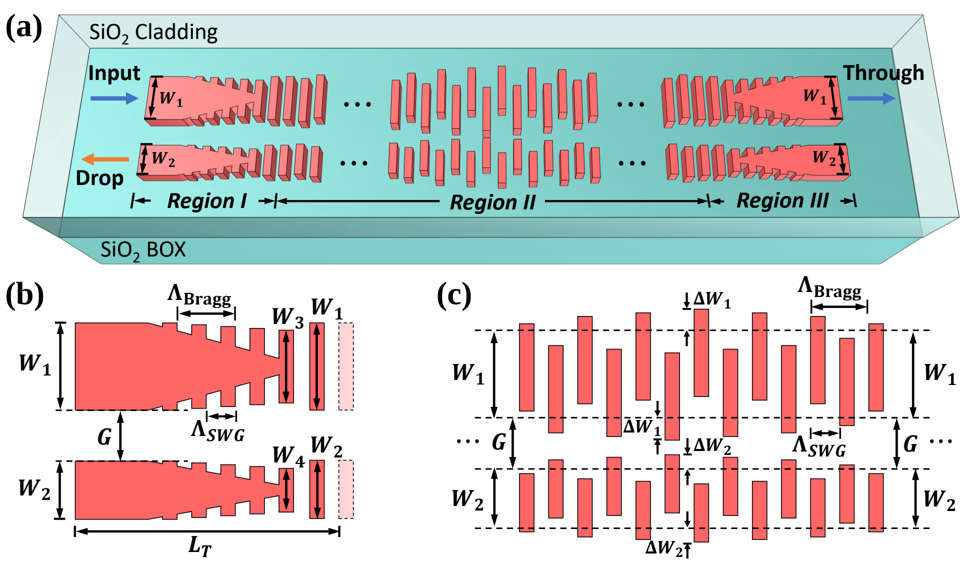

Figure 5.1: Schematic diagrams of my SWG contra-DC with design parameters labeled: (a) three-dimensional perspective view, (b) two-dimensional top view of Region I, and (c) a zoom-in of the center of Region II where ΔW_1 and ΔW_2 reach their maximum values and G reaches its minimum value.

W_2) to W_3 (or W_4) and the assisting-strip waveguide's width is linearly tapered from W_1 (or W_2) to the minimum feature size provided by the fabrication process (which is 60 nm in our case) which is finally followed by one SWG period with width W_1 (or W_2). Thus, the fundamental and next higher-order modes of the two strip waveguides on the LHS of Region I are matched to those of the two SWG waveguides on the RHS of Region I, respectively, and vice versa. Region II is the mode coupling region and consists of two SWG waveguides that have widths W_1 and W_2, respectively. For each SWG waveguide, as shown in Fig. 5.1(c), Bragg grating patterns are formed by alternately offsetting SWG sections by $+\Delta W$ and $-\Delta W$. Therefore, the SWG period, Λ_{SWG}, is one half of Λ_{Bragg} (where Λ_{Bragg} is the Bragg grating period). Also, the Bragg grating on one side of the SWG waveguide has a $\Lambda_{Bragg}/2$ mismatch with respect to that on the other side of the SWG waveguide. Hence, as originally demonstrated in conventional CDCs [22], the intra-waveguide Bragg reflection will be suppressed in each SWG waveguide. To suppress the sidelobes in my SWG CDCs response, I apodize the corrugation widths of the Bragg gratings on each SWG waveguide by applying the following Gaussian function [113] to the offsets of the SWG sections:

$$\Delta W_{1,2}(n) = \Delta W_{1,2} \cdot e^{-2[\alpha(n-0.5N)/N]^2} \tag{5.1}$$

where $\Delta W_{1,2}(n)$ is the offset of the nth SWG section in the SWG waveguide with either width W_1 or W_2, respectively, $\Delta W_{1,2}$ is the maximum offset for the SWG waveguide with either width W_1 or W_2, respectively, α is the apodization index, and N is the total number of SWG periods in each SWG waveguide. Region III is also a mode transition region and, as shown in Fig. 5.1(a), is a mirror image of Region I, here acting as SWG-to-strip waveguide converters. In all three regions, my SWG CDC has the same Λ_{SWG} with a duty cycle of 50% and a nominal gap distance, G, between the two waveguides.

I use a large waveguide-width asymmetry in my design in order to suppress the co-directional coupling between the two waveguides, where $W_1 = 560$ nm, $W_2 = 440$ nm, and $G = 200$ nm. For TE mode operation, Λ_{Bragg} is selected to meet the phase-match condition defined in Eq. 1.1 in which $\beta_a = \beta_1$ and $\beta_b = -\beta_2$ for the forward propagating, fundamental system mode and the backward propagating,

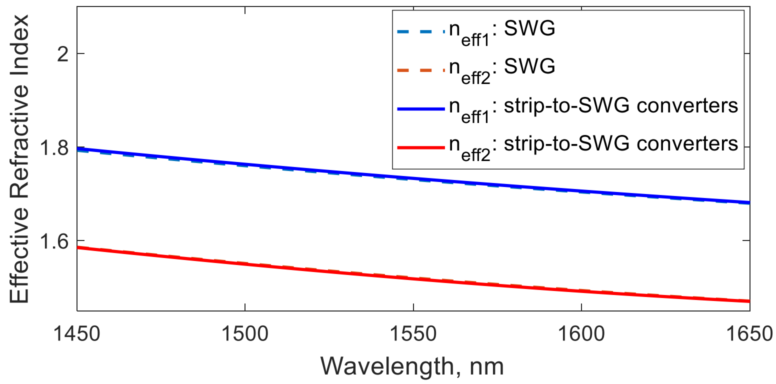

Figure 5.2: Calculated effective indices of the fundamental and the next higher-order Floquet-Bloch TE modes as functions of wavelength for the two-SWG-waveguide system in Region II (dashed lines) and the two strip-to-SWG waveguide converters with 60-nm-wide assisting-strip waveguides in Regions I and III (solid lines).

next higher order system mode, respectively. Hence, the phase-match condition for the CDC can be written to be

$$\beta_1 + \beta_2 = \frac{2\pi}{\Lambda_{Bragg}}, \tag{5.2}$$

where β_1 and β_2 are the propagation constants of the fundamental and next higher-order Floquet-Bloch TE modes (i.e., the quasi-TE_{00} and quasi-TE_{01} modes) of the two-SWG-waveguide system, respectively. In my initial design, I choose $\Lambda_{Bragg} =$ 468 nm and, thus, $\Lambda_{SWG} = 234$ nm. The effective indices of the two modes of the two-SWG-waveguide system, n_{eff1} and n_{eff2}, respectively, are obtained by calculating the equivalent refractive indices of the SWG waveguides [83, 84, 115] and by using 3D FDTD band structure calculations [76] in FDTD Solutions (from Lumerical, Inc.). To reduce the mode mismatch at the interface between Region I (or Region III) and Region II, n_{eff1} and n_{eff2} of the two strip-to-SWG waveguide converters in Region I (or the two SWG-to-strip waveguide converters in Region III) are matched to those of the two SWG waveguides in Region II, using $W_3 = 526$ nm and $W_4 = 416$ nm. As shown in Fig. 5.2, n_{eff1} and n_{eff2} are well matched over the wavelength range from 1450 nm to 1650 nm. Based on my simulation results, I use

$L_T = 23.634\ \mu$m (i.e., 101 SWG periods) to gradually taper the modes of the two strip waveguides to those of the two SWG waveguides, and vice versa, for near-ideal mode transitions. To achieve large coupling strengths and high reflectivities, I use $\Delta W_1 = 60$ nm and $\Delta W_2 = 40$ nm, which gives a minimum G of 100 nm at the center of the CDC, for a 374.4-μm-long coupling region (i.e., $N = 1600$). To suppress the sidelobes, I use $\alpha = 3.3$ in Eq. 5.1.

I use 3D FDTD band structure calculations and the coupled-mode-theory-based transfer-matrix method (CMT-TMM) [22] to simulate the spectral responses of my apodized, SWG CDC. First, I use 3D FDTD band structure calculations to obtain the bandwidth, $\Delta\lambda$, and the central wavelength, λ_o, of the SWG CDC with various sets of ΔW_1 and ΔW_2, where ΔW_1 increases from 0 nm to 60 nm and $\Delta W_2 = 2/3 \cdot \Delta W_1$. As a comparison, I also calculate $\Delta\lambda$ and λ_o for a conventional CDC, see [22] and/or [113], that consists of two strip waveguides and has the same waveguide geometries, gap distances, and corrugation depths that I used in my SWG CDC. As shown in Fig. 5.3(a), when ΔW_1 (or ΔW_2) increases to 60 nm (or 40 nm), $\Delta\lambda$ in my SWG CDC increases to 34 nm, whereas, $\Delta\lambda$ only increases to 14 nm in the conventional CDC. Also, as shown in Fig. 5.3(b), λ_o is not very sensitive to the changes in the ΔWs in my SWG CDC, whereas, in the conventional CDC, the changes in the ΔWs chirp λ_o by more than 20 nm. Such strong chirping effects on the central wavelengths have also been observed in other waveguide Bragg grating filters [159] that were made using conventional high-index-contrast SOI waveguides. Based on the above results, the contra-directional coupling coefficient, κ, can be calculated using Eq. 1.14 [104]:

$$\kappa = \frac{\pi \cdot \Delta\lambda}{\lambda_o^2}\left(\frac{n_{g1} + n_{g2}}{2}\right), \tag{5.3}$$

where n_{g1} and n_{g2} are the group indices of the fundamental and the next higher-order modes of the two-SWG-waveguide system, respectively. Next, as shown in Fig. 5.3(c), I use a second-order polynomial fit to the calculated κ values,

$$\kappa = a \cdot \Delta W_1^2 + b \cdot \Delta W_1, \tag{5.4}$$

where $a = -1.715\ \mathrm{m}^{-1} \cdot \mathrm{nm}^{-2}$ and $b = 2.034 \times 10^3\ \mathrm{m}^{-1} \cdot \mathrm{nm}^{-1}$. Then, by substituting ΔW_1 in Eq. 5.4 and using Eq. 5.1, I obtain κ as a function of the longitudinal position in the coupling region. As shown in Fig. 5.3(d), κ approaches zero at the two ends of the SWG CDC and achieves a maximum of 1.15×10^5 m^{-1} at the center. Finally, using the CMT-TMM with the calculated β_1, β_2, κ, and λ_o, I can obtain the spectral responses of my SWG CDC. As shown in Fig. 5.4, a wide,

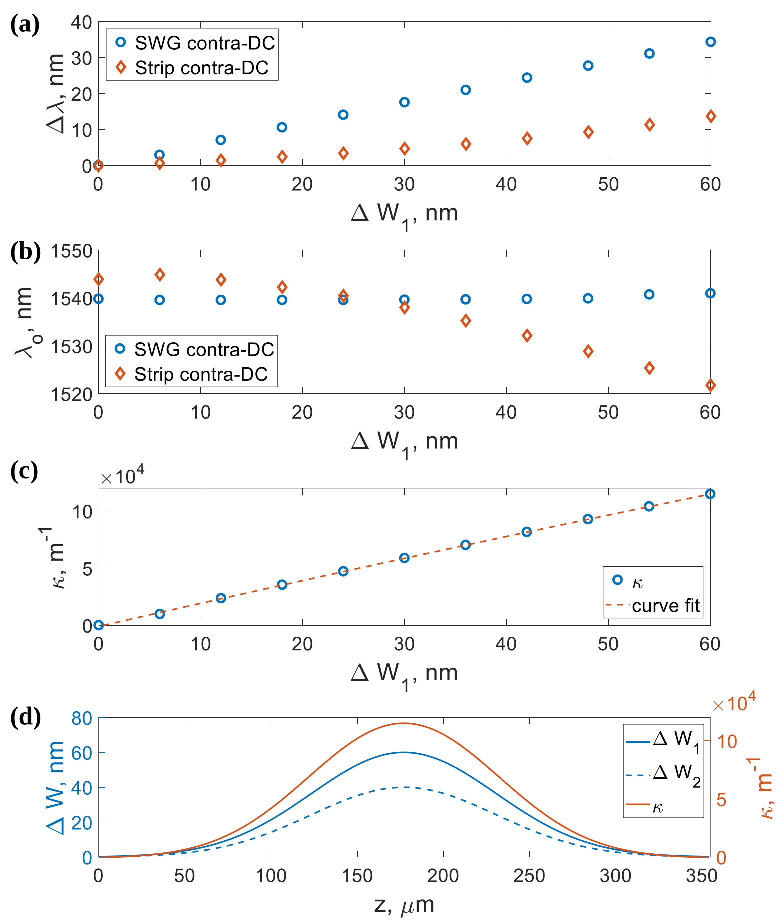

Figure 5.3: (a) Calculated $\Delta\lambda$ as a function of ΔW_1 for my SWG CDC (blue) and a conventional CDC (red), (b) calculated λ_o as a function of ΔW_1 for my SWG CDC (blue) and a conventional CDC (red), (c) calculated κ as a function of ΔW_1 for my SWG CDC with curve fit, and (d) calculated apodized ΔW_1 (solid blue), ΔW_2 (dashed blue), and distributed κ (red) as functions of the longitudinal position in my SWG CDC for $\alpha = 3.3$.

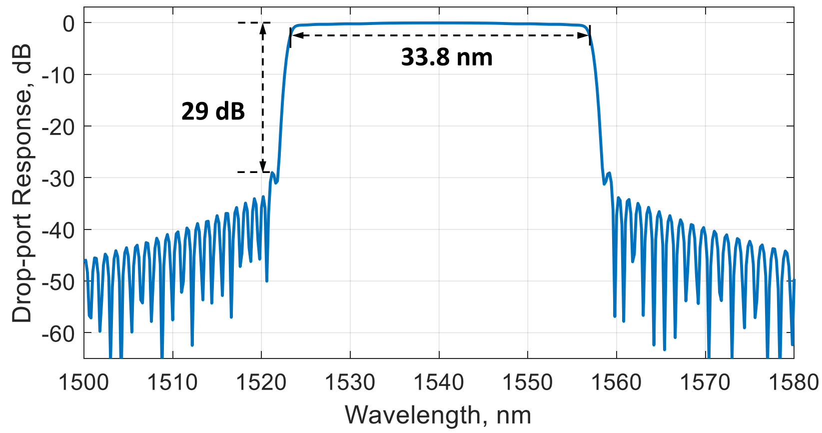

Figure 5.4: Simulated drop-port spectral response of an apodized, SWG CDC.

square-shaped, drop-port response is obtained with a 3 dB bandwidth of 33.8 nm and an SLSR of 29 dB.

5.3 Fabrication and Measurement

My apodized SWG CDC was fabricated using EBL with plasma etching. The devices were fabricated at the University of Washington WNF and Applied Nanotools, Inc. Figures 5.5(a)-(c) show SEM images of a fabricated SWG CDC. Broadband SWG TE-mode GCs [12] were used to couple light into and out of the CDC. The fabricated device was measured on a setup that included a TE polarization-maintaining fiber array (for light injection and collection), an Agilent 81600B tunable laser (as the light source), and an Agilent 81635A with two optical power sensors (i.e., as the two output detectors).

Figure 5.6 shows the measured through-port and drop-port spectral responses after calibrating out the insertion losses from the input and output GCs. The measured spectra were obtained when injecting light into the wide waveguide of my SWG CDC. As shown in Fig. 5.6, I obtained a flat-top response with a 3 dB bandwidth of 32.6 nm, an SLSR of 19 dB, and an excess loss of 0.26 dB at the drop-port. Additionally, my device had a >28 nm clear window with an ER in excess of 20 dB and a >25 nm clear window with an ER in excess of 40 dB at the through-port.

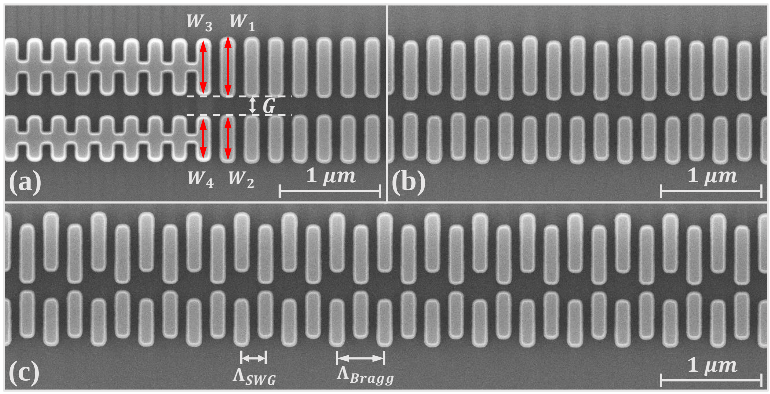

Figure 5.5: SEM images of sections of my apodized, SWG CDC: (a) strip-to-SWG waveguide converters at the interface between Regions I and II, (b) the section at which ΔW_1 and ΔW_2 are small, and (c) the center of the CDC where ΔW_1 and ΔW_2 reach their maximum values.

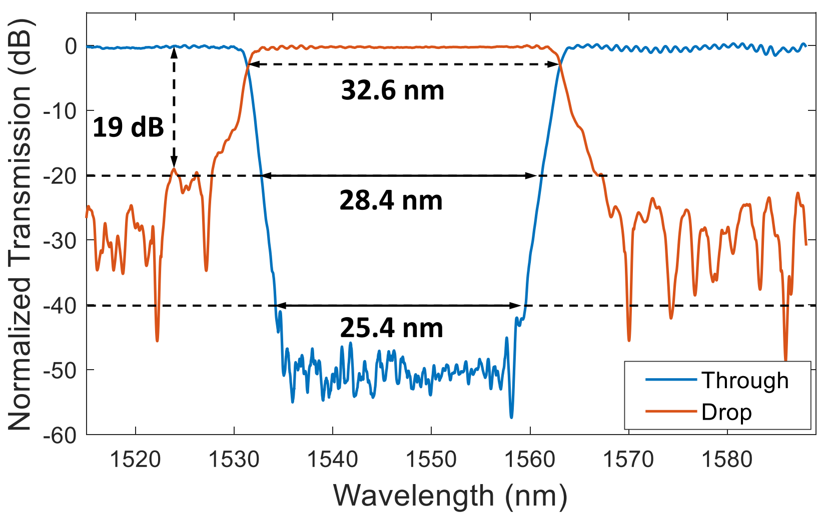

Figure 5.6: Measured spectral responses of my apodized, SWG CDC after calibration.

In comparison with the simulation results, the fabricated device has a lower SLSR. This is likely due to phase noise induced by the sidewall roughness and wafer non-uniformity [85, 102, 106]. If I were to use a minimum G of 40 nm, as was done in Ref. [85], my device should achieve a κ value of 1.43×10^5 m^{-1} which, in turn,

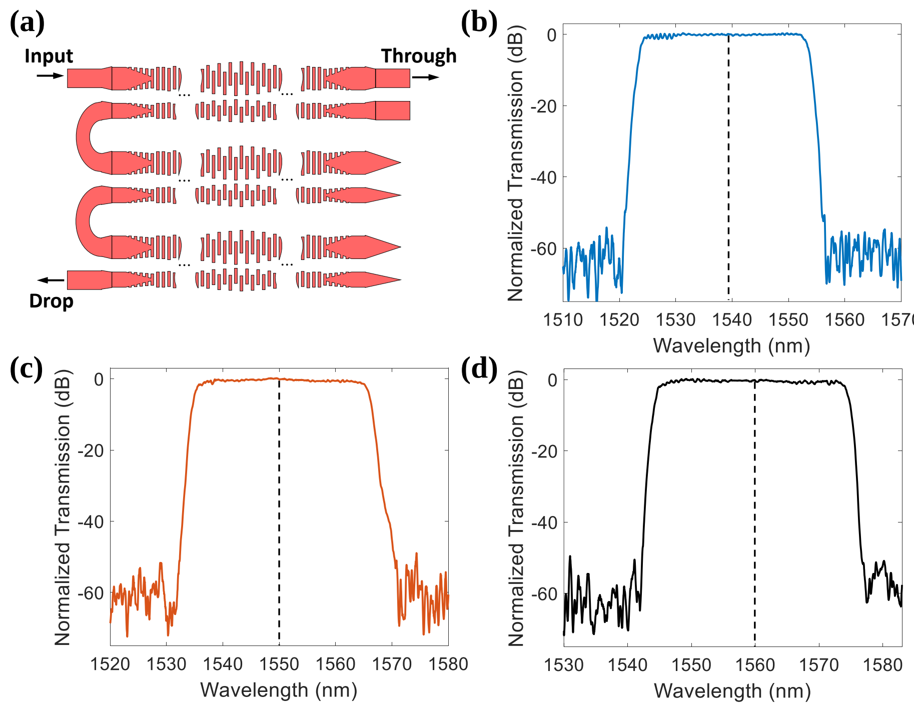

Figure 5.7: (a) The schematic of the series-cascaded, apodized, SWG CDCs. Measured, calibrated, drop-port response of serial-cascaded, apodized, SWG CDCs for (b) $\Lambda_{Bragg} = 468$ nm ($\lambda_o = 1539$ nm), (c) $\Lambda_{Bragg} = 472$ nm ($\lambda_o = 1550$ nm), and (d) $\Lambda_{Bragg} = 476$ nm ($\lambda_o = 1560$ nm).

would give a 3 dB bandwidth >40 nm (as compared to 33.4 nm as in [85]).

To further suppress the sidelobes, as shown in Fig. 5.7(a), I applied a series-cascaded configuration [113] to my apodized, SWG CDCs. In this configuration, three identical apodized, SWG CDCs were cascaded in which the drop-port of one CDC was connected to the input-port of the next CDC. To show that my device can be designed for various λ_os, I fabricated three devices for $\Lambda_{Bragg} = 468$, 472, and 476 nm, with corresponding measured λ_os of 1539, 1550, and 1560 nm, respectively. As shown in Figs. 5.7(b) - (d), I obtained square-shaped, drop-port responses with 3 dB bandwidths >30 nm, sidelobe suppressions >50 dB, and excess losses <0.85 dB for all three devices.

Chapter 6

Polarization-rotating Bragg-grating Filters

Silicon photonic waveguide Bragg grating filters offer great potential in PICs for optical communication and sensing applications due to their small footprints, low fabrication costs, and compatibility with CMOS processes [20, 82, 100, 104, 107, 160]. However, due to the large birefringence in high-index-contrast SOI waveguides, these Bragg grating filters, as well as other types of SOI filters (such as MRR, AWG, and CDC), are highly polarization sensitive and, thus, are typically designed for either TE mode or TM mode operation. To work for both the TE and TM modes, these polarization-sensitive filters require polarization control circuits to be connected at their inputs, since light is typically coupled from optical fibers to silicon PICs with arbitrary polarization states [86]. As briefly described in Section 1.2.3, PRBGs provide alternative solutions for polarization-independent wavelength filtering. In a PRBG, the input forward-traveling light (in either or both the quasi-TE and quasi-TM modes) is coupled to backward-traveling, output light in which the powers in the quasi-TE and quasi-TM modes have been exchanged. In other words, in a PRBG, the light in each input mode is reflected into the orthogonal backward-traveling, output mode (in the rest of this chapter, I will refer to the quasi-TE and quasi-TM modes simply as TE and TM modes). A single PRBG-based filter will pass, or reflect, both the TE and TM modes at the same wavelength without the need to use additional polarization beam splitters and/or polarization rotators which are required in MRR-based [88] and AWG-based [89] polarization diversity circuits. Therefore, PRBG-based filters, having theoretically zero polarization-dependent frequency shift, are promising candidates for applications that require very small polarization-dependent frequency shifts (<1 GHz) [161].

In this work, for the first time, I proposed and demonstrated SOI PRBG filters using partially-etched, asymmetric Bragg gratings on compact, single-mode strip waveguides [95, 97]. These asymmetric Bragg gratings rotate and reflect the fundamental TE and TM modes of the waveguide at selected wavelengths. The transmitted light maintains its polarization at other wavelengths. Therefore, my PRBG filters offer wavelength-selective, polarization-rotating reflection at their reflection ports and wavelength-selective, polarization-independent filtering at their through ports. Unlike the SOI PRBG filter demonstrated in Ref. [94], my devices are fabricated using standard duo-etch processes provided by commercially available silicon photonic foundries [52, 54].

In this chapter, PRBG band-rejection filter is designed and demonstrated in Section 6.1 using uniform PRBGs and achieves a 3 dB bandwidth of 2.63 nm and an ER >27 dB for both the TE mode and the TM mode. PRBG transmission filter is designed and demonstrated in Section 6.2 using phase-shifted PRBGs and achieves a 3 dB bandwidth of 0.26 nm and an ER of 19 dB for both modes.

6.1 Polarization-rotating Bragg-grating Band-rejection Filter*

6.1.1 Design and Simulation

The proposed band-rejection PRBG filter, as shown in Fig. 6.1, is designed using a single-mode silicon strip waveguide with a thick silicon-dioxide cladding layer and a 2 μm thick buried oxide layer. The waveguide width, W, and height, H, are 400 nm and 220 nm, respectively. The Bragg-grating pattern is formed by etching first-order periodic corner corrugations into the waveguide. As shown in Fig. 6.1,

*A version of Section 6.1 has been published: Han Yun, Zhitian Chen, Yun Wang, Jonas Flueckiger, Michael Caverley, Lukas Chrostowski, and Nicolas A. F. Jaeger, "Polarization-rotating, Bragg-grating filters on silicon-on-insulator strip waveguides using asymmetric periodic corner corrugations," *Optics Letters*, vol. 40, pp. 5578-5581, 2015.

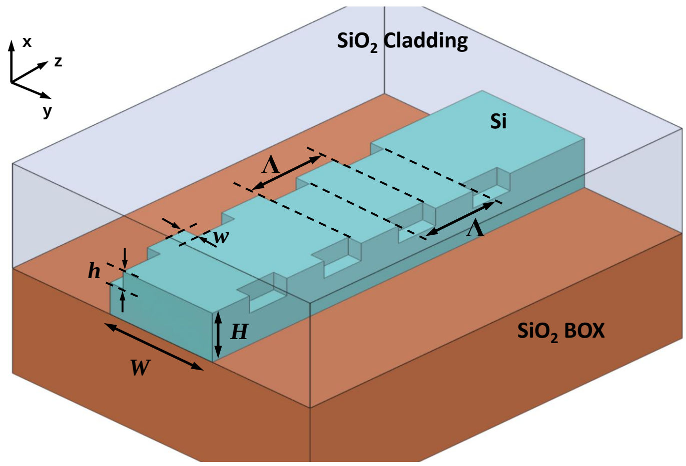

Figure 6.1: Perspective view of the polarization-rotating Bragg-grating filter on an SOI strip waveguide .

the grating pattern on one side of the waveguide is designed to have a half-period mismatch with respect to that on the other side of the waveguide [91, 93, 94].

As light propagates along the waveguide, the Bragg gratings that are partially etched into the upper right and the upper left corners break the geometric symmetry in the transverse plane. Breaking the symmetry changes the fundamental quasi-TE and quasi-TM mode distributions (see Figs. 6.2 and 6.3). In other words, the x-component and the y-component, $\vec{E}_x$ and $\vec{E}_y$, respectively, of the transverse electric field of the guided mode change. These changes are such that the total transverse electric field, $\vec{E}_t$, where $\vec{E}_t(x,y) = \vec{E}_x(x,y) + \vec{E}_y(x,y)$, is rotated. As shown in Fig. 6.3, $\vec{E}_t(x,y)$ rotates in the clockwise direction if the upper right corner is etched [see Figs. 6.3(a) and 6.3(b)] whereas it rotates in the counter-clockwise direction if the upper left corner is etched [see Figs. 6.3(a) and 6.3(c)] [162, 163]. In Figs. 6.2 and 6.3, we used a corrugation width, w, of 100 nm and a shallow-etch depth, h, of 70 nm to accentuate the rotations achieved by etching the upper right corner or and the upper left corner for illustration purposes. However, for my design, I used the values obtained for $w = 40$ nm and $h = 70$ nm, as were used for the actual device.

The PRBG couples light from the fundamental quasi-TE mode to the fundamental quasi-TM mode, and vise versa, in a counter-directional fashion, when the

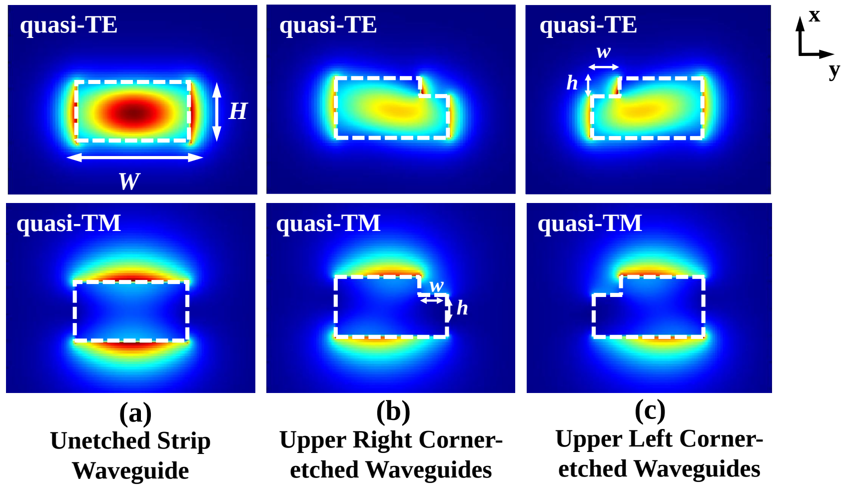

Figure 6.2: Cross-sectional geometry with the calculated intensity distributions of the fundamental quasi-TE and quasi-TM modes of the unetched strip waveguide and of the partially-etched waveguides for the cases in which the upper right corner and in which the upper left corner are etched (here $w = 100$ nm and $h = 70$ nm were used for illustration purposes.

phase-match condition

$$\beta_{\parallel}^{+} + \beta_{\perp}^{-} = \frac{2\pi}{\Lambda} \tag{6.1}$$

is met, where $\beta_{\parallel}^{+}$ is the propagation constant of the forward-propagating quasi-TE (or quasi-TM) mode input to the Bragg-grating, $\beta_{\perp}^{-}$ is the propagation constant of the backward-propagating quasi-TM (or quasi-TE) mode, and Λ is the grating period. The power coupling efficiency of the polarization-rotating reflection can be calculated using coupled-mode theory [111] and is given by:

$$\eta = \frac{|\kappa|^2 \sinh^2(sL)}{s^2 \cosh^2(sL) + (\Delta\beta/2)^2 \sinh^2(sL)} \tag{6.2}$$

where $\Delta\beta = \beta_{\parallel}^{+} + \beta_{\perp}^{-} - 2\pi/\Lambda$, $s^2 = |\kappa|^2 - (\Delta\beta/2)^2$, and L is the total length of the grating. The polarization-rotating coupling coefficient, κ, is given by

$$\kappa = \frac{\omega}{4} \iint \mathbf{E}_{\parallel}^{*}(x,y) \cdot \varepsilon(x,y) \mathbf{E}_{\perp}(x,y) dxdy \tag{6.3}$$

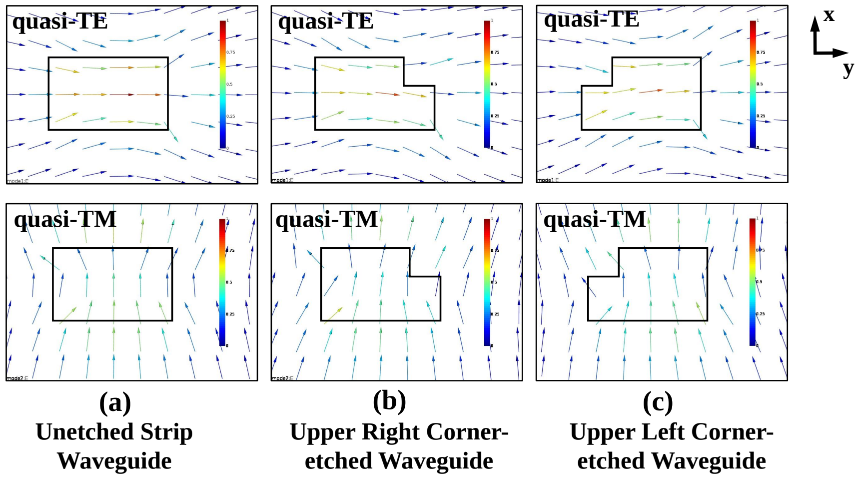

Figure 6.3: The simulated vector plots of the total transverse electric fields of the fundamental quasi-TE and quasi-TM modes of the unetched strip waveguide and of the partially-etched waveguides for the cases in which the upper right corner and in which the upper left corner are etched (here $w = 100$ nm and $h = 70$ nm were used for illustration purposes

where ω is the angular frequency, $\mathbf{E}_{\parallel}$ and $\mathbf{E}_{\perp}$ are the normalized transverse electric field distributions of the fundamental modes that have the propagation constants $\beta_{\parallel}^{+}$ and $\beta_{\perp}^{-}$, respectively, and ε is the first Fourier component of the periodic dielectric perturbation.

The fundamental quasi-TE and quasi-TM modes of the unetched strip waveguide and the partially-etched waveguide are obtained using the eigenmode solver in MODE Solutions [164] from Lumerical, Inc., with a 5 nm mesh. The calculated wavelength-dependent effective indices of the partially-etched waveguide are shown in Fig. 6.4, from which we can find the polarization-rotating wavelength

$$\lambda_{PR} = (n_{TE} + n_{TM}) \cdot \Lambda \tag{6.4}$$

due to the polarization-rotating Bragg reflection. The polarization-maintaining Bragg wavelengths, $\lambda_{TE} = 2n_{TE} \cdot \Lambda$ and $\lambda_{TM} = 2n_{TM} \cdot \Lambda$, can also be found, i.e., for TE-to-TE and TM-to-TM Bragg reflections for TE-polarized and TM-polarized light at the input, respectively. The spacings between λ_{PR} and λ_{TE} and between λ_{PR} and

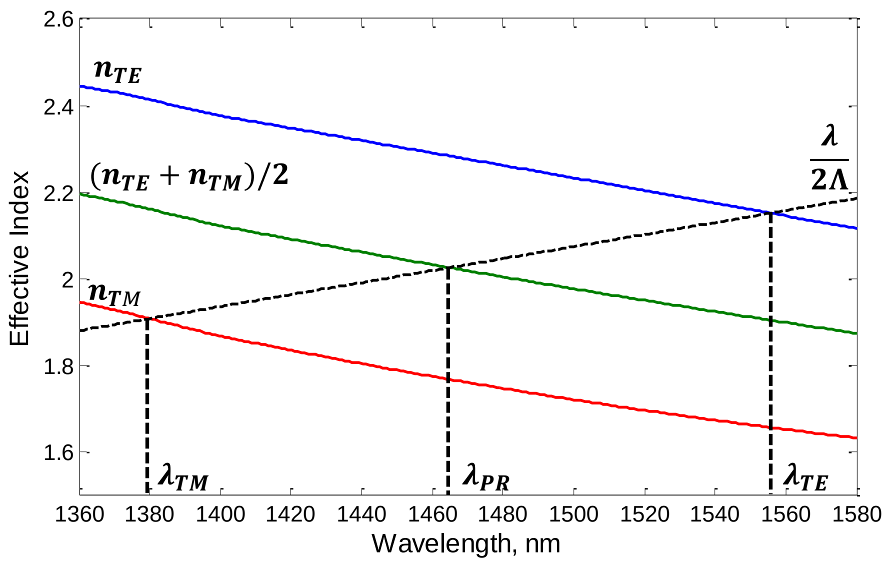

Figure 6.4: Calculated effective indices of the fundamental quasi-TE and quasi-TM modes of the partially-etched waveguide. λ_{PR} is the polarization-rotating reflection Bragg wavelength and λ_{TE} and λ_{TM} are the polarization-maintaining reflection Bragg wavelengths, respectively, for $\Lambda = 368$ nm (black dashed line).

λ_{TM} are greater than 80 nm (see Fig. 6.4). Using the transfer-matrix approach in [22], the calculated spectral responses of my device (see Figs. 6.8 and 6.7) can be obtained by solving Eqs. 6.2 and 6.3.

6.1.2 Fabrication and Measurement

Fabrication was performed at ePIXfab by IMEC in Belgium using 193 nm DUV lithography on an SOI platform. Such fabrication technology has shown the capability of reliably patterning nanophotonic features [165, 166] and has been used to fabricate Bragg-grating structures that have corrugation widths on the scale of several tens of nanometers [18–20, 22]. $h = 70$ nm was used to fabricate the waveguide corner corrugations on the strip waveguides. The fabricated device, as shown in Fig. 6.5(b), has $\Lambda = 368$ nm with a duty cycle of 50%, $w = 40$ nm, and a grating period number, N, of 800, such that the device has a total grating length of

(a)

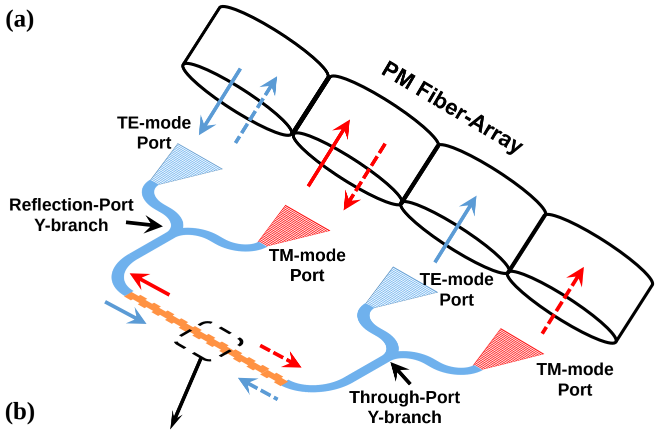

(b)

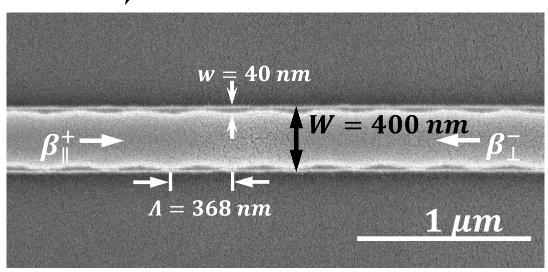

Figure 6.5: (a) Schematic for TE-to-TM (solid arrows) and TM-to-TE (dashed arrows) polarization rotation measurements. (b) SEM image showing the corrugations of a device with the propagation constants labeled and the directions of propagation indicated.

294.4 μm.

As shown in Fig. 6.5(a), TE-polarized and TM-polarized GCs [8] were used as the optical inputs/outputs to couple light into and out of my device from polarization-maintaining fibers. For the measurements, Y-branch power splitters [14] were used at both the reflection port and the through port so that the reflected and the transmitted light would be guided to the TE-mode and the TM-mode output GCs. A reference device that had its Bragg-grating waveguide section replaced by a strip waveguide was also fabricated and used to calibrate out the losses introduced by the GCs and the Y-branches. Both TE-to-TM and TM-to-TE polarization rotation measurements of my device were performed on an automated probe station [50] so that the optical power coupled into and out of the grating coupler from the fiber

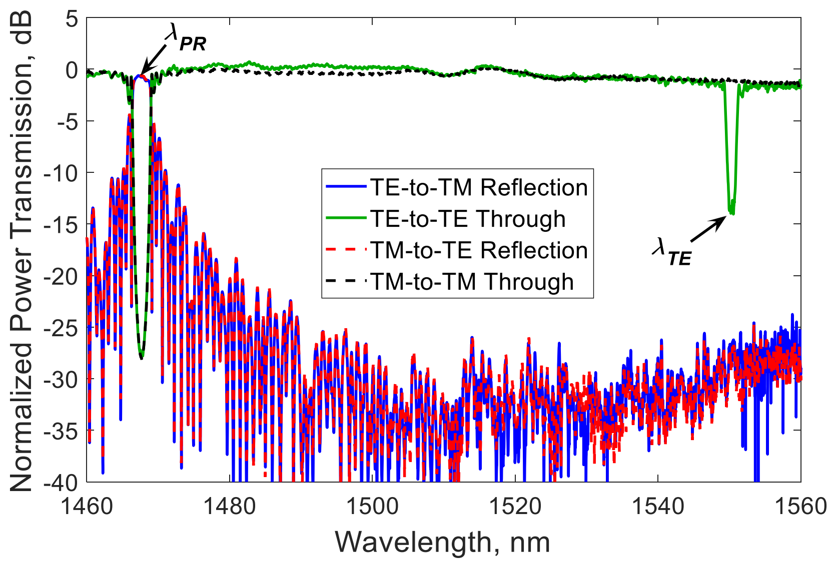

Figure 6.6: Measured reflection and transmission spectral responses over the wavelength range 1460 nm to 1560 nm for both TE-to-TM and TM-to-TE polarization rotation measurements after calibration. λ_{PR} and λ_{TE} are the measured central wavelengths for polarization-rotating Bragg reflection and polarization-maintaining Bragg reflection, respectively.

was maximized during the measurements. First, TE-polarized light was injected into the left TE-mode port, and the reflection and the transmission responses were measured at the left TM-mode port and the right TE-mode port, respectively. I then injected TM-polarized light into the left TM-mode port and measured the reflection and the transmission responses at the left TE-mode port and the right TM-mode port, respectively.

Figure 6.6 shows the measured spectra of the fabricated polarization-rotating Bragg-grating filter, after calibrating out the losses introduced by the GCs and the two Y-branch power splitters. As shown in Fig. 6.6, both TE-to-TM and TM-to-TE polarization-rotation responses were observed at the refection port centered at $\lambda = 1467.7$ nm (see the blue and dashed red lines) and the polarization-maintaining responses were observed at other wavelengths (see the green and dashed black lines). The measured phase-match wavelengths λ_{PR} and λ_{TE} are about 1467.7 nm and 1550.3 nm, respectively. The measured full-width-half-maximum (FWHM),

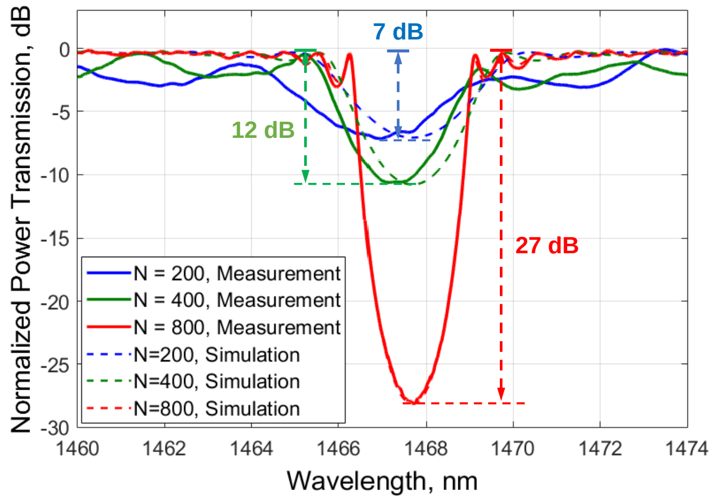

Figure 6.7: Measured (solid lines) and simulated (dashed lines) polarization-independent wavelength-selective transmission responses for devices with various grating period numbers.

i.e., the 3 dB spectral bandwidths, for both polarization-independent transmission and polarization-rotating reflection, are 2.63 nm. The measured responses show that the maximum ER obtained is in excess of 27 dB at $\lambda_{PR} = 1467.7$ nm (see Fig. 6.7) with an excess loss below 1 dB (~0.6 dB). The extinction ratio of the first sidelobes are approximately -4.5 dB.

The simulations show that the transmission extinction ratios of the devices increase from 7 dB to 27 dB when the grating period numbers increase from 200 to 800, respectively, which were also confirmed in the measurements, as shown in Fig. 6.7. In Fig. 6.7, the measured Bragg wavelengths are seen to shift slightly. This shift is due to fabrication variations.

6.1.3 Discussion

The measured phase-match wavelengths are slightly different from the predicted values which are 1465.3 nm and 1553.2 nm, respectively, shown in Fig. 6.4. These differences are likely due to the wafer non-uniformity and fabrication variations [20, 22]. The actual fabricated corrugations of the Bragg gratings are not rectangular,

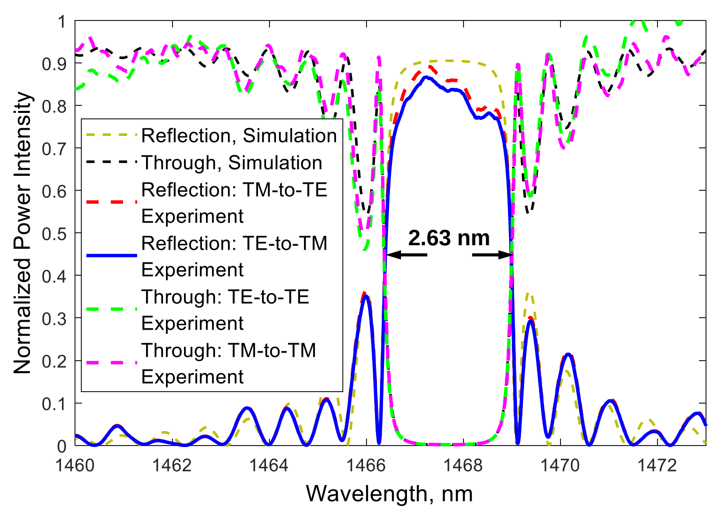

Figure 6.8: Wavelength-selective polarization-maintaining transmission and polarization-rotating reflection responses and simulation results centered at $\lambda = 1467.7$ nm with a FWHM of 2.63 nm.

due to the lithography smoothing effect [19, 20] in the fabrication processes [see the SEM image in Fig. 6.5(b)].

Also, due to the pattern-size effect in the plasma etching [19], the cross-section of the fabricated Bragg-grating is not the same as in my design. This effect results in weaker coupling (and thus a narrower bandwidth) and also changes the effective indices of the modes which can contribute to the observed wavelength shift. The design value for κ was calculated to be $1.7411 \times 10^4\ m^{-1}$, whereas the κ extracted from the measured reflection spectra was $1.3320 \times 10^4\ m^{-1}$. I have taken the above into account in my simulations by adjusting the parameters which include the effective indices and the coupling coefficients in Eqs. 6.2 and 6.3, and we were able to curve-fit the main peak as well as the sidelobes to the measured spectra [22] and obtained good agreement to the experimental results (see Fig. 6.8).

In comparison with previous work [94], our device is more compact, having a total grating length of less than 300 μm, and achieves a higher maximum polarization-extinction-ratio (PER) of greater than 27 dB. Our device also has a low excess loss of less than 1 dB and a 3 dB spectral bandwidth of 2.63 nm for both TE-to-TM and TM-to-TE polarization rotations.

6.2 Polarization-rotating Bragg-grating Transmission Filter†

SOI Bragg grating transmission filters can be achieved by using phase-shifted Bragg gratings to obtain narrow transmission peaks [167, 168] for applications including optical add-drop filters [160], modulators [33], bio-sensors [169, 170], and microwave photonic (MWP) signal processors [171, 172]. Nevertheless, these devices are again highly polarization sensitive. In recent years, many PRBG-based, band-rejection filters [94, 95, 128, 129] have been demonstrated for polarization independent operation on the SOI platform. However, very few PRBG-based transmission filters [96] have been reported (see Section 1.1.2). Here I demonstrate a thermally-tunable, PRBG-based, transmission filter using phase-shifted PRBGs with an integrated thermal heater on an SOI strip waveguide [97] for polarization-independent wavelength filtering.

6.2.1 Device Design and Simulation

The PRBG band-transmission filter was designed using a 450 nm wide, 220 nm high, single-mode SOI strip waveguide with a nominally 3 μm thick silicon dioxide cladding layer and a 2 μm thick buried oxide layer. As shown in Fig. 6.9, the PRBG pattern was formed by etching first-order periodic corner corrugations into the waveguide. The corrugations, having a corrugation width, w, and a corrugation depth, h, broke the geometrical and, therefore, the optical symmetry of the waveguide in the transverse plane and rotated the polarization of the light propagating in the waveguide [95, 128]. The grating on one side of the waveguide was shifted by a half-period relative to that on the other side of the waveguide.

The grating periodicity sets the central wavelength of the reflection band of a PRBG and polarization-rotating Bragg reflection occurs when the phase-match condition between the forward-traveling light and the polarization-rotated, backward-

†A version of Section 6.2 has been published: Han Yun, Lukas Chrostowski, and Nicolas A. F. Jaeger, "Narrow-band, polarization-independent, transmission filter in a silicon-on-insulator strip waveguide," *Optics Letters*, vol. 44, pp. 847-850, 2019.

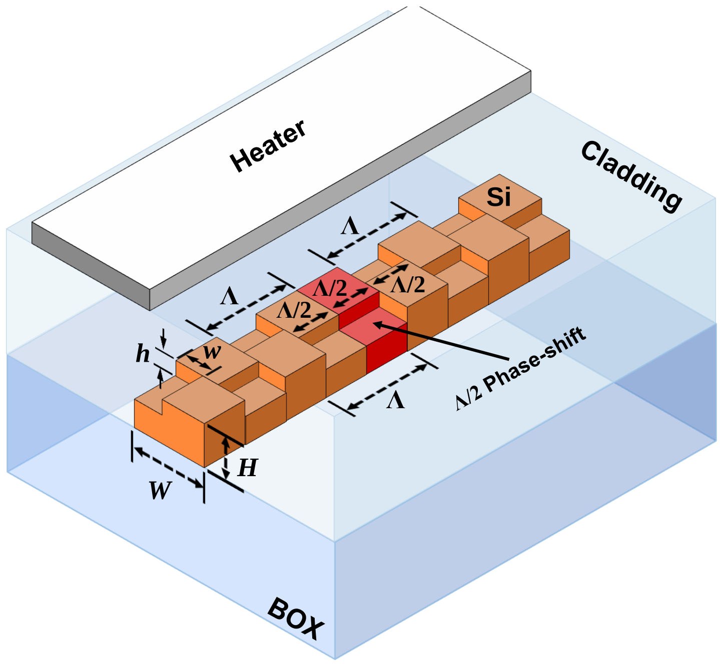

Figure 6.9: Perspective view of a schematic of the central portion of the polarization-independent transmission filter on an SOI strip waveguide with an integrated heater.

traveling light is met [95], i.e., when

$$\beta_{\parallel}^{+} + \beta_{\perp}^{-} = \frac{2\pi}{\Lambda}, \tag{6.5}$$

where $\beta_{\parallel}^{+}$ is the propagation constant of the forward-traveling quasi-TE (or quasi-TM) mode input to the grating, $\beta_{\perp}^{-}$ is the propagation constant of the backward-traveling quasi-TM (or quasi-TE) mode, and Λ is the grating period. In this work, as shown in Fig. 6.9, a $\Lambda/2$ phase-shift is introduced between two PRBGs by extending one $\Lambda/2$ section of one of the PRBGs to have a length of Λ. For both the TE and TM modes, this phase-shift and the PRBGs on each side formed a Fabry-Pérot resonant cavity and resulted in a single resonance peak at the center of the stop-band at the through-port and a corresponding notch at the center of the pass-band at the reflection-port. This peak, being polarization independent, was located around the central wavelength of the polarization-rotating Bragg reflection and, thus, was given by

$$\lambda_p = (n_{eff}^{TE} + n_{eff}^{TM}) \cdot \Lambda, \tag{6.6}$$

where n_{eff}^{TE} and n_{eff}^{TM} were the effective indices of the fundamental quasi-TE and quasi-TM modes in the corrugated waveguide, respectively. The transmission and reflection responses of the phase-shifted PRBGs can be calculated using [33, 111]

$$\begin{bmatrix} E_{\parallel}^{+}(0) \\ E_{\perp}^{-}(0) \end{bmatrix} = CPC \begin{bmatrix} E_{\parallel}^{+}(L) \\ E_{\perp}^{-}(L) \end{bmatrix}, \tag{6.7}$$

where $E_{\parallel}^{+}(0)$ and $E_{\perp}^{-}(0)$ are the field amplitudes of the propagating mode of the forward-traveling light and the polarization-rotated, backward-traveling light at the input of the device, respectively. $E_{\parallel}^{+}(L)$ and $E_{\perp}^{-}(L)$ are the field amplitudes of the propagating mode of the forward-traveling light and the polarization-rotated, backward-traveling light at the output of the device, respectively. L is the total length of the phase-shifted PRBG. C is the transfer matrix for the PRBG on either side of the phase-shift and is given by

$$C = \begin{bmatrix} \cosh(sl) + j\frac{\Delta\beta - j\alpha}{2s}\sinh(sl) & j\frac{\kappa}{s}\sinh(sl) \\ -j\frac{\kappa}{s}\sinh(sl) & \cosh(sl) - j\frac{\Delta\beta - j\alpha}{2s}\sinh(sl) \end{bmatrix}. \tag{6.8}$$

where $s = \sqrt{|\kappa|^2 - [(\Delta\beta - j\alpha)/2]^2)}$, $\Delta\beta = \beta_{\parallel}^{+} + \beta_{\perp}^{-} - 2\pi/\Lambda$, κ is the polarization-rotating coupling coefficient of the PRBG, α is the propagation loss in the PRBG, and l is the length of the PRBG [i.e., $l = (L - \Lambda/2)/2$]. P is the transfer matrix for the phase-shift and is given by

$$P = \begin{bmatrix} e^{j(\beta_{\parallel}^{+} - j\alpha/2)\Lambda/2} & 0 \\ 0 & e^{-j(\beta_{\perp}^{-} - j\alpha/2)\Lambda/2} \end{bmatrix}. \tag{6.9}$$

In my design, I chose $\Lambda = 413$ nm with a duty cycle of 50%, $w = 80$ nm, and $h = 70$ nm for a 400 period long PRBG on either side of the phase-shift, which had a length of 206.5 nm (i.e., $\Lambda/2 = 206.5$ nm). I also integrated a 360 μm long, 4.5 μm wide heater that covered the entire device for wavelength tuning. The heater was placed in the silicon dioxide cladding ~ 2 μm above the PRBG waveguide.

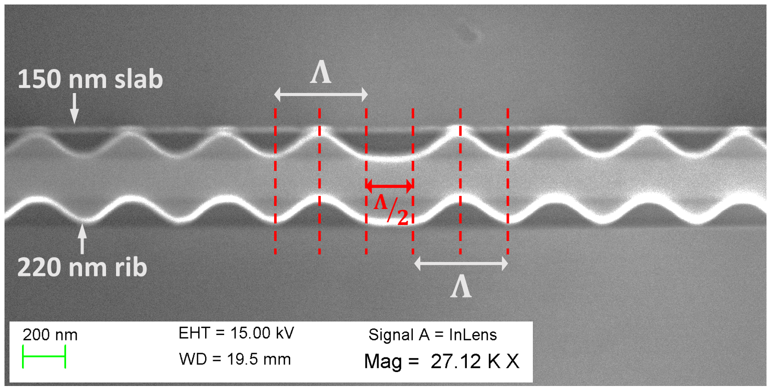

Figure 6.10: SEM image of the central portion of a fabricated, polarization-independent, transmission filter on an SOI strip waveguide.

6.2.2 Fabrication and Characterization

The device was fabricated using 193 nm DUV lithography on an SOI platform by IME in Singapore. A duo-etching process, including a shallow-etch depth of 70 nm and a deep-etch depth of 220 nm, was used to fabricate the PRBGs in a 450 nm wide, 220 nm high strip waveguide. Figure 6.10 shows the SEM image of a fabricated PRBG with a $\Lambda/2$ phase-shift in the center of the grating. A thin layer of titanium nitride was used as the heater. Aluminum alloy DC probe pads and routing wires were used to provide current to the heater.

As shown in Fig. 6.11, TE-mode and TM-mode, shallow-etched GCs [8], having the same fiber coupling angle, were used as the optical inputs/outputs to couple light into and out of my device. Y-junction power splitters [14] were used at both the reflection port and the through port so that the reflected and the transmitted light would be guided to the TE-mode and the TM-mode output GCs. The Y-junction has low excess losses of $\sim$0.28 dB for TE mode and $\sim$0.43 dB for TM mode, which were obtained from independent cutback measurements. I also fabricated a reference device that had its PRBG waveguide section replaced by a strip waveguide to calibrate out the losses introduced by the Y-junctions and the GCs. The fabricated device was measured on a test setup that included a polarization maintaining fiber array (for light injection and collection), an Agilent 81600B tunable laser (as the light source), and an Agilent 81635A with the two optical power sensors (as

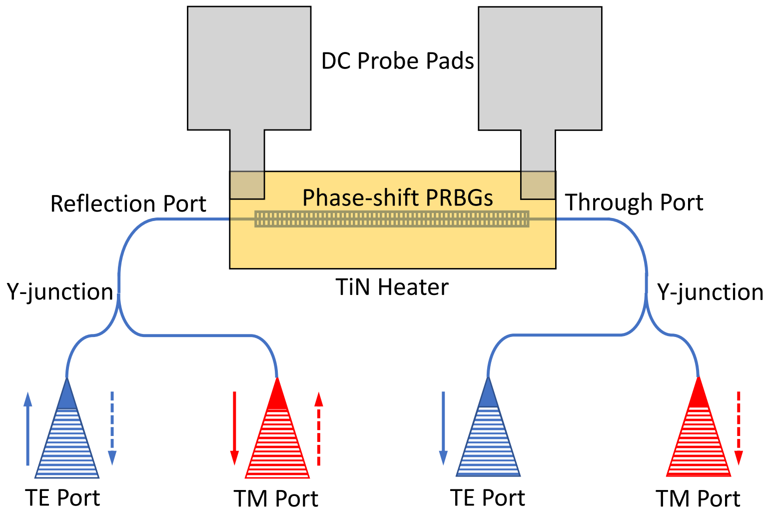

Figure 6.11: Schematic for the TE-mode (solid lines) and TM-mode (dashed lines) measurements with integrated heater (yellow region) for thermal tuning.

the output detectors). DC probes were used to apply a voltage to the heater and a Keithley 2602 was used as both the voltage source and the power meter.

As shown in Fig. 6.11, both TE-mode and TM-mode measurements were performed on fabricated device. First, TE-polarized light was injected into the left TE-mode port, and the reflection and the transmission responses were measured at the left TM-mode and the right TE-mode ports, respectively. I then injected TM-polarized light into the left TM-mode port and measured the reflection and the transmission responses at the left TE-mode and the right TM-mode ports, respectively. Figure 6.12 shows the through-port and reflection-port spectral responses obtained when the TE-mode light was injected and when the TM-mode light was injected. As shown in Fig. 6.12, after calibrating out the losses from the GCs and the Y-junctions, for both the TE- and TM-mode inputs, polarization-independent transmission peaks were obtained at $\lambda = 1556.36$ nm with 3 dB bandwidths of 0.26 nm, giving quality factors of $\sim$6000. The corresponding notches in the reflection responses are also shown in Fig. 6.12 and extinction ratios of 19 dB were obtained at 1556.36 nm for both the TE and TM modes.

The transmission peaks at the through-port had imbalanced out-of-band rejec-

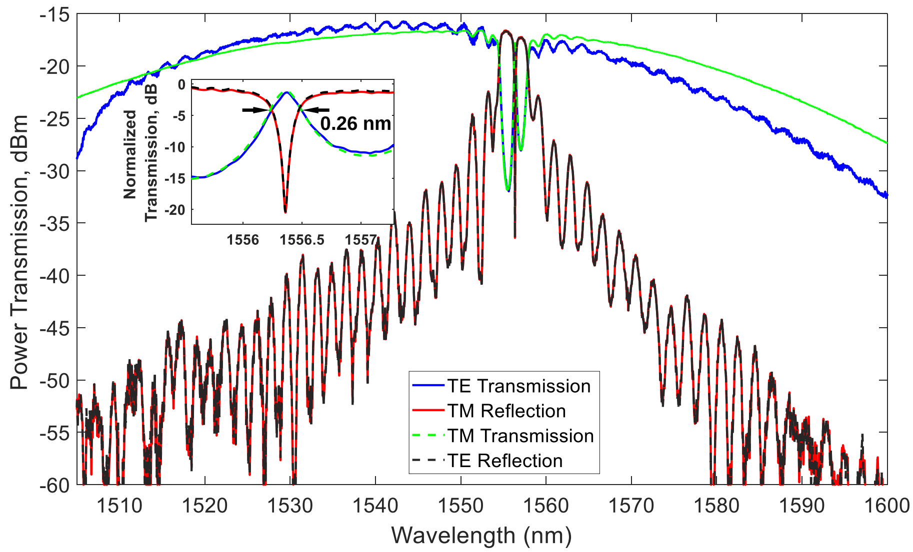

Figure 6.12: Measured spectral responses of a fabricated device for TE-mode injection (solid line) and TM-mode injection (dashed line). The inset shows the resonant transmission peak at 1556.36 nm with a 3 dB bandwidth of 0.26 nm (after calibration) for both the TE and TM modes.

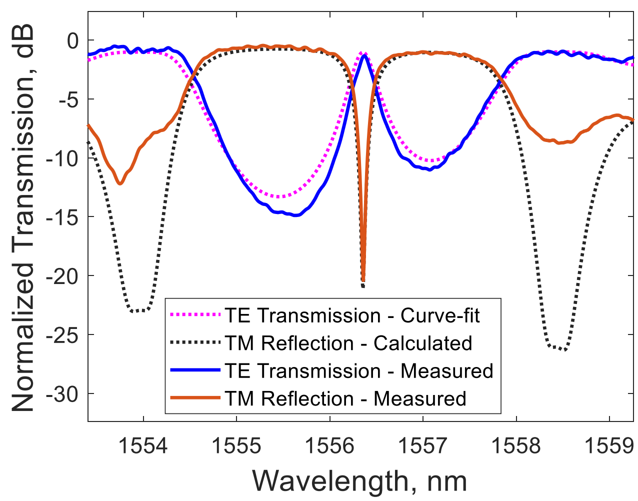

Figure 6.13: Measured calibrated through-port and reflection-port spectral responses for the TE-mode measurements. Also shown are the curve-fit through-port and calculated reflection-port spectral responses.

tion ratios which were 15 dB on the left side and 10 dB on the right side. This was likely due to fabrication imperfections resulting in the optical length of the central, Λ long section (the one with the $\Lambda/2$ phase-shift) not being exactly the same as in other Λ long sections in the PRBGs (see Fig. 6.10), which means that the fabricated phase-shift section did not give exactly a π phase shift at the designed center wavelength. I have taken the above into account in my calculations and used Eqs. 6.7, 6.8, and 6.9 to curve fit the measured TE mode transmission spectral responses. I obtained $\kappa = 7800\ \mathrm{m}^{-1}$ and an average $\alpha = 14.65$ dB/cm of the TE and TM modes in the PRBGs for the fabricated device (the propagation losses in the PRBGs are higher than those in regular strip waveguides, which are $\sim$2.5 dB/cm for TE mode and $\sim$1 dB/cm for TM mode [173]). I then used the fitted κ and α values to calculate the corresponding TM mode reflection spectral responses. As shown in Fig. 6.13, the curve-fit TE mode transmission responses and the calculated TM mode reflection responses were in good agreement with the measured calibrated spectral responses. Also, the measured calibrated through-port spectral responses showed low excess losses of less than 0.5 dB, for both modes, in my device.

I measured the group delays of my device at the through- and reflection-ports for both the TE and TM modes using an Optical Vector Analyzer$^{\mathrm{TM}}$ STe from Luna Innovations Inc. The measured group delays, that included the delays from the routing waveguides (connecting the GCs and the PRBG filter), the GCs, and the input/output fibers, are shown in Fig. 6.14. For both the TE and TM modes, a spike of 8 ps and a notch of 86 ps were observed at the same central wavelength in the through-port and reflection-port responses, respectively.

I also performed thermal tuning measurements on the polarization-independent transmission filter for both the TE and TM modes. The integrated heater had a measured resistance of 775 Ω. I measured the through-port spectral responses of the filter while varying the applied bias voltage. The measurement results are shown in Fig. 6.15. As shown in Figs. 6.15(a) and (c), the transmission peak shifted to longer wavelengths for both the TE and TM modes. I used linear regressions to fit the measured wavelength shifts and obtained 0.028 nm/mW tuning efficiency for both the TE and TM modes, as shown in Figs. 6.15(b) and (d), respectively.

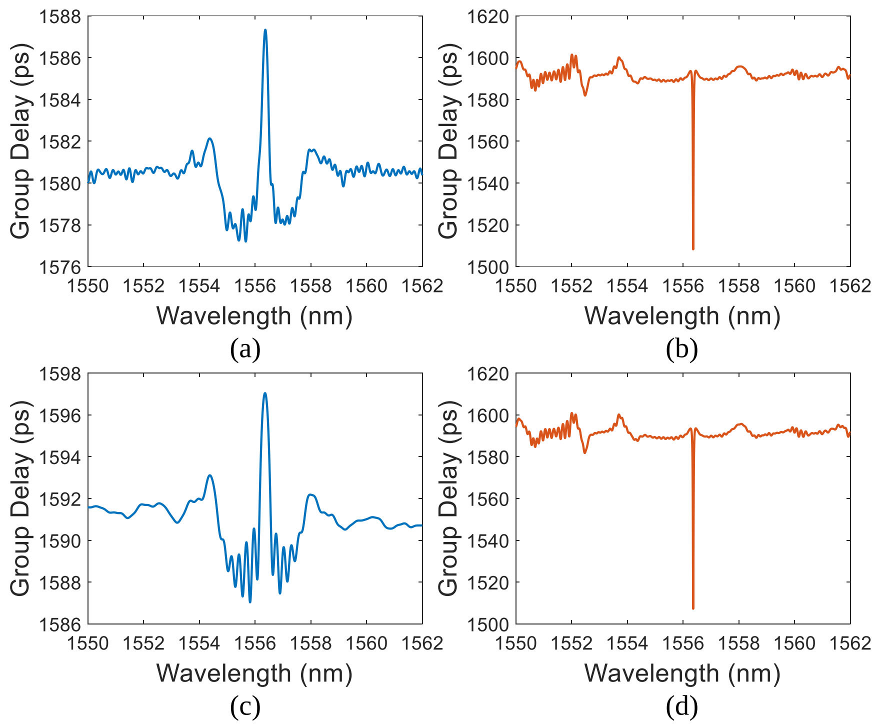

Figure 6.14: Measured group delays for (a) TE mode transmission, (b) TE-to-TM mode reflection, (c) TM mode transmission, and (d) TM-to-TE mode reflection.

6.2.3 Discussion

The center wavelength of my phase-shifted PRBG filter can be tuned by adjusting the size of the phase-shift section. The bandwidth of the transmission peak is affected by the propagation losses and the reflectivities of the PRBGs on either side of the phase-shift section. The width of the stopband on either side of the transmission peak can be tuned by varying the corrugation widths.

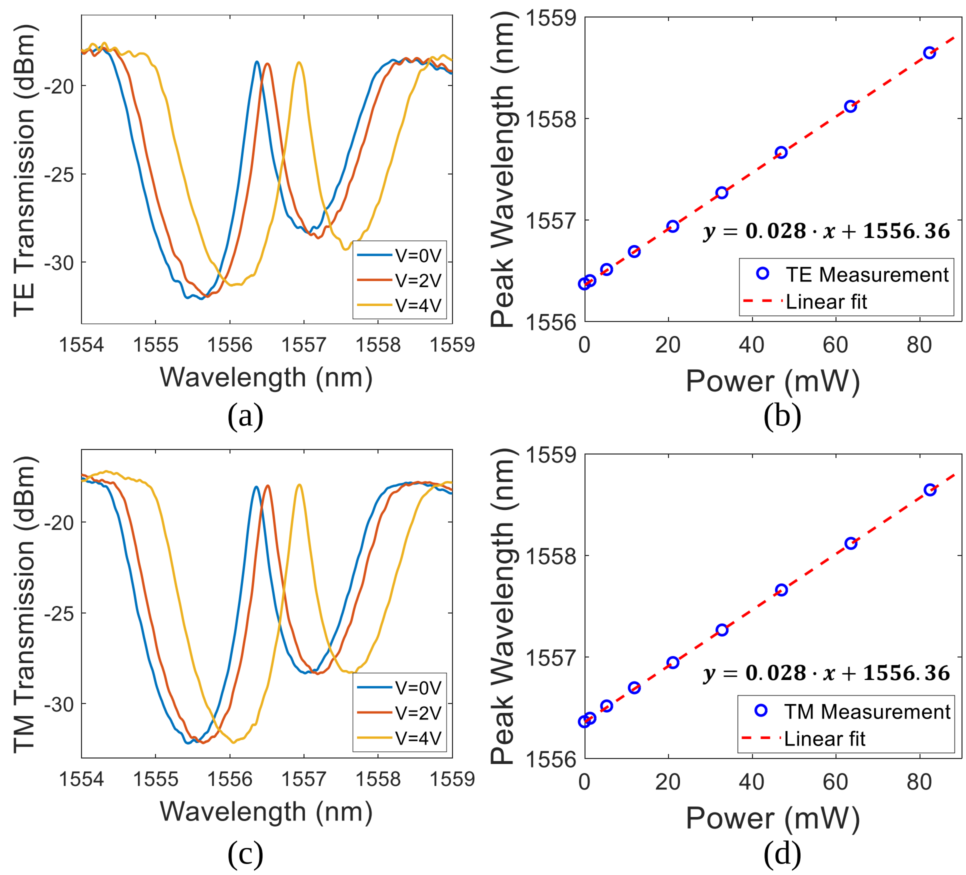

Figure 6.15: (a) Superimposed TE-mode transmission spectra for various bias voltages, (b) TE-mode peak wavelength versus the power applied to the heater, (c) superimposed TM-mode transmission spectra for various bias voltages, and (d) TM-mode peak wavelength versus the power applied to the heater.

Chapter 7

Summary, Conclusions, and Suggestions for Future Work

7.1 Summary

In this thesis, a comprehensive study of adiabatic 3 dB couplers, contra-directional couplers (CDCs), and polarization-rotating Bragg gratings (PRBGs) is presented. Each type of device has been theoretically investigated and experimentally demonstrated on the SOI platform.

The mode evolution process of guided optical modes in two waveguide systems has been studied for various types of waveguide including conventional ridge and strip waveguides, SWG waveguides, and SWG-assisted strip waveguides. In the mode evolution process, the fundamental and next higher order modes of two asymmetric waveguides evolve into those of two symmetric waveguides. This process has been studied using 3D FDTD simulations and has been applied to the designs of adiabatic 3 dB couplers for broadband operation. First, adiabatic 3 dB couplers utilizing conventional ridge and strip waveguides are demonstrated for 100-μm-long mode-evolution regions and 100 nm operating bandwidths with splitting imbalances $<$0.5 dB. Next, the propagation and dispersion properties of light in SWG waveguides are explored using 3D FDTD band structure calculations and used to design SWG adiabatic couplers featuring compact footprints, broad operating bandwidths, low splitting imbalances, low insertion losses, and high tolerances to fabrication variations. An SWG adiabatic 3 dB coupler has been fabricated with a 20-μm-long, mode-evolution region and has achieved a 130 nm bandwidth, and a splitting imbalance <0.4 dB. Finally, SWG-assisted strip waveguides have been studied and utilized for a compact, ultra-broadband, adiabatic 3 dB coupler that has a 15-μm-long, mode-evolution region, a 185 nm bandwidth, a splitting imbalance <0.3 dB, low insertion losses <0.11 dB, and a high tolerance to fabrication variations.

The methodology of using 3D FDTD band structure calculations to model SWG waveguides has also been applied to the designs of SWG CDCs as broadband add-drop filters. Strong mode couplings between the fundamental and next higher order modes of the two asymmetric waveguide system have been obtained by using two SWG waveguides with integrated Bragg gratings. High sidelobe suppressions have also been achieved by apodizing corrugation depths of the Bragg gratings along the device. An apodized, SWG CDC has been demonstrated giving a flat-top, drop-port response with a 3 dB bandwidth of 32.6 nm, an SLSR of 19 dB, and a low excess loss of 0.26 dB. Broadband, square-shaped, add-drop filters using series-cascaded SWG CDCs have also been demonstrated with 3 dB bandwidths >30 nm, sidelobe suppressions >50 dB, and low excess losses <0.85 dB.

Furthermore, PRBGs with asymmetric, periodic, corner corrugations on single-mode strip waveguides are studied. The operating principles of wavelength-selective polarization-rotation are presented and applied to achieve polarization-independent wavelength filtering. Uniform PRBGs as band-rejection filters and phase-shifted PRBGs as band-pass filters have been fabricated and tested. A PRBG band-rejection filter with 3 dB bandwidths of 2.63 nm, ERs >27 dB, and low insertion losses <1 dB has been demonstrated for both the TE and TM modes. A PRBG band-pass filter has also been demonstrated with 3 dB bandwidths of 0.26 nm and ERs of 19 dB, again, for both mode types.

7.2 Conclusions

In conclusion, I have demonstrated adiabatic 3 dB couplers for low-loss, broadband power splittings on the SOI platform. When using conventional ridge or strip waveguides, my adiabatic 3 dB couplers achieved broad operating bandwidths with low insertion losses and low splitting imbalances, but suffered from long mode evolution regions. Due the fact that SWG waveguides can be engineered to have weakly confined optical modes with low dispersion, SWG adiabatic couplers with compact footprints and wider bandwidths can be obtained; however, their operating bandwidths cut-off at wavelengths below the L-band (1630 nm in my case). Nevertheless, by including a central strip, SWG-assisted strip waveguides that support guided optical modes over all communication bands can be obtained. SWG-assisted adiabatic 3 dB couplers also have the most compact footprints, the widest operating bandwidths, and the lowest insertion losses while maintaining low splitting imbalances and high tolerances to fabrication variations. Here, I have copied Table. 1.1 (first presented in Chapter 1) since it compares the adiabatic 3 dB couplers developed in this work with state-of-the-art, mode-evolution-based, SOI power splitters demonstrated by other research groups. Functioning as 2×2 optical power splitters, my SWG-assisted adiabatic 3 dB couplers should be able to replace my conventional adiabatic 3 dB couplers which have been used for numerous optical communication applications such as optical gyroscopes [150], MZI modulators [151], Michelson interferometric modulators [65, 152], and optical switches [63, 64].

Using SWG waveguides and apodized Bragg gratings, SWG CDCs can be used to provide broadband, flat-top responses with high extinction ratios (ERs) and high sidelobe supression ratios (SLSRs). Broadband, square-shaped, add-drop filters can be obtained by using series-cascaded, apodized, SWG CDCs and can achieve ultra-high SLSRs. These devices can be used for optical communication applications including WDM band-splitters, WDM filters, and bandwidth-tunable filters.

Additionally, I have also shown that polarization-independent filters can be obtained using PRBGs. While rotating and reflecting light at same wavelengths for both the TE and TM modes, these devices can provide polarization-independent, polarization-rotating at their drop-ports and polarization-independent, polarization-maintaining at their through ports with same performance for both the TE and TM modes, and that my PRBG-based filters are promising candidates for applications that require polarization-independent wavelength filtering.

Ref.	Year	Polarization	BW (nm)	Splitting Ratio (dB)	IL (dB)	L_E (μm)	Waveguide
[73]	2006	TE&TM	300	3±0.7	∼0.5	250	Rib
[74]	2010	TE	90	3±1.1	NA	200	Rib
[68]	2013	TE	100	3±0.2	0.31	300	Rib
[15]	***2013***	***TE***	***100***	***3±0.5***	***<1***	***100***	***Rib***
[62]	2013	TE	70	3±0.3	<1	100	Strip
[75]	***2015***	***TE/TM***	***100***	***3±0.8 (TE) 3±0.2 (TM)***	***<0.5***	***100 (TE) 122 (TM)***	***Strip***
[76]	***2016***	***TE***	***130***	***3±0.4***	***<0.5***	***20***	***SWG***
[77]	2017	TE&TM	100	3±0.7	NA	125	Strip
[78]	***2018***	***TE***	***185**** ***500*****	***3±0.3***	***<0.11***	***15***	***SWG-assisted Strip***
[69]	2018	TE&TM	100 (TE) 80 (TM)	3±0.6 (TE) 3±0.1 (TM)	∼1	75	Strip
[79]	2018	TE&TM	100	3±0.27	<0.74	25	SWG-assisted Slot
[71]	2018	TE	100	3±0.3	<0.3	60	Rib
[72]	2019	TE	100	3±0.5	<0.3	26.3	Rib

*: Measured bandwidth (limited by our test setup).
**: Simulated bandwidth.

Table 1.1: Comparison of mode-evolution-based, 2×2 power splitters on SOI platforms. The adiabatic couplers developed in this dissertation are highlighted in ***bold italics***. BW: Bandwidth; L_E: mode evolution region length. (copied from page 6)

7.3 Suggestions for Future Work

The adiabatic couplers demonstrated in this thesis were designed for broadband 3 dB power splitting. Following the design methodology shown in this thesis, compact, broadband adiabatic couplers with arbitrary splitting ratios should be able to be developed using asymmetric waveguide pairs with various width differences at Ports 3 and 4. Compact, polarization-insensitive, adiabatic couplers can also be obtained by using SWG-assisted strip waveguides. By increasing the width of the central strip and/or the length of the SWG fins, SWG-assisted strip waveguides should be optimized to support the mode evolution process for both the TE and TM modes. Since the effective indices of the system modes will increase, the

SWG period length should also be adjusted to avoid Bragg diffraction.

With regard to SWG CDCs, higher SLSRs should be obtained by optimizing the Gaussian apodization function or using other apodization functions. Although it was not obvious in my SWG CDCs, Fig. 5.3(b) has shown that corrugation apodization chirps the central wavelength of Bragg grating filters. This is because, while apodizing the coupling coefficient, apodized corrugations also change the effective indices for the gratings. Therefore, with a constant grating period length, the central wavelength will be chirped, and unexpected apodization phase noise will also be induced to distort the spectral responses, which results in increased bandwidths and decreased sidelobe suppressions. A phase correction method should be applied by adjusting the period length along the CDC so that the apodized coupling coefficients always locate at the same central wavelength along the device. Therefore, the apodization phase noise can be compensated and the sidelobe suppression can be improved.

Add-drop filters with bandwidths $>$100 nm can be achieved by chirping the Bragg period lengths (and the corresponding SWG period lengths) along the SWG CDCs. In principle, as the grating period changes along the length, the central wavelength also changes according to the contra-directinonal phase-match condition. Therefore, a chirped SWG CDC can be considered to be the sum of a large number of uniform SWG CDCs with various periods, and, thus, broad operating bandwidths can be obtained. Chirped Bragg grating devices typically need to have long total grating lengths to obtain large ERs. However, since the coupling strength of the SWG CDC is very large, chirped SWG CDCs can have much smaller footprints than those using conventional SOI waveguides.

CDC-based, PRBG, add-drop filters should be able to be developed using two asymmetric PRBG waveguides. To drop the reflected light, the demonstrated PRBG filters in Chapter 6 were cascaded with a Y-junction, which then induced a 6 dB loss in the reflected light at the refection port. CDC-based, PRBG filters can be designed so that the polarization-rotated, reflected light is separated from the input light without having the 6 dB loss or the need to use circulators. As shown in Fig. 7.1, the CDC-based, PRBG filters consist of two PRBG waveguides with waveguide widths, W_1 and W_2, respectively. The PRBG period should be chosen so that when the fundamental quasi-TE mode of the narrow waveguide is injected

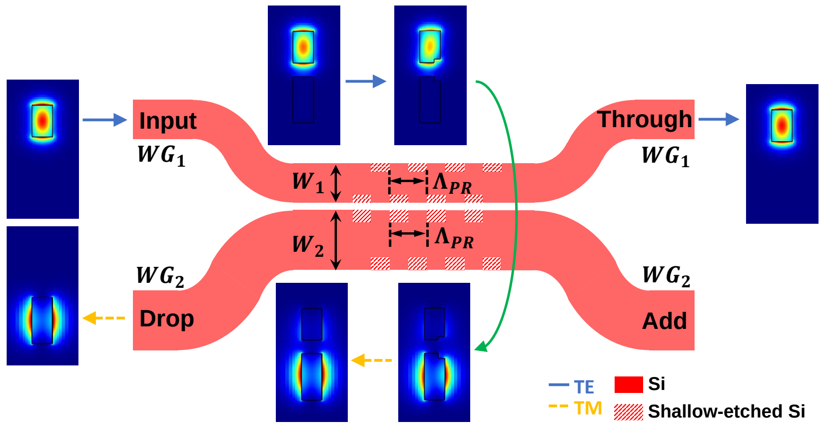

Figure 7.1: Schematic diagram of polarization-independent wavelength filtering and wavelength-selective polarization-rotating achieved by using an SOI, PRBG-based, band-rejection filter.

into the input port of the coupler the TE_{01} mode of the two waveguide system is the (predominantly) excited mode and is coupled to the contra-directionally propagating TM_{00} mode of the two waveguide system. The device also works in reverse if the fundamental quasi-TM mode of the wide waveguide is injected. Therefore, the light injected into one waveguide will be contra-directionally coupled to the other waveguide and have its polarization rotated at specific wavelengths.

In this dissertation, although I used an EBL tool to fabricate the SWG-based structures with features as small as 60 nm, as summarized in Table. 7.2, these devices could have been, and (to be commercially viable) should be, fabricated using 193 nm DUV immersion lithography, which has been used for silicon photonic devices with features as small as 50 nm [59].

Devices	EBL	193nm DUV Lithography *	193nm Immersion Lithography **
Rib Adiabatic Coupler	✓	✓	✓
Strip Adiabatic Coupler	✓	✓	✓
SWG Adiabatic Coupler	✓	×	✓
SWG-assisted Adiabatic Coupler	✓	✓	✓
SWG CDC	✓	×	✓
PRBG Band-rejection Filter	✓	✓	✓
PRBG Transmission Filter	✓	✓	✓

*: 90 nm minimum feature [174].
**: 50 nm minimum feature [59].
✓: process used in this dissertation for fabrication.

Table 7.2: Device Fabrication Compatibility.

Bibliography

[1] B. Jalali and S. Fathpour, "Silicon photonics," *J. Lightwave Technol.* **24**, 4600–4615 (2006).

[2] N. B. Feilchenfeld, F. G. Anderson, T. Barwicz, S. Chilstedt, Y. Ding, J. Ellis-Monaghan, D. M. Gill, C. Hedges, J. Hofrichter, F. Horst *et al.*, "An integrated silicon photonics technology for O-band datacom," *in 2015 IEEE International Electron Devices Meeting (IEDM)* (IEEE, 2015), pp. 25–7.

[3] D. Thomson, A. Zilkie, J. E. Bowers, T. Komljenovic, G. T. Reed, L. Vivien, D. Marris-Morini, E. Cassan, L. Virot, J.-M. Fédéli *et al.*, "Roadmap on silicon photonics," *Journal of Optics* **18**, 073003 (2016).

[4] W. Bogaerts, S. K. Selvaraja, P. Dumon, J. Brouckaert, K. De Vos, D. Van Thourhout, and R. Baets, "Silicon-on-insulator spectral filters fabricated with CMOS technology," *IEEE Journal of Selected Topics in Quantum Electronics* **16**, 33–44 (2010).

[5] B. Dong, X. Guo, C. P. Ho, B. Li, H. Wang, C. Lee, X. Luo, and G. Lo, "Silicon-on-insulator waveguide devices for broadband mid-infrared photonics," *IEEE Photonics Journal* **9**, 1–10 (2017).

[6] V. R. Almeida, R. R. Panepucci, and M. Lipson, "Nanotaper for compact mode conversion," *Optics Letters* **28**, 1302–1304 (2003).

[7] D. Taillaert, P. Bienstman, and R. Baets, "Compact efficient broadband grating coupler for silicon-on-insulator waveguides," *Optics Letters* **29**, 2749–2751 (2004).

[8] F. V. Laere, T. Claes, J. Schrauwen, S. Scheerlinck, W. Bogaerts, D. Taillaert, L. O'Faolain, D. V. Thourhout, and R. Baets, "Compact focusing grating couplers for silicon-on-insulator integrated circuits," *IEEE Photonics Technology Letters* **19**, 1919–1921 (2007).

[9] B. B. Bakir, A. V. De Gyves, R. Orobtchouk, P. Lyan, C. Porzier, A. Roman, and J.-M. Fedeli, "Low-loss ($<$1 dB) and polarization-insensitive edge fiber couplers fabricated on 200-mm silicon-on-insulator wafers," *IEEE Photonics Technology Letters* **22**, 739–741 (2010).

[10] P. Cheben, P. J. Bock, J. H. Schmid, J. Lapointe, S. Janz, D.-X. Xu, A. Densmore, A. Delâge, B. Lamontagne, and T. J. Hall, "Refractive index engineering with subwavelength gratings for efficient microphotonic couplers and planar waveguide multiplexers," *Optics Letters* **35**, 2526–2528 (2010).

[11] D. Benedikovic, P. Cheben, J. H. Schmid, D.-X. Xu, B. Lamontagne, S. Wang, J. Lapointe, R. Halir, A. O.-M. nux, S. Janz, and M. Dado, "Subwavelength index engineered surface grating coupler with sub-decibel efficiency for 220-nm silicon-on-insulator waveguides," *Optics Express* **23**, 22628–22635 (2015).

[12] Y. Wang, W. Shi, X. Wang, Z. Lu, M. Caverley, R. Bojko, L. Chrostowski, and N. A. F. Jaeger, "Design of broadband subwavelength grating couplers with low back reflection," *Optics Letters* **40**, 4647–4650 (2015).

[13] D.-X. Xu, A. Densmore, P. Waldron, J. Lapointe, E. Post, A. Delâge, S. Janz, P. Cheben, J. H. Schmid, and B. Lamontagne, "High bandwidth SOI photonic wire ring resonators using MMI couplers," *Optics Express* **15**, 3149–3155 (2007).

[14] Y. Zhang, S. Yang, A. E.-J. Lim, G.-Q. Lo, C. Galland, T. Baehr-Jones, and M. Hochberg, "A compact and low loss Y-junction for submicron silicon waveguide," *Optics Express* **21**, 1310–1316 (2013).

[15] H. Yun, W. Shi, Y. Wang, L. Chrostowski, and N. A. F. Jaeger, "2×2 adiabatic 3-dB coupler on silicon-on-insulator rib waveguides," *in Proc. SPIE, vol. 8915* (International Society for Optics and Photonics, 2013), vol. 8915, p. 89150V.

[16] S. Chen, Y. Shi, S. He, and D. Dai, "Low-loss and broadband 2×2 silicon thermo-optic Mach-Zehnder switch with bent directional couplers," *Optics Letters* **41**, 836–839 (2016).

[17] R. Boeck, N. A. F. Jaeger, N. Rouger, and L. Chrostowski, "Series-coupled silicon racetrack resonators and the vernier effect: theory and measurement," *Optics Express* **18**, 25151–25157 (2010).

[18] X. Wang, W. Shi, R. Vafaei, N. A. F. Jaeger, and L. Chrostowski, "Uniform and sampled Bragg gratings in SOI strip waveguides with sidewall corrugations," *IEEE Photonics Technol. Lett.* **23**, 290–292 (2011).

[19] W. Shi, X. Wang, W. Zhang, L. Chrostowski, and N. A. F. Jaeger, "Contradirectional couplers in silicon-on-insulator rib waveguides," *Optics Letters* **36**, 3999–4001 (2011).

[20] X. Wang, W. Shi, H. Yun, S. Grist, N. A. F. Jaeger, and L. Chrostowski, "Narrow-band waveguide Bragg gratings on SOI wafers with CMOS-compatible fabrication process," *Optics Express* **20**, 15547–15558 (2012).

[21] W. Shi, H. Yun, W. Zhang, C. Lin, T. K. Chang, Y. Wang, N. A. F. Jaeger, and L. Chrostowski, "Ultra-compact, high-Q silicon microdisk reflectors," *Optics Express* **20**, 21840–21846 (2012).

[22] W. Shi, X. Wang, C. Lin, H. Yun, Y. Liu, T. Baehr-Jones, M. Hochberg, N. A. F. Jaeger, and L. Chrostowski, "Silicon photonic grating-assisted, contra-directional couplers," *Optics Express* **21**, 3633–3650 (2013).

[23] P. D. Trinh, S. Yegnanarayanan, F. Coppinger, and B. Jalali, "Silicon-on-insulator (SOI) phased-array wavelength multi/demultiplexer with extremely low-polarization sensitivity," *IEEE Photonics Technology Letters* **9**, 940–942 (1997).

[24] P. Dumon, W. Bogaerts, D. Van Thourhout, D. Taillaert, R. Baets, J. Wouters, S. Beckx, and P. Jaenen, "Compact wavelength router based on a silicon-on-insulator arrayed waveguide grating pigtailed to a fiber array," *Optics Express* **14**, 664–669 (2006).

[25] S. Park, S.-G. Kim, J. Park, and G. Kim, "Echelle grating silicon multi/demultiplexers with single-reflection total internal reflectors," *Optics Express* **20**, 23582–23586 (2012).

[26] W. Shi, H. Yun, C. Lin, M. Greenberg, X. Wang, Y. Wang, S. T. Fard, J. Flueckiger, N. A. F. Jaeger, and L. Chrostowski, "Ultra-compact, flat-top demultiplexer using anti-reflection contra-directional couplers for CWDM networks on silicon," *Optics Express* **21**, 6733–6738 (2013).

[27] Q. Xu, B. Schmidt, S. Pradhan, and M. Lipson, "Micrometre-scale silicon electro-optic modulator," *Nature* **435**, 325–327 (2005).

[28] P. Dong, R. Shafiiha, S. Liao, H. Liang, N.-N. Feng, D. Feng, G. Li, X. Zheng, A. V. Krishnamoorthy, and M. Asghari, "Wavelength-tunable silicon microring modulator," *Optics Express* **18**, 10941–10946 (2010).

[29] G. T. Reed, G. Mashanovich, F. Y. Gardes, and D. J. Thomson, "Silicon optical modulators," *Nature Photonics* **4**, 518–526 (2010).

[30] T. Baehr-Jones, R. Ding, Y. Liu, A. Ayazi, T. Pinguet, N. C. Harris, M. Streshinsky, P. Lee, Y. Zhang, A. E.-J. Lim, T.-Y. Liow, S. H.-G. Teo, G.-Q. Lo, and M. Hochberg, "Ultralow drive voltage silicon traveling-wave modulator," *Optics Express* **20**, 12014–12020 (2012).

[31] D. Patel, S. Ghosh, M. Chagnon, A. Samani, V. Veerasubramanian, M. Osman, and D. V. Plant, "Design, analysis, and transmission system performance of a 41 GHz silicon photonic modulator," *Optics Express* **23**, 14263–14287 (2015).

[32] A. Samani, M. Chagnon, D. Patel, V. Veerasubramanian, S. Ghosh, M. Osman, Q. Zhong, and D. V. Plant, "A low-voltage 35-GHz silicon photonic modulator-enabled 112-Gb/s transmission system," *IEEE Photonics Journal* **7**, 1–13 (2015).

[33] M. Caverley, X. Wang, K. Murray, N. A. F. Jaeger, and L. Chrostowski, "Silicon-on-insulator modulators using a quarter-wave phase-shifted Bragg grating," *IEEE Photonics Technology Letters* **27**, 2331–2334 (2015).

[34] R. Dubé-Demers, S. LaRochelle, and W. Shi, "Ultrafast pulse-amplitude modulation with a femtojoule silicon photonic modulator," *Optica* **3**, 622–627 (2016).

[35] C. T. DeRose, D. C. Trotter, W. A. Zortman, A. L. Starbuck, M. Fisher, M. R. Watts, and P. S. Davids, "Ultra compact 45 GHz CMOS compatible Germanium waveguide photodiode with low dark current," *Optics Express* **19**, 24897–24904 (2011).

[36] J. J. Ackert, D. J. Thomson, L. Shen, A. C. Peacock, P. E. Jessop, G. T. Reed, G. Z. Mashanovich, and A. P. Knights, "High-speed detection at two micrometres with monolithic silicon photodiodes," *Nature Photonics* **9**, 393 (2015).

[37] Acacia Communications Inc., https://acacia-inc.com/product/silicon-photonic-integrated-circuits-pic/. Accessed: 2019-06-11.

[38] Luxtera, http://www.luxtera.com/silicon-photonics-technology/. Accessed: 2019-06-11.

[39] Finisar Corporation, http://investor.finisar.com/news-releases/news-release-details/finisar-introduces-400g-qsfp-dd-dr4-transceiver-data-center. Accessed: 2019-06-11.

[40] Intel® Silicion Photonics, https://www.intel.com/content/www/us/en/products/network-io/high-performance-fabrics/silicon-photonics.html. Accessed: 2019-06-11.

[41] Mellanox Technologies, http://www.mellanox.com/products/interconnect/ethernet-optical-transceivers.php. Accessed: 2019-06-11.

[42] C. Doerr, L. Chen, D. Vermeulen, T. Nielsen, S. Azemati, S. Stulz, G. McBrien, X.-M. Xu, B. Mikkelsen, M. Givehchi *et al.*, "Single-chip silicon photonics 100-Gb/s coherent transceiver," *in Optical Fiber Communication Conference* (Optical Society of America, 2014), pp. Th5C–1.

[43] V. Stojanović, R. J. Ram, M. Popović, S. Lin, S. Moazeni, M. Wade, C. Sun, L. Alloatti, A. Atabaki, F. Pavanello *et al.*, "Monolithic silicon-photonic platforms in state-of-the-art CMOS SOI processes," *Optics Express* **26**, 13106–13121 (2018).

[44] C. Sun, M. T. Wade, Y. Lee, J. S. Orcutt, L. Alloatti, M. S. Georgas, A. S. Waterman, J. M. Shainline, R. R. Avizienis, S. Lin *et al.*, "Single-chip microprocessor that communicates directly using light," *Nature* **528**, 534 (2015).

[45] P. Agnello, T. Ivers, C. Warm, R. Wise, R. Wachnik, D. Schepis, S. Sankaran, J. Norum, S. Luning, Y. Li *et al.*, "High performance 45-nm SOI technology with enhanced strain, porous low-k BEOL, and immersion lithography," *in 2006 International Electron Devices Meeting* (IEEE, 2006), pp. 1–4.

[46] S. Chen, W. Li, J. Wu, Q. Jiang, M. Tang, S. Shutts, S. N. Elliott, A. Sobiesierski, A. J. Seeds, I. Ross *et al.*, "Electrically pumped continuous-wave III–V quantum dot lasers on silicon," *Nature Photonics* **10**, 307 (2016).

[47] C. Xiong, D. M. Gill, J. E. Proesel, J. S. Orcutt, W. Haensch, and W. M. Green, "Monolithic 56 Gb/s silicon photonic pulse-amplitude modulation transmitter," *Optica* **3**, 1060–1065 (2016).

[48] A. H. Atabaki, S. Moazeni, F. Pavanello, H. Gevorgyan, J. Notaros, L. Alloatti, M. T. Wade, C. Sun, S. A. Kruger, H. Meng *et al.*, "Integrating photonics with silicon nanoelectronics for the next generation of systems on a chip," *Nature* **556**, 349 (2018).

[49] K. Zhong, J. Mo, R. Grzybowski, and A. P. T. Lau, "400 Gbps PAM-4 signal transmission using a monolithic Laser integrated silicon photonics transmitter," *in Optical Fiber Communication Conference* (Optical Society of America, 2019), pp. Tu2I–4.

[50] L. Chrostowski and M. Hochberg, *Silicon photonics design: from devices to systems* (Cambridge University Press, 2015).

[51] A. E.-J. Lim, J. Song, Q. Fang, C. Li, X. Tu, N. Duan, K. K. Chen, R. P.-C. Tern, and T.-Y. Liow, "Review of silicon photonics foundry efforts," *IEEE Journal of Selected Topics in Quantum Electronics* **20**, 405–416 (2013).

[52] imec, https://www.imec-int.com/en/integrated-silicon-photonics. Accessed: 2019-06-11.

[53] CEA-LETI, http://www.leti-cea.com/cea-tech/leti/english/Pages/Applied-Research/Facilities/photonics-plateform.aspx. Accessed: 2019-06-11.

[54] Advanced Micro Foundry PTE LTD, http://www.advmf.com/services/. Accessed: 2019-06-11.

[55] Innovations for High Performance Microelectronics, https://www.ihp-microelectronics.com/en/services/mpw-prototyping/sigec-bicmos-technologies.html. Accessed: 2019-06-11.

[56] Washington Nanofabrication Facility, https://www.wnf.washington.edu/about/services/. Accessed: 2019-06-11.

[57] Applied Nanotools Inc. - NanoSOI Fabrication Process, http://www.appliednt.com/nanosoi/. Accessed: 2019-06-11.

[58] L. Chrostowski, H. Shoman, M. Hammood, H. Yun, J. Jhoja, E. Luan, S. Lin, A. Mistry, D. Witt, N. A. F. Jaeger *et al.*, "Silicon photonic circuit design using rapid prototyping foundry process design kits," *IEEE Journal of Selected Topics in Quantum Electronics* (2019).

[59] S. K. Selvaraja, G. Winroth, S. Locorotondo, G. Murdoch, A. Milenin, C. Delvaux, P. Ong, S. Pathak, W. Xie, G. Sterckx, G. Lepage, D. V.

Thourhout, W. Bogaerts, J. V. Campenhout, and P. Absil, "193nm immersion lithography for high-performance silicon photonic circuits," *in Proc. SPIE, vol. 9052* (2014), vol. 9052, p. 90520F.

[60] T.-Y. Liow, J. Song, X. Tu, A. E.-J. Lim, Q. Fang, N. Duan, M. Yu, and G.-Q. Lo, "Silicon optical interconnect device technologies for 40 Gb/s and beyond," *IEEE Journal of Selected Topics in Quantum Electronics* **19**, 8200312–8200312 (2012).

[61] R. J. Bojko, J. Li, L. He, T. Baehr-Jones, M. Hochberg, and Y. Aida, "Electron beam lithography writing strategies for low loss, high confinement silicon optical waveguides," *Journal of Vacuum Science & Technology B, Nanotechnology and Microelectronics: Materials, Processing, Measurement, and Phenomena* **29**, 06F309 (2011).

[62] M. R. Watts, J. Sun, C. DeRose, D. C. Trotter, R. W. Young, and G. N. Nielson, "Adiabatic thermo-optic Mach–Zehnder switch," *Optics Letters* **38**, 733–735 (2013).

[63] K. Murray, Z. Lu, H. Jayatilleka, and L. Chrostowski, "Dense dissimilar waveguide routing for highly efficient thermo-optic switches on silicon," *Optics Express* **23**, 19575–19585 (2015).

[64] Z. Lu, K. Murray, H. Jayatilleka, and L. Chrostowski, "Michelson interferometer thermo-optic switch on soi with a 50-μw power consumption," *IEEE Photonics Technology Letters* **27**, 2319–2322 (2015).

[65] R. Li, D. Patel, E. El-Fiky, A. Samani, Z. Xing, Y. Wang, and D. V. Plant, "Silicon photonic dual-drive MIM based 56 Gb/s DAC-less and DSP-free PAM-4 transmission," *Optics Express* **26**, 5395–5407 (2018).

[66] Z. Lu, D. Celo, P. Dumais, E. Bernier, and L. Chrostowski, "Comparison of photonic 2$\times$2 3-dB couplers for 220 nm silicon-on-insulator platforms," *in 2015 IEEE 12th International Conference on Group IV Photonics (GFP)* (IEEE, 2015), pp. 57–58.

[67] T. A. Ramadan and R. M. Osgood, "Adiabatic couplers: design rules and optimization," *Journal of Lightwave Technology* **16**, 277 (1998).

[68] J. Xing, K. Xiong, H. Xu, Z. Li, X. Xiao, J. Yu, and Y. Yu, "Silicon-on-insulator-based adiabatic splitter with simultaneous tapering of velocity and coupling," *Optics Letters* **38**, 2221–2223 (2013).

[69] Y. Wang, L. Xu, H. Yun, M. Ma, A. Kumar, E. El-Fiky, R. Li, N. Abadíacalvo, L. Chrostowski, N. A. F. Jaeger *et al.*, "Polarization-independent mode-evolution-based coupler for the silicon-on-insulator platform," *IEEE Photonics Journal* **10**, 1–10 (2018).

[70] J. Jiang, D. J. Goodwill, P. Dumais, D. Celo, C. Zhang, M. Li, Y. Wei, F. Zhao, W. Liu, X. Tu, D. Geng, and E. Bernier, "Ultra low loss waveguide transitions for reticle-scale silicon nanophotonic routing," *IEEE Photonics Technology Letters* **29**, 2099–2102 (2017).

[71] D. Guo and T. Chu, "Compact broadband silicon 3 dB coupler based on shortcuts to adiabaticity," *Optics Letters* **43**, 4795–4798 (2018).

[72] Y.-J. Hung, Z.-Y. Li, H.-C. Chung, F.-C. Liang, M.-Y. Jung, T.-H. Yen, and S.-Y. Tseng, "Mode-evolution-based silicon-on-insulator 3 dB coupler using fast quasiadiabatic dynamics," *Optics Letters* **44**, 815–818 (2019).

[73] K. Solehmainen, M. Kapulainen, M. Harjanne, and T. Aalto, "Adiabatic and Multimode Interference Couplers on Silicon-on-Insulator," *IEEE Photon. Technol. Lett.* **18**, 2287–2289 (2006).

[74] L. Cao, A. Elshaari, A. Aboketaf, and S. Preble, "Adiabatic couplers in soi waveguides," *in Conference on Lasers and Electro-Optics* (Optical Society of America, 2010), p. CThAA2.

[75] H. Yun, Z. Lu, Y. Wang, W. Shi, L. Christowski, and N. A. F. Jaeger, "2×2 broadband adiabatic 3-db couplers on SOI strip waveguides for TE and TM modes," *in CLEO: Science and Innovations* (Optical Society of America, 2015), pp. STh1F–8.

[76] H. Yun, Y. Wang, F. Zhang, Z. Lu, S. Lin, L. Chrostowski, and N. A. F. Jaeger, "Broadband 2×2 adiabatic 3 dB coupler using Silicon-on-Insulator sub-wavelength grating waveguides," *Optics Letters* **41**, 3041–3044 (2016).

[77] L. Xu, Y. Wang, D. Patel, E. El-Fiky, Z. Xing, R. Li, M. G. Saber, M. Jacques, and D. V. Plant, "Polarization independent adiabatic 3-dB coupler for silicon-on-insulator," *in 2017 Conference on Lasers and Electro-Optics (CLEO)* (IEEE, 2017), pp. 1–2.

[78] H. Yun, L. Chrostowski, and N. A. F. Jaeger, "Ultra-broadband 2× 2 adiabatic 3 dB coupler using subwavelength-grating-assisted silicon-on-insulator strip waveguides," *Optics Letters* **43**, 1935–1938 (2018).

[79] L. Xu, Y. Wang, A. Kumar, E. El-Fiky, D. Mao, H. Tamazin, M. Jacques, Z. Xing, M. G. Saber, and D. V. Plant, "Compact high-performance adiabatic 3-dB coupler enabled by subwavelength grating slot in the silicon-on-insulator platform," *Optics Express* **26**, 29873–29885 (2018).

[80] Y. Wang, Z. Lu, M. Ma, H. Yun, F. Zhang, N. A. F. Jaeger, and L. Chrostowski, "Compact broadband directional couplers using subwavelength gratings," *IEEE Photonics Journal* **8**, 1–8 (2016).

[81] R. Halir, P. Cheben, J. M. Luque-Gonzlez, J. D. Sarmiento-Merenguel, J. H. Schmid, G. Wangemert-Prez, D.-X. Xu, S. Wang, A. Ortega-Moux, and . Molina-Fernndez, "Ultra-broadband nanophotonic beamsplitter using an anisotropic sub-wavelength metamaterial," *Laser & Photonics Reviews* **10**, 1039–1046 (2016).

[82] A. D. Simard and S. LaRochelle, "Complex apodized Bragg grating filters without circulators in silicon-on-insulator," *Optics Express* **23**, 16662–16675 (2015).

[83] B. Naghdi and L. R. Chen, "Silicon photonic contradirectional couplers using subwavelength grating waveguides," *Optics Express* **24**, 23429–23438 (2016).

[84] B. Naghdi and L. R. Chen, "Spectral engineering of subwavelength-grating-based contradirectional couplers," *Optics Express* **25**, 25310–25317 (2017).

[85] D. Charron, J. St-Yves, O. Jafari, S. LaRochelle, and W. Shi, "Subwavelength-grating contradirectional couplers for large stopband filters," *Optics Letters* **43**, 895–898 (2018).

[86] D. Dai, L. Liu, S. Gao, D.-X. Xu, and S. He, "Polarization management for silicon photonic integrated circuits," *Laser & Photonics Reviews* **7**, 303–328 (2012).

[87] D.-X. Xu, P. Cheben, D. Dalacu, A. Delâge, S. Janz, B. Lamontagne, M.-J. Picard, and W. N. Ye, "Eliminating the birefringence in silicon-on-insulator ridge waveguides by use of cladding stress," *Optics Letters* **29**, 2384–2386 (2004).

[88] C. Li, J. H. Song, J. Zhang, H. Zhang, S. Chen, M. Yu, and G. Q. Lo, "Silicon polarization independent microring resonator-based optical tunable filter circuit with fiber assembly," *Optics Express* **19**, 15429–15437 (2011).

[89] S. Pathak, M. Vanslembrouck, P. Dumon, D. V. Thourhout, and W. Bogaerts, “Compact SOI-based polarization diversity wavelength de-multiplexer circuit using two symmetric awgs,” *Optics Express* **20**, B493–B500 (2012).

[90] M. Ma, A. H. Park, Y. Wang, H. Shoman, F. Zhang, N. A. F. Jaeger, and L. Chrostowski, “Sub-wavelength grating-assisted polarization splitter-rotators for silicon-on-insulator platforms,” *Optics Express* **27**, 17581–17591 (2019).

[91] Y. Shani, R. Alferness, T. Koch, U. Koren, M. Oron, B. Miller, and M. Young, “Polarization rotation in asymmetric periodic loaded rib waveguides,” *Applied Physics Letters* **59**, 1278–1280 (1991).

[92] J. Van der Tol, J. Pedersen, E. Metaal, F. Hakimzadeh, Y. Oei, F. Groen, and I. Moerman, “Realization of a short integrated optic passive polarization converter,” *IEEE photonics technology letters* **7**, 893–895 (1995).

[93] T. Ando, T. Murata, H. Nakayama, J. Yamauchi, and H. Nakano, “Analysis and measurement of polarization conversion in a periodically loaded dielectric waveguide,” *IEEE Photonics Technology Letters* **14**, 1288–1290 (2002).

[94] H. Okayama, Y. Onawa, D. Shimura, H. Yaegashi, and H. Sasaki, “Polarization rotation Bragg grating using Si wire waveguide with non-vertical sidewall,” *Optics Express* **22**, 31371–31378 (2014).

[95] H. Yun, Z. Chen, Y. Wang, J. Fluekiger, M. Caverley, L. Chrostowski, and N. A. F. Jaeger, “Polarization-rotating, Bragg-grating filters on silicon-on-insulator strip waveguides using asymmetric periodic corner corrugations,” *Opt. Lett.* **40**, 5578–5581 (2015).

[96] H. Okayama, Y. Onawa, D. Shimura, H. Yaegashi, and H. Sasaki, “Silicon waveguide polarization rotation bragg grating with resonator cavity section,” *Japanese Journal of Applied Physics* **56**, 042502 (2017).

[97] H. Yun, L. Chrostowski, and N. A. F. Jaeger, “Narrow-band, polarization-independent, transmission filter in a silicon-on-insulator strip waveguide,” *Optics Letters* **44**, 847–850 (2019).

[98] R. Loiacono, G. T. Reed, G. Z. Mashanovich, R. Gwilliam, S. J. Henley, Y. Hu, R. Feldesh, and R. Jones, “Laser erasable implanted gratings for integrated silicon photonics,” *Optics Express* **19**, 10728–10734 (2011).

[99] Q. Fang, J. F. Song, X. Tu, L. Jia, X. Luo, M. Yu, and G. Q. Lo, "Carrier-induced silicon bragg grating filters with a pin junction," *IEEE Photonics Technology Letters* **25**, 810–812 (2013).

[100] D. T. H. Tan, K. Ikeda, and Y. Fainman, "Cladding-modulated Bragg gratings in silicon waveguides," *Optics Letters* **34**, 1357–1359 (2009).

[101] Y.-J. Hung, K.-H. Lin, C.-J. Wu, C.-Y. Wang, and Y.-J. Chen, "Narrowband reflection from weakly coupled cladding-modulated Bragg gratings," *IEEE J. Sel. Topics Quantum Electron.* **22**, 218–224 (2015).

[102] A. D. Simard, N. Ayotte, Y. Painchaud, S. Bedard, and S. LaRochelle, "Impact of sidewall roughness on integrated Bragg gratings," *Journal of Lightwave Technology* **29**, 3693–3704 (2011).

[103] H. Qiu, G. Jiang, T. Hu, H. Shao, P. Yu, J. Yang, and X. Jiang, "FSR-free add-drop filter based on silicon grating-assisted contradirectional couplers," *Optics Letters* **38**, 1–3 (2013).

[104] X. Wang, Y. Wang, J. Flueckiger, R. Bojko, A. Liu, A. Reid, J. Pond, N. A. F. Jaeger, and L. Chrostowski, "Precise control of the coupling coefficient through destructive interference in silicon waveguide Bragg gratings," *Optics Letters* **39**, 5519–5522 (2014).

[105] Z. Chen, J. Flueckiger, X. Wang, F. Zhang, H. Yun, Z. Lu, M. Caverley, Y. Wang, N. A. F. Jaeger, and L. Chrostowski, "Spiral Bragg grating waveguides for TM mode silicon photonics," *Optics Express* **23**, 25295–25307 (2015).

[106] M. Ma, Z. Chen, H. Yun, Y. Wang, X. Wang, N. A. F. Jaeger, and L. Chrostowski, "Apodized spiral Bragg grating waveguides in Silicon-on-Insulator," *IEEE Photonics Technology Letters* **30**, 111–114 (2018).

[107] T. E. Murphy, J. T. Hastings, and H. I. Smith, "Fabrication and characterization of narrow-band Bragg-reflection filters in silicon-on-insulator ridge waveguides," *Journal of Lightwave Technology* **19**, 1938–1942 (2001).

[108] R. Halir, A. Ortega-Moux, J. H. Schmid, C. Alonso-Ramos, J. Lapointe, D. X. Xu, J. G. Wangemert-Prez, . Molina-Fernndez, and S. Janz, "Recent advances in silicon waveguide devices using sub-wavelength gratings," *IEEE Journal of Selected Topics in Quantum Electronics* **20**, 279–291 (2014).

[109] R. Halir, P. J. Bock, P. Cheben, A. Ortega-Moñux, C. Alonso-Ramos, J. H. Schmid, J. Lapointe, D.-X. Xu, J. G. Wangüemert-Pérez, Í. Molina-Fernández *et al.*, "Waveguide sub-wavelength structures: a review of principles and applications," *Laser & Photonics Reviews* **9**, 25–49 (2015).

[110] P. Yeh and H. F. Taylor, "Contradirectional frequency-selective couplers for guided-wave optics," *Applied Optics* **19**, 2848–2855 (1980).

[111] A. Yariv and P. Yeh, *Photonics: optical electronics in modern communications* (Oxford Univ., 2006).

[112] J. Buus, M.-C. Amann, and D. J. Blumenthal, *Tunable laser diodes and related optical sources* (Wiley-Interscience New York, 2005).

[113] M. Hammood, A. Mistry, M. Ma, H. Yun, L. Chrostowski, and N. A. F. Jaeger, "Compact, silicon-on-insulator, series-cascaded, contradirectional-coupling-based filters with $>$50 dB adjacent channel isolation," *Optics Letters* **44**, 439–442 (2019).

[114] H. Yun, M. Hammood, S. Lin, L. Chrostowski, and N. A. F. Jaeger, "Broadband flat-top SOI add–drop filters using apodized sub-wavelength grating contradirectional couplers," *Optics letters* **44**, 4929–4932 (2019).

[115] P. Cheben, R. Halir, J. H. Schmid, H. A. Atwater, and D. R. Smith, "Subwavelength integrated photonics," *Nature* **560**, 565–572 (2018).

[116] S. Rytov, "Electromagnetic properties of a finely stratified medium," *Soviet Physics JEPT* **2**, 466–475 (1956).

[117] Z. Weissman and A. Hardy, "Modes of periodically segmented waveguides," *J. Lightw. Technol.* **11**, 1831–1838 (1993).

[118] Y. Wang, X. Wang, J. Flueckiger, H. Yun, W. Shi, R. Bojko, N. A. F. Jaeger, and L. Chrostowski, "Focusing sub-wavelength grating couplers with low back reflections for rapid prototyping of silicon photonic circuits," *Optics Express* **22**, 20652–20662 (2014).

[119] V. Donzella, A. Sherwali, J. Flueckiger, S. T. Fard, S. M. Grist, and L. Chrostowski, "Sub-wavelength grating components for integrated optics applications on SOI chips," *Optics Express* **22**, 21037–21050 (2014).

[120] V. Donzella, A. Sherwali, J. Flueckiger, S. M. Grist, S. T. Fard, and L. Chrostowski, "Design and fabrication of SOI micro-ring resonators based on sub-wavelength grating waveguides," *Optics Express* **23**, 4791–4803 (2015).

[121] E. Luan, H. Yun, L. Laplatine, Y. Dattner, D. M. Ratner, K. C. Cheung, and L. Chrostowski, "Enhanced sensitivity of subwavelength multibox waveguide microring resonator label-free biosensors," *IEEE Journal of Selected Topics in Quantum Electronics* **25**, 1–11 (2019).

[122] J. Wang, I. Glesk, and L. R. Chen, "Subwavelength grating filtering devices," *Optics Express* **22**, 15335–15345 (2014).

[123] P. Cheben, J. Čtyroký, J. H. Schmid, S. Wang, J. Lapointe, J. G. Wangüemert-Pérez, I. nigo Molina-Fernández, A. O.-M. nux, R. Halir, D. Melati, D. Xu, S. Janz, and M. Dado, "Bragg filter bandwidth engineering in subwavelength grating metamaterial waveguides," *Optics Letters* **44**, 1043–1046 (2019).

[124] A. Maese-Novo, R. Halir, S. Romero-García, D. Pérez-Galacho, L. Zavargo-Peche, A. O.-M. nux, I. Molina-Fernández, J. G. Wangüemert-Pérez, and P. Cheben, "Wavelength independent multimode interference coupler," *Optics Express* **21**, 7033–7040 (2013).

[125] R. Halir, A. Maese-Novo, A. O.-M. nux, I. Molina-Fernández, J. G. Wangüemert-Pérez, P. Cheben, D.-X. Xu, J. H. Schmid, and S. Janz, "Colorless directional coupler with dispersion engineered sub-wavelength structure," *Optics Express* **20**, 13470–13477 (2012).

[126] Y. Wang, M. Ma, H. Yun, Z. Lu, X. Wang, N. A. F. Jaeger, and L. Chrostowski, "Ultra-compact sub-wavelength grating polarization splitter-rotator for silicon-on-insulator platform," *IEEE Photonics Journal* **8**, 1–9 (2016).

[127] L. Liu, Q. Deng, and Z. Zhou, "Manipulation of beat length and wavelength dependence of a polarization beam splitter using a subwavelength grating," *Optics Letters* **41**, 5126–5129 (2016).

[128] H. Okayama, Y. Onawa, D. Shimura, H. Yaegashi, and H. Sasaki, "Silicon waveguide polarization rotator sampled Bragg grating," *Opt. Lett.* **42**, 2142–2144 (2017).

[129] H. Okayama, Y. Onawa, D. Shimura, H. Yaegashi, and H. Sasaki, "Polarization rotation Bragg grating using si waveguide with top surface groove grating and terrace," *Japanese Journal of Applied Physics* **57**, 042201 (2018).

[130] C. Carathéodory, "Untersuchungen über die grundlagen der thermodynamik," *Mathematische Annalen* **67**, 355–386 (1909).

[131] L. Tisza, *Generalized thermodynamics*, vol. 1 (MIT press Cambridge, 1966).

[132] M. Cowperthwaite and T. Ahrens, "Thermodynamics of the adiabatic expansion of a mixture of two phases," *American Journal of Physics* **35**, 951–955 (1967).

[133] M. Born, "Physical aspects of quantum mechanics," (1927).

[134] M. Born and V. Fock, "Beweis des adiabatensatzes," *Zeitschrift für Physik* **51**, 165–180 (1928).

[135] T. Kato, "On the adiabatic theorem of quantum mechanics," *Journal of the Physical Society of Japan* **5**, 435–439 (1950).

[136] Y. Fu, T. Ye, W. Tang, and T. Chu, "Efficient adiabatic silicon-on-insulator waveguide taper," *Photonics Research* **2**, A41–A44 (2014).

[137] X. Sun, H.-C. Liu, and A. Yariv, "Adiabaticity criterion and the shortest adiabatic mode transformer in a coupled-waveguide system," *Opt. Lett.* **34**, 280–282 (2009).

[138] Y. Shani, C. H. Henry, R. Kistler, R. Kazarinov, and K. Orlowsky, "Integrated optic adiabatic polarization splitter on silicon," *Applied Physics Letters* **56**, 120–121 (1990).

[139] M. Watts, H. Haus, and E. Ippen, "Integrated mode-evolution-based polarization splitter," *Optics letters* **30**, 967–969 (2005).

[140] J. Zhang, M. Yu, G.-Q. Lo, and D.-L. Kwong, "Silicon-waveguide-based mode evolution polarization rotator," *IEEE Journal of selected topics in quantum electronics* **16**, 53–60 (2009).

[141] J. Schmid, B. Lamontagne, P. Cheben, A. Delâge, S. Janz, A. Densmore, J. Lapointe, E. Post, P. Waldron, and D.-X. Xu, "Mode converters for coupling to high aspect ratio silicon-on-insulator channel waveguides," *IEEE Photonics Technology Letters* **19**, 855–857 (2007).

[142] R. Palmer, L. Alloatti, D. Korn, W. Heni, P. Schindler, J. Bolten, M. Karl, M. Waldow, T. Wahlbrink, W. Freude *et al.*, "Low-loss silicon strip-to-slot mode converters," *IEEE Photonics Journal* **5**, 2200409–2200409 (2013).

[143] Y. Silberberg, P. Perlmutter, and J. Baran, "Digital optical switch," *Applied Physics Letters* **51**, 1230–1232 (1987).

[144] R. Adar, C. H. Henry, R. F. Kazarinov, R. Kistler, and G. R. Weber, "Adiabatic 3-dB Couplers, Filters, and Multiplexers Made with Silica Waveguides on Silicon," *J. Lightwave Technol.* **10**, 46–50 (1992).

[145] W. Yuan, S. Kim, W. H. Steier, and H. R. Fetterman, "Electrooptic Polymeric Digital Optical Switches (DOSs) With Adiabatic Couplers," *IEEE Photon. Technol. Lett.* **17**, 2568–2570 (2005).

[146] S. J. Spector, M. W. Geis, G.-R.Zhou, M. E. Grein, F. Gan, M. Popović, J. U. Yoon, D. M. Lennon, E. P. Ippen, F. X. Kärtner, and T. M. Lyszczarz, "CMOS-compatible dual-output silicon modulator for analog signal processing," *Optics Express* **16**, 11027–11031 (2008).

[147] L. Vivien, F. Grillot, E. Cassan, D. Pascal, S. Lardenois, A. Lupu, S. Laval, M. Heitzmann, and J.-M. Fédéli, "Comparison between strip and rib SOI microwaveguides for intra-chip light distribution," *Optical Materials* **27**, 756–762 (2005).

[148] W. Bogaerts and S. K. Selvaraja, "Compact single-mode silicon hybrid rib/strip waveguide with adiabatic bends," *IEEE Photonics Journal* **3**, 422–432 (2011).

[149] W. Bogaerts, P. De Heyn, T. Van Vaerenbergh, K. De Vos, S. Kumar Selvaraja, T. Claes, P. Dumon, P. Bienstman, D. Van Thourhout, and R. Baets, "Silicon microring resonators," *Laser & Photonics Reviews* **6**, 47–73 (2012).

[150] M. Á. Guillén-Torres, K. Murray, H. Yun, M. Caverley, E. Cretu, L. Chrostowski, and N. A. F. Jaeger, "Effects of backscattering in high-q, large-area silicon-on-insulator ring resonators," *Optics Letters* **41**, 1538–1541 (2016).

[151] M. Caverley, H. Yun, L. Chrostowski, and N. A. F. Jaeger, "A low-power biasing scheme for silicon-on-insulator traveling-wave modulators," *in 2015 IEEE 12th International Conference on Group IV Photonics (GFP)* (IEEE, 2015), pp. 141–142.

[152] D. Patel, V. Veerasubramanian, S. Ghosh, A. Samani, Q. Zhong, and D. V. Plant, "High-speed compact silicon photonic michelson interferometric modulator," *Optics Express* **22**, 26788–26802 (2014).

[153] W. A. Zortman, D. C. Trotter, and M. R. Watts, "Silicon photonics manufacturing," *Optics Express* **18**, 23598–23607 (2010).

[154] E. D. Palik, *Handbook of Optical Constants of Solids* (Academic Press, 1998).

[155] Z. Lu, J. Jhoja, J. Klein, X. Wang, A. Liu, J. Flueckiger, J. Pond, and L. Chrostowski, “Performance prediction for silicon photonics integrated circuits with layout-dependent correlated manufacturing variability,” *Optics Express* **25**, 9712–9733 (2017).

[156] B. Liu, Y. Zhang, Y. He, X. Jiang, J. Peng, C. Qiu, and Y. Su, “Silicon photonic bandpass filter based on apodized subwavelength grating with high suppression ratio and short coupling length,” *Optics Express* **25**, 11359–11364 (2017).

[157] J. St-Yves, H. Bahrami, P. Jean, S. LaRochelle, and W. Shi, “Widely bandwidth-tunable silicon filter with an unlimited free-spectral range,” *Optics Letters* **40**, 5471–5474 (2015).

[158] J. Jiang, H. Qiu, G. Wang, Y. Li, T. Dai, X. Wang, H. Yu, J. Yang, and X. Jiang, “Broadband tunable filter based on the loop of multimode Bragg grating,” *Optics Express* **26**, 559–566 (2018).

[159] J. Pond, X. Wang, J. Flueckiger, A. Reid, J. Niegemann, A. Liu, and L. Chrostowski, “Design and optimization of photolithography friendly photonic components,” *in Proc. SPIE, vol. 9751* (2016), vol. 9751, p. 97510V.

[160] V. Veerasubramanian, G. Beaudin, A. Giguère, B. Le Drogoff, V. Aimez, and A. G. Kirk, “Waveguide-coupled drop filters on soi using quarter-wave shifted sidewalled grating resonators,” *Optics Express* **20**, 15983–15990 (2012).

[161] K. Voigt, L. Zimmermann, G. Winzer, T. Mitze, J. Bruns, K. Petermann, B. Huttl, and C. Schubert, “Performance of 40-Gb/s DPSK demodulator in SOI-technology,” *IEEE Photonics Technology Letters* **20**, 614–616 (2008).

[162] L. Jia, T.-Y. Liow, J. Song, X. Luo, N. Duan, S. C. Koh, Q. Fang, M. Yu, and G. Lo, “Compact optical polarization rotators based on an asymmetric silicon waveguide,” *Photonics Technology Letters, IEEE* **25**, 2229–2232 (2013).

[163] K. Goi, A. Oka, H. Kusaka, K. Ogawa, T.-Y. Liow, X. Tu, G.-Q. Lo, and D.-L. Kwong, “Low-loss partial rib polarization rotator consisting only of silicon core and silica cladding,” *Optics Letters* **40**, 1410–1413 (2015).

[164] MODE, https://www.lumerical.com/products/mode/. Accessed: 2019-06-11.

[165] W. Bogaerts, R. Baets, P. Dumon, V. Wiaux, S. Beckx, D. Taillaert, B. Luyssaert, J. Van Campenhout, P. Bienstman, and D. Van Thourhout, “Nanophotonic waveguides in silicon-on-insulator fabricated with cmos technology,” *Journal of Lightwave Technology* **23**, 401–412 (2005).

[166] S. K. Selvaraja, P. Jaenen, W. Bogaerts, D. Van Thourhout, P. Dumon, and R. Baets, “Fabrication of photonic wire and crystal circuits in silicon-on-insulator using 193-nm optical lithography,” *Journal of Lightwave Technology* **27**, 4076–4083 (2009).

[167] H.-C. Kim, K. Ikeda, and Y. Fainman, “Tunable transmission resonant filter and modulator with vertical gratings,” *J. Lightwave Technol.* **25**, 1147–1151 (2007).

[168] X. Wang, W. Shi, S. Grist, H. Yun, N. A. F. Jaeger, and L. Chrostowski, “Narrow-band transmission filter using phase-shifted Bragg gratings in SOI waveguide,” *in IEEE Photonic Society 24th Annual Meeting* (2011), pp. 869–870.

[169] X. Wang, J. Flueckiger, S. Schmidt, S. Grist, S. T. Fard, J. Kirk, M. Doerfler, K. C. Cheung, D. M. Ratner, and L. Chrostowski, “A silicon photonic biosensor using phase-shifted Bragg gratings in slot waveguide,” *Journal of Biophotonics* **6**, 821–828 (2013).

[170] E. Luan, H. Yun, M. Ma, D. M. Ratner, K. C. Cheung, and L. Chrostowski, “Label-free biosensing with a multi-box sub-wavelength phase-shifted bragg grating waveguide,” *Biomedical optics express* **10**, 4825–4838 (2019).

[171] M. Burla, L. R. Cortés, M. Li, X. Wang, L. Chrostowski, and J. Azaña, “Integrated waveguide Bragg gratings for microwave photonics signal processing,” *Opt. Express* **21**, 25120–25147 (2013).

[172] W. Zhang and J. Yao, “A fully reconfigurable waveguide bragg grating for programmable photonic signal processing,” *Nature Communications* **9**, 1–9 (2018).

[173] Z. Chen, “Spiral Bragg gratings for TM mode silicon photonics,” Master’s thesis, University of British Columbia (2015).

[174] CompoundTek, https://compoundtek.com/our-services/?noredirect=true. Accessed: 2019-12-10.

Appendix A

Publications

A.1 Journal Publications

A.1.1 First Author

1. **Han Yun**, Mustafa Hammood, Stephen Lin, Lukas Chrostowski, and Nicolas A. F. Jaeger, "Broadband Flat-top Silicon Photonic Add-drop Filters using Apodized Sub-wavelength Grating Contra-directional Couplers," *Optics Letters*, 44, pp. 4929-4932, 2019.

2. **Han Yun**, Lukas Chrostowski, and Nicolas A. F. Jaeger, "Narrow-band, polarization-independent, transmission filter in a silicon-on-insulator strip waveguide," *Optics Letters*, 44, pp. 847-850, 2019.

3. **Han Yun**, Lukas Chrostowski, and Nicolas A. F. Jaeger, "Ultra-broadband 2×2 adiabatic 3 dB coupler using subwavelength-grating-assisted silicon-on-insulator strip waveguides," *Optics Letters*, 43, pp. 1935-1938, 2018.

4. **Han Yun**, Yun Wang, Fan Zhang, Zeqin Lu, Stephen Lin, Lukas Chrostowski, and Nicolas A. F. Jaeger, "Broadband 2×2 adiabatic 3 dB coupler using silicon-on-insulator sub-wavelength grating waveguides," *Optics Letters*, 41, pp. 3041-3044, 2016.

5. **Han Yun**, Zhitian Chen, Yun Wang, Jonas Flueckiger, Michael Caverley,

Lukas Chrostowski, and Nicolas A. F. Jaeger, "Polarization-rotating, Bragg-grating filters on silicon-on-insulator strip waveguides using asymmetric periodic corner corrugations," *Optics Letters*, 40, pp. 5578-5581, 2015.

A.1.2 Co-author

1. Stehpen Lin, Mustafa Hammood, **Han Yun**, Enxiao Luan, Nicolas A. F. Jaeger, and Lukas Chrostowski, "Computational Lithography for Silicon Photonics Design," *IEEE Journal of Selected Topics in Quantum Electronics*, vol. 26, no. 2, pp. 1-8, 2020.

2. Enxiao Luan, **Han Yun**, Minglei Ma, Daniel M. Ratner, Karen C. Cheung, and Lukas Chrostowski, "Label-free biosensing with a multi-box sub-wavelength phase-shifted Bragg grating waveguide," Biomed. Opt. Express 10, pp. 4825-4838, 2019.

3. Lukas Chrostowski, Hossam Shoman, Mustafa Hammood, **Han Yun**, Jaspreet Jhoja, Enxiao Luan, Stephen Lin, Ajay Mistry, Donald Witt, Nicolas A. F. Jaeger, Sudip Shekhar, Hasitha Jayatilleka, Philippe Jean, Simon B.-de. Villers, Jonathan Cauchon, Wei Shi, Cameron Horvath, Jocelyn N. Westwood-Bachman, Kevin Setzer, Mirwais Aktary, N. Sahne Patrick, Richard Bojko, Amin Khavasi, Xu Wang, Thomas Ferreira de Lima, Alexander N. Tait, Paul R. Prucnal, David E. Hagan, Doris Stevanovic, and Andy P. Knights,"Silicon Photonic Circuit Design Using Rapid Prototyping Foundry Process Design Kits," *IEEE Journal of Selected Topics in Quantum Electronics*, vol. 25, no. 5, pp. 1-26, 2019 (invited).

4. Mustafa Hammood, Ajay Mistry, Minglei Ma, **Han Yun**, Lukas Chrostowski, and Nicolas A. F. Jaeger, "Compact, silicon-on-insulator, series-cascaded, contra-directional-coupling-based filters with >50dB adjacent channel isolation," *Optics Letters*, vol. 44, pp. 439-442, 2019.

5. Rui Cheng, **Han Yun**, Stephen Lin, Ya Han, and Lukas Chrostowski, "Apodization profile amplification of silicon integrated Bragg gratings through lateral phase delays," *Optics Letters*, vol. 44, pp. 435-438, 2019.

6. Yun Wang, Luhua Xu, **Han Yun**, Minglei Ma, Amar Kumar, Eslam EI-Fiky, Rui Li, Nicolás Abadiacalvo, Lukas Chrostowski, Nicolas A. F. Jaeger, and David V. Plant, "Polarization-Independent Mode-Evolution-Based Coupler for the Silicon-on-Insulator Platform," *IEEE Photonics Journal*, vol. 10, no. 3, pp. 1-10, 2018

7. Enxiao Luan, **Han Yun**, Loic Laplatine, Yonathan Dattner, Daniel M. Ratner, Karen C. Cheung, and Lukas Chrostowski, "Enhanced Sensitivity of Subwavelength Multibox Waveguide Microring Resonator Label-Free Biosensors," *IEEE Journal of Selected Topics in Quantum Electronics*, vol. 25, no. 3, pp. 1-11, 2018 (Invited).

8. Minglei Ma, Zhitian Chen, **Han Yun**, Yun Wang, Xu Wang, Nicolas A. F. Jaeger, and Lukas Chrostowski, "Apodized Spiral Bragg Grating Waveguides in Silicon-on-Insulator," *IEEE Photonics Technology Letters*, vol. 30, no. 1, pp. 111-114, 2018.

9. Fan Zhang, **Han Yun**, Yun Wang, Zeqin Lu, Lukas Chrostowski, and Nicolas A. F. Jaeger, "Compact broadband polarization beam splitter using a symmetric directional coupler with sinusoidal bends", *Optics Letters*, vol. 42, pp.235-238, 2017.

10. Yun Wang, Minglei Ma, **Han Yun**, Zeqin Lu, Xu Wang, Nicolas A. F. Jaeger, and Lukas Chrostowski, "Ultra-Compact, Sub-Wavelength Grating Polarization Splitter-Rotator for Silicon-on-Insulator Platform", *IEEE Photonics Journal*, vol. 8, no. 6, pp. 1-9, 2016.

11. Yun Wang, Zeqin Lu, Minglei Ma, **Han Yun**, Fan Zhang, and Nicolas A. F. Jaeger, and Lukas Chrostowski, "Compact Broadband Directional Couplers Using Sub-wavelength Gratings", *IEEE Photonics Journal*, vol. 8, no. 3, pp. 1-8, 2016.

12. Miguel Á. Guillén-Torres, Kyle Murray, **Han Yun**, Michael Caverley, Edmond Cretu, Lukas Chrostowski, and Nicolas A. F. Jaeger, "Effects of backscattering in high-Q, large-area silicon-on-insulator ring resonators", *Optics Letters*, vol. 41, pp.1538-1541, 2016.

13. Zeqin Lu, **Han Yun**, Yun Wang, Zhitian Chen, Fan Zhang, Nicolas A. F. Jaeger, and Lukas Chrostowski, "Broadband silicon photonic directional coupler using asymmetric-waveguide based phase control," *Optics Express*, 23(3):3795-3808, 2015.

14. Yun Wang, **Han Yun**, Zeqin Lu, Richard Bojko, Wei Shi, Xu Wang, Jonas Flueckiger, Fan Zhang, Michael Caverley, Nicolas A. F. Jaeger, "Apodized focusing fully etched sub-wavelength grating couplers," *IEEE Photonics Journal*, vol. 7, no. 3, pp. 1-10, 2015.

15. Zhitian Chen, Jonas Flueckiger, Xu Wang, Fan Zhang, **Han Yun**, Zeqin Lu, Michael Caverley, Yun Wang, Nicolas A. F. Jaeger, and Lukas Chrostowski, "Spiral Bragg grating waveguides for TM mode silicon photonics," *Optics Express*, 23, pp. 25295-25307, 2015.

16. Yun Wang, Xu Wang, Jonas Flueckiger, **Han Yun**, Wei Shi, Richard Bojko, Nicolas A. F. Jaeger, and Lukas Chrostowski, "Focusing sub-wavelength grating couplers with low back reflections for rapid prototyping of silicon photonic circuits," *Optics Express*, 22(17):20652-20662, 2014.

17. Wei Shi, **Han Yun**, Charlie Lin, Jonas Flueckiger, Nicolas A. F. Jaeger, and Lukas Chrostowski, "Coupler-apodized Bragg-grating add-drop filter," *Optics Letters*, 38, pp. 3068-3070, 2013.

18. Wei Shi, **Han Yun**, Charlie Lin, Mark Greenberg, Xu Wang, Yun Wang, Sahba Talebi Fard, Jonas Flueckiger, Nicolas A. F. Jaeger, and Lukas Chrostowski, "Ultra-compact, flat-top demultiplexer using anti-reflection contra-directional couplers for CWDM networks on silicon," *Optics Express*, 21, pp. 6733-6738, 2013.

19. Wei Shi, Xu Wang, Charlie Lin, **Han Yun**, Yang Liu, Tom Baehr-Jones, Michael Hochberg, Nicolas A. F. Jaeger, and Lukas Chrostowski, "Silicon photonic grating-assisted, contra-directional couplers," *Optics Express*, 21, pp. 3633-3650, 2013.

20. Robert Boeck, Jonas Flueckiger, **Han Yun**, Lukas Chrostowski, and Nicolas A. F. Jaeger, "High performance Vernier racetrack resonators," *Optics Letters*, 37, pp. 5199-5201, 2012.

21. Wei Shi, **Han Yun**, Wen Zhang, Charlie Lin, Ting Kai Chang, Yun Wang, Nicolas A. F. Jaeger, and Lukas Chrostowski, "Ultra-compact, high-Q silicon microdisk reflectors," *Optics Express*, 20, pp. 21840-21846, 2012.

22. Xu Wang, Wei Shi, **Han Yun**, Samantha Grist, Nicolas A. F. Jaeger, and Lukas Chrostowski, "Narrow-band waveguide Bragg gratings on SOI wafers with CMOS-compatible fabrication process," *Optics Express*, 20, pp. 15547-15558, 2012.

23. Wei Shi, Xu Wang, Wen Zhang, **Han Yun**, Charlie Lin, Lukas Chrostowski, and Nicolas A. F. Jaeger, "Grating-coupled silicon microring resonators," *Applied Physics Letters*, 100, pp. 121118, 2012.

A.2 Conference Proceedings

A.2.1 First Author

1. **Han Yun**, Mustafa Hammood, Lukas Chrostowski, and Nicolas A. F. Jaeger,"Optical Add-drop Filters using Cladding-modulated Sub-wavelength Grating Contra-directional Couplers for Silicon-on-Insulator Platforms," *IEEE IEMCON 2019 Conference*, Vancouver, Canada, 2019.

2. **Han Yun**, Mustafa Hammood, Lukas Chrostowski, and Nicolas A. F. Jaeger,"Wideband, Flat-top, SOI Filter using an Apodized Sub-wavelength-grating Contra-directional Coupler," *2019 IEEE 16th International Conference on Group IV Photonics (GFP)*, Singapore, 2019.

3. **Han Yun** and Nicolas A. F. Jaeger, "Broadband optical power splitters for photonic integrated circuits using Si metamaterial on an SOI platform," *Emerging Technologies 2018: Communications, Microsystems, Optoelectronics, Sensors*, Whistler, Canada, 2018 (Invited).

4. **Han Yun**, Jonas Flueckiger, Zhitian Chen, Yun Wang, Lukas Chrostowski, and Nicolas A. F. Jaeger, "A wavelength-selective polarization rotating reflector using a partially-etched asymmetric Bragg grating on an SOI strip waveguide," *IEEE 12th International Conference on Group IV Photonics*, FA3, Vancouver, Canada (08/2015).

5. **Han Yun**, Zeqin Lu, Yun Wang, Wei Shi, Lukas Chrostowski, and Nicolas A. F. Jaeger, "2×2 Broadband adiabatic 3-dB couplers on SOI strip waveguides for TE and TM modes," in *CLEO (Conference on Lasers and Electro-Optics): 2015, (Optical Society of America, 2015)*, p. STh1F.8. (05/2015).

6. **Han Yun**, Wei Shi, Yun Wang, Lukas Chrostowski, and Nicolas A. F. Jaeger, "2×2 Adiabatic 3-dB coupler on silicon-on-insulator rib waveguides," *Proceedings of SPIE*, 8915, 89150V-1–89150V-6 (2013).

A.2.2 Co-author

1. Mustafa Hammood, Ajay Mistry, **Han Yun**, Minglei Ma, Lukas Chrostowski, and Nicolas A. F. Jaeger, "Four-channel, Silicon Photonic, Wavelength Multiplexer-Demultiplexer with High Channel Isolations," 2020 Optical Fiber Communications Conference and Exhibition (OFC) (accepted).

2. Enxiao Luan*, **Han Yun***, Stephen Lin, Karen C. Cheung, Lukas Chrostowski, and Nicolas A. F. Jaeger, "Phase-shifted Bragg grating-based Mach-Zehnder Interferometer Sensor using an Intensity Interrogation Scheme," 2020 Optical Fiber Communications Conference and Exhibition (OFC), (accepted; *: These two authors share equal contribution).

3. Minglei Ma, Yun Wang, Anthony Park, **Han Yun**, Nicolas A. F. Jaeger, and Lukas Chrostowski, "Broadband Polarization Splitter-Rotator using Subwavelength Grating Assisted Adiabatic Waveguides," *2018 IEEE 15th International Conference on Group IV Photonics (GFP)*, pp. 1-2, 2018.

4. Enxiao Luan, **Han Yun**, Loic Laplatine, Jonas Flueckiger, Yonathan Dattner, Daniel Ratner, Karen C. Cheung, and Lukas Chrostowski, "Sub-wavelength

multi-box waveguide-based label-free sensors," *Proceedings of SPIE 10535, Integrated Optics: Devices, Materials, and Technologies XXII*, 105350H, 2018.

5. Zeqin Lu, Minglei Ma, **Han Yun**, Yun Wang, Nicolas A. F. Jaeger, and Lukas Chrostowski, "Silicon photonic polarization beamsplitter and rotator for on-chip polarization control," *2016 IEEE 13th International Conference on Group IV Photonics (GFP)*, pp. 70-71, 2016.

6. Minglei Ma, Kyle Murray, Mengyuan Ye, Stephen Lin, Yun Wang, Zeqin Lu, **Han Yun**, Ricky Hu, Nicolas A. F. Jaeger, and Lukas Chrostowski, "Silicon Photonic Polarization Receiver with Automated Stabilization for Arbitrary Input Polarizations," *Conference on Lasers and Electro-Optics*, paper STu4G.8., 2016.

7. Yun Wang, **Han Yun**, Zeqin Lu, Nicolas A. F. Jaeger, and Lukas Chrostowski, "State-of-the-art sub-wavelength grating couplers for silicon-on-insulator platform," *2016 IEEE Canadian Conference on Electrical and Computer Engineering (CCECE)*, pp.1-4, 2016.

8. Yun Wang, **Han Yun**, Nicolas A. F. Jaeger, and Lukas Chrostowski, "Broadband Bidirectional Vertical Grating Coupler," *Optical Fiber Communication Conference*, paper W2A.16, 2016.

9. Michael Caverley, **Han Yun**, Lukas Chrostowski, and Nicolas A. F. Jaeger, "A low-power biasing scheme for silicon-on-insulator traveling-wave modulators," *Group IV Photonics (GFP), 2015 IEEE 12th International Conference on*, WP54, 141–142 (08/2015).

10. Zeqin Lu, **Han Yun**, Yun Wang, Zhitian Chen, Fan Zhang, Nicolas A. F. Jaeger, and Lukas Chrostowski, "Asymmetric-waveguide-assisted 3-dB Broadband Directional Coupler," *CLEO (Conference on Lasers and Electro-Optics): 2015*, SM1I.8. (05/2015).

11. Yun Wang, **Han Yun**, Zeqin Lu, Richard Bojko, Fan Zhang, Michael Caverley, Nicolas A. F. Jaeger, and Lukas Chrostowski, "Apodized Focusing Fully

Etched Sub-wavelength Grating Couplers," *CLEO (Conference on Lasers and Electro-Optics): 2015*, SM1I.6. (05/2015).

12. Fan Zhang, **Han Yun**, Volentina Donzella, Zeqin Lu, Yun Wang, Zhitian Chen, Lukas Chrostowski, and Nicolas A. F. Jaeger, "Sinusoidal Anti-coupling SOI Strip Waveguides," *CLEO (Conference on Lasers and Electro-Optics): 2015*, (05/2015).

13. Zhitian Chen, Jonas Flueckiger, Xu Wang, **Han Yun**, Yun Wang, Zeqin Lu, Fan Zhang, Nicolas A. F. Jaeger, and Lukas Chrostowski, "Bragg Grating Spiral Strip Waveguide Filters for TM Modes," *CLEO (Conference on Lasers and Electro-Optics): 2015*, 05/2015.

14. Yun Wang, Jonas Flueckiger, **Han Yun**, Richard Bojko, Nicolas A. F. Jaeger, and Lukas Chrostowski, "Focusing sub-wavelength grating coupler," in *Photonics Conference (IPC), 2014 IEEE*, pages 552–553. IEEE, 2014.

15. Xu Wang, **Han Yun**, Nicolas A. F. Jaeger, and Lukas Chrostowski, "Multi-period Bragg gratings in silicon waveguides," *IEEE Photonics Conference (IPC)*, pp. WD2.5, 09/2013.

16. Wei Shi, **Han Yun**, Charlie Lin, Xu Wang, Yun Wang, Jonas Flueckiger, Nicolas A. F. Jaeger, and Lukas Chrostowski, "Silicon CWDM Demultiplexers Using Contra-Directional Couplers," in CLEO: 2013, OSA Technical Digest (online) (Optical Society of America, 2013), paper CTu3F.5.

17. Xu Wang, **Han Yun**, and Lukas Chrostowski, "Integrated Bragg Gratings in Spiral Waveguides," in CLEO: 2013, OSA Technical Digest (online) (Optical Society of America, 2013), paper CTh4F.8.

18. Wei Shi, Ting Kai Chang, **Han Yun**, Wen Zhang, Yun Wang, Charlie Lin, Nicolas A. F. Jaeger, Lukas Chrostowski, "Differential measurement of transmission losses of integrated optical components using waveguide ring resonators," Proc. SPIE 8412, Photonics North 2012, 84120R (24 October 2012).

19. Wei Shi, Xu Wang, Charlie Lin, **Han Yun**, Yang Liu, Tom Baehr-Jones, Michael Hochberg, Nicolas A. F. Jaeger, and Lukas Chrostowski, “Electrically tunable resonant filters in phase-shifted contra-directional couplers,” The 9th International Conference on Group IV Photonics (GFP), San Diego, CA, 2012, pp. 78-80.

20. Wei Shi, Xu Wang, Wen Zhang, **Han Yun**, Nicolas A. F. Jaeger, and Lukas Chrostowski, “Integrated Microring Add-Drop Filters with Contradirectional Couplers,” in Conference on Lasers and Electro-Optics 2012, OSA Technical Digest (online) (Optical Society of America, 2012), paper JW4A.91.

21. Wei Shi, Xu Wang, **Han Yun**, Wen Zhang, Lukas Chrostowski, and Nicolas A. F. Jaeger, “Add-drop filters in silicon grating-assisted asymmetrie couplers,” OFC/NFOEC, Los Angeles, CA, 2012, pp. 1-3.

22. Lukas Chrostowski, Samantha Grist, Jonas Flueckiger, Wei Shi, Xu Wang, Eric Ouellet, **Han Yun**, Mitch Webb, Ben Nie, Zhen Liang, Karen C. Cheung, Shon A. Schmidt, Daniel M. Ratner, Nicolas A. F. Jaeger, “Silicon photonic resonator sensors and devices,” Proc. SPIE 8236, Laser Resonators, Microresonators, and Beam Control XIV, 823620 (6 February 2012);

23. Xu Wang, Wei Shi, Samantha Grist, **Han Yun**, Nicolas A. F. Jaeger, and Lukas Chrostowski, “Narrow-band transmission filter using phase-shifted Bragg gratings in SOI waveguide,” IEEE Photonic Society 24th Annual Meeting, Arlington, VA, 2011, pp. 869-870.